

國立臺灣大學工學院機械工程學研究所

博士論文

Department of Mechanical Engineering


College of Engineering

National Taiwan University

Ph.D. Dissertation

水溶液環境原子力顯微鏡系統之設計與開發

Design and Development of Atomic Force Microscope Systems  
for Liquid Environment



廖先順

Hsien-Shun Liao

指導教授：黃光裕 博士

Advisor: Kuang-Yuh Huang, Dr.-Ing.

中華民國 102 年 1 月

January, 2013

## 誌謝

在博士班的這段時間中，除了感謝黃光裕老師在論文上的指導外，也給學生參與執行研究計劃的機會，拓展了學生的視野與經驗。感謝中研院物理所的張嘉升、黃英碩老師，除了老師們的真知灼見給予學生許多的啟發與學習，更營造了一個可讓學生們成長發揮的研究環境。

紹剛、志文、恩德、彥甫、仰山、博景學長，謝謝學長們無私的指導與照顧，給我上課所學不到的寶貴的經驗。原力精密儀器的合作團隊，貴銘、嘉宜、志憲、敬凱、彥名、建男、育琛、翰弘..，與各位一同開發儀器的時光既充實又有趣。中研院的同事們：韋僑、韋誠、伯彥、子銘、書正、士嶽、君岳、立維、偉文、信宏、仕修、秉翔、鑑元、旭佑、曉琪、欣純、奕賢、雅綾、淵智、延松、莉穎、少傑、崇開、賢真、維哲..，很榮幸能有機會與你們共事、讓我獲益良多。產學團隊與台大的同學們：偉珉、敬修、彥宏、仁峰、宣富、天仁、奕伸、彥名、秉彤、揚文、Chris、Jens、銘廷、仲翔、明山..，小至尋找六角板手，大至論文檔案救援都受你們照顧了。謝謝物理所精工室團隊總是幫助我們製作品質優良的工件。要感謝的人太多無法盡列，願相關的研究者也能從此論文中得到一點助益。

感謝我所信的神，讓我在研究過程中學習謙卑，重新認識自己的所是、所知、所能之渺小與有限，願榮耀歸與我神。

*When I applied my mind to know wisdom and to observe man's labor on earth – his eyes not seeing sleep day or night – then I saw all that God has done. No one can comprehend what goes on under the sun. Despite all his efforts to search it out, man cannot discover its meaning. Even if a wise man claims he knows, he cannot really comprehend it.*

*ECCLESIASTES 8:16~17*

## 摘要

在水溶液環境中之操作能力為原子力顯微鏡的重要優勢之一，此優點使原子力顯微鏡廣泛地被應用於生化研究的領域。然而，水溶液介質會嚴重影響微懸臂探針之動態特性，進而增加取得高解析與穩定影像的困難度。

在此篇論文中，分別探討微懸臂探針之幾何造型、激振機構、以及像散式偵測方法以改善在水溶液中之性能。考慮微懸臂尺寸，等比例減小微懸臂長度與厚度可提高 Q 值與共振頻率。此外，相較於微懸臂第一共振模態，高階共振模態可提供較高之質量靈敏度。在激振機構方面，開發之微懸臂夾持針座可有效減低水中之雜峰，並能提供彎曲式以及扭曲式兩種不同激振模式。藉由光路的修改，像散式偵測系統之靈敏度可被最佳化，並提高光學掃描模式對生物細胞成像之解析度。

最後，應用以上經驗開發一像散式偵測之水溶液原子力顯微鏡系統，水中雜峰可低於真實微懸臂共振峰值之 26.0%。此外，藉由達到對石墨單原子層台階以及 DNA 樣品於水溶液中成像，驗證系統解析度以及量測軟性生物樣品之能力。

關鍵字：原子力顯微鏡、水溶液環境、像散效應

# Abstract

The ability to operate in liquid environment is a remarkable advantage of the atomic force microscope (AFM). This advantage enables the AFM to be applied to the bio-chemical field widely. However, the dynamic properties of the cantilever tip are influenced significantly in liquid, and cause the difficulty in getting high resolution and stable images.

In this dissertation, the cantilever geometry, the excitation mechanism, and the astigmatic detection method are studied for improving the AFM's performance in liquid. Considering the cantilever dimensions, the resonant frequency and the Q-factor can be raised through decreasing cantilever thickness and length proportionally. Besides, the high-order resonances can provide higher mass sensitivity than the fundamental one. In the excitation mechanism, a clamp-modification holder is developed for reducing spurious peaks and enhancing the real resonant peak, and provides a more apparent flexural or torsional excitation. Moreover, the sensitivity of the astigmatic detection system is optimized, and the resolution of the optical scanning method is also improved for imaging the bio-sample.

Accumulating the experience above, a liquid-AFM system is developed based on the astigmatic detection method. The spurious peaks are suppressed down to 26.0 % of the resonant peaks in the liquid environment. Furthermore, it is verified that the liquid-AFM can realize high-resolution scanning images of the sub-nano scale graphite layer and the soft DNA sample in water.

Keywords: AFM, Liquid environment, Astigmatism



# Table of Contents

誌謝 .....	i
摘要 .....	ii
Abstract.....	iii
Table of Contents.....	iv
List of Figures.....	vii
List of Tables .....	xi
<b>Chapter 1 Introduction.....</b>	<b>1</b>
1.1 Motivation .....	1
1.2 Literature Survey.....	2
1.2.1 History of AFM.....	2
1.2.2 Operation modes of AFM.....	6
1.2.3 Phenomenons in liquid .....	10
1.3 Contribution.....	13
1.4 Thesis Organization .....	14
<b>Chapter 2 Preliminary .....</b>	<b>15</b>
2.1 AFM System Structure .....	15
2.2 Force Sensing System.....	16
2.2.1 Cantilever force sensor .....	16
2.2.2 Excitation source .....	19
2.2.3 Cantilever detection system.....	23
2.3 Actuator System .....	25
2.3.1 Scanner .....	25

2.3.2 Z-axis approaching system .....	30
2.4 Control System .....	31
2.4.1 Lock-in amplifier .....	31
2.4.2 Z-axis feedback control .....	32
2.4.3 XY-axes scanning control .....	34
<b>Chapter 3 Cantilever Force Sensor .....</b>	<b>35</b>
3.1 Cantilever Dimensional Effect .....	35
3.1.1 Theoretical calculation .....	35
3.1.2 Experimental Results .....	41
3.2 High Order Resonances .....	48
3.2.1 Mass sensitivity in air .....	49
3.2.2 Mass sensitivity in water .....	56
3.3 Conclusion .....	60
<b>Chapter 4 Excitation Source and Transmission .....</b>	<b>62</b>
4.1 Cantilever Holder Design .....	62
4.1.1 Modified commercial holder .....	62
4.1.2 Material modification .....	68
4.1.3 Preload adjustment .....	75
4.1.4 Chip-clamped modification .....	79
4.2 Conclusion .....	83
<b>Chapter 5 Cantilever Detection System .....</b>	<b>84</b>
5.1 Astigmatic Detection Method .....	84
5.2 Detective Sensitivity in Water .....	86
5.3 Optical Scanning Images in Water .....	93
5.4 Spring Constant Calibration .....	95

5.4.1 Thermal fluctuation method.....	96
5.4.2 ADS setup for spring constant calibration.....	97
5.4.3 Calibration on AFM and ADS.....	98
5.5 Conclusion.....	103
<b>Chapter 6 Liquid Environment AFM.....</b>	<b>105</b>
6.1 System Configuration.....	105
6.1.1 Equipment construction.....	107
6.1.2 Electronic control system.....	109
6.2 Experimental Verification.....	117
6.2.1 Scanning in air.....	117
6.2.2 Scanning in liquid.....	124
6.3 Conclusion.....	129
<b>Chapter 7 Summary.....</b>	<b>130</b>
References.....	132
Appendix.....	140
Publication List.....	146

## List of Figures

Fig. 1.1	Scheme of STM .....	3
Fig. 1.2	First AFM setup .....	4
Fig. 1.3	Biological images of (a) double-stranded DNA (BlueScript II), (b) human blood protein fibrinogen (image size is 450 nm × 450 nm), (c) white blood cell (image size is 9.1 μm × 9.1 μm) .....	5
Fig. 1.4	Force-displacement curve of contact mode .....	7
Fig. 1.5	Force-displacement curves of tapping mode .....	9
Fig. 1.6	Cantilever resonant modes.....	10
Fig. 1.7	Spectra of different length cantilevers.....	12
Fig. 1.8	Two different transmissive ways .....	13
Fig. 2.1	Force sensing system, actuator system, and control system.....	16
Fig. 2.2	SEM images of commercial cantilevers (MikroMasch).....	17
Fig. 2.3	Double tips artifact .....	18
Fig. 2.4	Scheme of piezoelectric actuator excitation .....	19
Fig. 2.5	Scheme of magnetic excitation method.....	20
Fig. 2.6	Scheme of Lorentz force excitation method.....	20
Fig. 2.7	Scheme of photothermal excitation method .....	21
Fig. 2.8	Cantilever holder design of Asakawa and Fukuma .....	22
Fig. 2.9	Excitation spectrum comparison between two materials .....	23
Fig. 2.10	Cantilever detection methods .....	24
Fig. 2.11	Piezoelectric scanner .....	26
Fig. 2.12	Piezoelectric hysteresis with different input amplitudes .....	27

Fig. 2.13	AFM images of calibration grating with 3 $\mu\text{m}$ pitch .....	28
Fig. 2.14	Open-loop scanner calibration .....	29
Fig. 2.15	Closed-loop scanner control .....	30
Fig. 2.16	Digital lock-in amplifier diagram .....	32
Fig. 2.17	Z-axis feedback control diagram .....	33
Fig. 2.18	XY-axes scanning control .....	34
Fig. 3.1	Cantilever properties versus cantilever dimensions .....	40
Fig. 3.2	Cantilever properties with $L/h = 100$ and $b = 5 \mu\text{m}$ .....	41
Fig. 3.3	Cantilever No.02 with different widths .....	42
Fig. 3.4	Cantilever properties versus cantilever width in water .....	44
Fig. 3.5	Cantilever No.02 with different lengths .....	45
Fig. 3.6	Dynamic properties versus cantilever length in water .....	45
Fig. 3.7	Modified cantilever with different hole layouts .....	47
Fig. 3.8	Resonant frequency versus number of holes .....	48
Fig. 3.9	Cantilever dimensions .....	50
Fig. 3.10	Resonant frequency shift $\Delta f$ versus mass variation $\Delta m$ .....	52
Fig. 3.11	Configuration of experimental setup .....	53
Fig. 3.12	Modified cantilevers with mass variations .....	54
Fig. 3.13	Thermal fluctuation spectrums .....	55
Fig. 3.14	Thermal fluctuation spectra of $n$ th flexural deflection with and without mass-tuning (a) in air and (b) in water .....	58
Fig. 3.15	Experimental and simulated mass sensitivity of five flexura modes in water .....	59
Fig. 3.16	Thermal fluctuation spectra of torsional deflection signal with and without mass-tuning (a) in air and (b) in water .....	60

Fig. 4.1	Commercial TR-mode holder .....	63
Fig. 4.2	Spectrums of cantilever PPP-NCHAuD .....	65
Fig. 4.3	Spectrums of cantilever CSC38B .....	67
Fig. 4.4	PEEK-based holder.....	69
Fig. 4.5	Spectrums of cantilever PPP-NCHAuD .....	70
Fig. 4.6	Spectrums of cantilever CSC38B .....	71
Fig. 4.7	Steel-based holder.....	72
Fig. 4.8	Spectrums of cantilever PPP-NCHAuD .....	73
Fig. 4.9	Spectrums of cantilever CSC38B .....	74
Fig. 4.10	Adjustable preload holder.....	75
Fig. 4.11	Spectrums of cantilever PPP-NCHAuD with different preload .....	77
Fig. 4.12	Spectrums of cantilever CSC38B with different preload .....	78
Fig. 4.13	Clamp-modification holder.....	80
Fig. 4.14	Spectrums of cantilever PPP-NCHAuD.....	81
Fig. 4.15	Spectrums of cantilever CSC38B .....	83
Fig. 5.1	(a) Configuration of ADS and (b) focus error signal $U_{FES}$ versus cantilever displacement .....	85
Fig. 5.2	Astigmatic pickup head .....	86
Fig. 5.3	Optical paths of (a) DVD optical disc, and (b) water environment.....	88
Fig. 5.4	ADS sensitivity measurement setup .....	89
Fig. 5.5	$U_{FES}$ versus displacement curves (S-curves) .....	91
Fig. 5.6	Sensitivity $S_{ADS}$ versus water thickness $h_{water}$ .....	92
Fig. 5.7	$U_{FES}$ versus displacement curves (S-curves) .....	93
Fig. 5.8	Optical scanning images of MCF-7 breast cancer cell .....	95
Fig. 5.9	(a) Configuration and (b) construction of calibration setup .....	98

Fig. 5.10	SEM images of cantilevers .....	99
Fig. 5.11	Experimental results on AFM.....	100
Fig. 5.12	Experimental results on ADS .....	102
Fig. 6.1	Configuration of liquid-AFM .....	107
Fig. 6.2	Equipment construction.....	108
Fig. 6.3	Cantilever holder .....	109
Fig. 6.4	Programmable embedded controller.....	110
Fig. 6.5	Processing strategies of lock-in amplifier .....	111
Fig. 6.6	Configuration of lock-in amplifier .....	112
Fig. 6.7	Z-axis feedback control configuration.....	113
Fig. 6.8	Scanning control flowchart.....	114
Fig. 6.9	Scheme of coordinate rotational of scan range.....	115
Fig. 6.10	XY-axes scanning control process.....	116
Fig. 6.11	Tip-sample approaching process .....	117
Fig. 6.12	Flexural bode plot of cantilever PPP-NCHAuD in air .....	118
Fig. 6.13	Scanning results on test grating TGQ1 in air.....	120
Fig. 6.14	Scanning results on test grating 607-AFM in air.....	122
Fig. 6.15	Scanning results on graphite (HOPG) in air.....	124
Fig. 6.16	Flexural spectrums of cantilever PPP-NCHAuD in air and water .....	125
Fig. 6.17	Scanning results on graphite (HOPG) in water .....	127
Fig. 6.18	Scanning results of DNA on mica in liquid.....	128

## List of Tables

Table 3.1	Numerical values of parameters .....	39
Table 3.2	Experimental results of various widths .....	43
Table 3.3	Influence of cantilever length on dynamic properties. ....	46
Table 3.4	Influence of number of holes on dynamic properties .....	47
Table 3.5	Dimensions of REM-cantilevers .....	50
Table 3.6	Dynamic properties and mass sensitivity of modified cantilevers in air ....	55
Table 3.7	Simulated dynamic properties and mass sensitivity .....	57
Table 3.8	Influence of resonant mode on dynamic properties and mass sensitivity ....	58
Table 5.1	Specification of TopRay pickup head .....	86
Table 5.2	Sensitivity $S_{ADS}$ of objective lenses under different water thicknesses.....	92
Table 5.3	Experimental results on AFM and ADS .....	102



# Chapter 1

## Introduction

### 1.1 Motivation

The atomic force microscope (AFM) is a powerful tool in various nanotechnology fields for different operative environments. Particularly, the scanning ability in liquid is valued for bio-chemical applications. Liquid environmental measurement approaches the physiological conditions of many biomolecules, and the AFM is able to observe an individual molecule by its high spatial resolution. Besides, the AFM enables unique measurements of mechanical properties. These advantages induce more and more investigations relied on the AFM. However, getting high resolution and stable images is still a challenge due to some factors in liquid. Therefore, the main object of this dissertation is to improve the AFM's performance in the liquid environment.

In the AFM system, a tiny cantilever tip is used for scanning on the measured sample. For reducing damages to the tip and sample, the tapping mode AFM becomes a general method, which vibrates the cantilever at its resonant frequency. However, when the cantilever tip is immersed in liquid, the dynamic properties of the cantilever tip are influenced significantly. Usually, the quality factor (Q-factor) is below 10 in water, and the resonant frequency also decreases due to the increased damping effect of liquid. Besides, the external excitation for oscillating the cantilever can be easily propagated through liquid and then causes complex acoustic interferences. Furthermore, the cantilever deflection is usually detected by a laser beam deflection system, and the varied refractive index could change the laser focus on the cantilever. These factors not only affect the force sensitivity of the cantilever tip, but also cause an error on the

quantitative measurement.

According to these limitations, we approach to these solutions in three different ways: cantilever geometry, cantilever holder, and cantilever detection. The affection of the cantilever geometric dimensions in liquid is studied. Different cantilever holders are designed for reducing complex acoustic interferences. The advantages and disadvantages of the optical beam deflection and astigmatic detection methods are compared. These issues are considered for the AFM design and development.

## **1.2 Literature Survey**

### **1.2.1 History of AFM**

Scanning probe microscopy (SPM) includes many different technologies, and measures various physical properties for different purposes. In 1981, Binnig and Rohrer invented the first technology of SPM: the scanning tunneling microscope (STM) [1]. This invention opened a door of atomic-scale measurement and manipulation [2,3], and was rewarded the Nobel Prize in 1986. As its name, the STM detects the tunneling current between a sharp tip and the measured sample. The tunneling current occurs when the tip is close to the sample enough. Therefore, the tunneling current is used as a reference signal, which is kept constant by adjusting the tip-sample distance. Through a precise piezoelectric XYZ-scanner, the tip can scan and trace the sample surface as shown in Figure. 1.1. The tip trajectory is recorded during scanning, and the 3D surface topography is depicted.

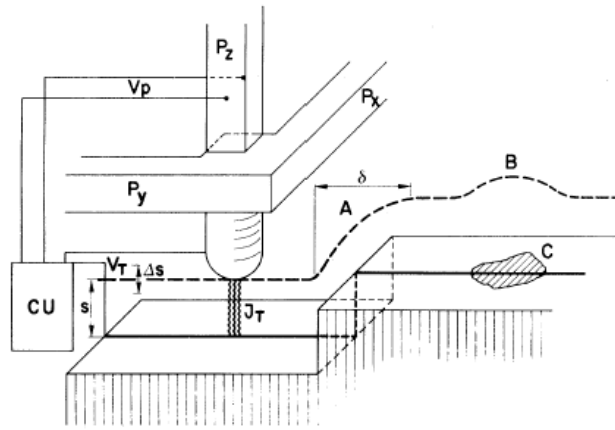


Figure. 1.1 Scheme of STM [1]

Based on the STM technology, Binnig *et al.* invented the AFM in 1986 [4]. Unlike the STM, the reference signal of the tunneling current is replaced by the interactive force between the tip and the sample. The first AFM setup is shown in Figure 1.2. A diamond tip is attached on a tiny cantilever. The interactive force applied on the tip deforms the cantilever, and the flexural deflection of the cantilever is detected by a STM tip on the other side. In this method, the sample is not limited to conductive materials anymore. This breakthrough extends the applicative range widely, and many related technologies based on the AFM are developed for measuring various physical properties. For instance, the friction force microscope (FFM) is achieved by measuring the torsional deflection of the cantilever [5]. Utilizing a magnetized tip, the surface magnetic field can be measured by the magnetic force microscope (MFM) [6]. Through applying a bias between a conductive tip and the sample, the AFM transforms into the electrostatic force microscope (EFM) [7, 8]. Moreover, there are still many other technologies like the scanning near-field optical microscope (SNOM) [9], the scanning thermal microscope (SThM) [10], etc.

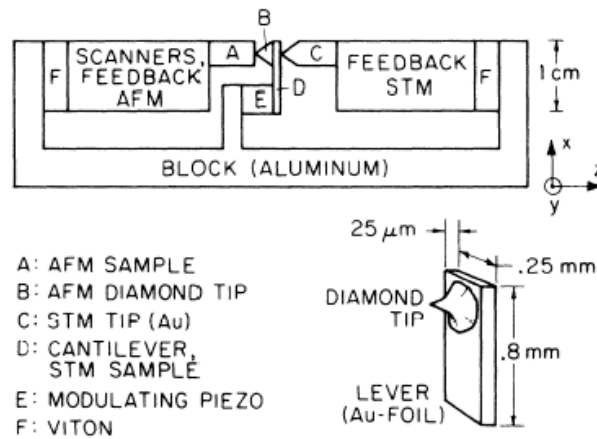


Figure 1.2 First AFM setup [4]

Furthermore, the AFM is adaptive to various environments that include air, vacuum, and liquid. Because most biomolecules live in liquid environment, the potential ability of the measurement in liquid is particularly valuable for biological applications. Deoxyribonucleic acid (DNA) is one of important targets, because it contains the genetic code of living organisms. Through the AFM, reproducible imaging of DNA in liquid was achieved [11]. Besides, the mechanical properties of a single DNA can also be measured by the AFM [12, 13]. In these kinds of experiments, one end of the DNA molecule is fixed on the substrate, and the other end is attached to the cantilever tip. When the cantilever tip is pulled away from the substrate, the stretched force on the DNA can be determined by the cantilever flexural deflection. For another significant instance, protein is an essential part in organisms and performs many fundamental biological processes. Through the AFM, Drake *et al.* showed the clotting of the human blood protein fibrinogen in real time [14]. Membrane protein performs processes such as energy conversion, signal transmission, and molecular transport [15], and the AFM is able to observe the response of an individual protein to external stimulation such as voltage and pH [16]. For understanding the molecular processes on the cell surface, the

AFM also has potential for imaging and manipulating living cells [17, 18]. Several biological images from previous literatures are shown in Figure 1.3 for demonstration. The AFM cantilever tip is not only a sensitive force sensor for imaging, it can also be utilized for manipulating and pressing molecules. Stark *et al.* demonstrated that human metaphase chromosomes were successful dissected by the AFM [19]. Similarly, subunits from a multi-protein can also be damaged for analysing the underlying structures [20]. These results show that controlling a single biomolecule is possible through the AFM.

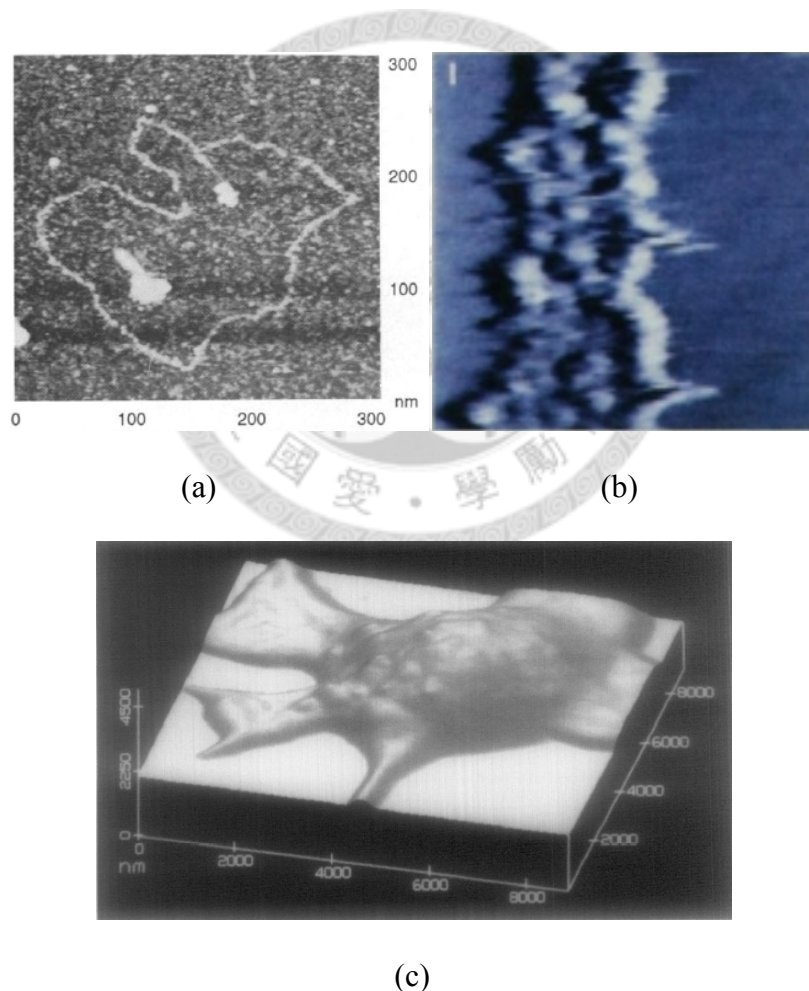


Figure 1.3 Biological images of (a) double-stranded DNA (BlueScript II) [11], (b) human blood protein fibrinogen (image size is 450 nm  $\times$  450 nm) [14], (c) white blood cell (image size is 9.1  $\mu$ m  $\times$  9.1  $\mu$ m) [17]

## 1.2.2 Operation modes of AFM

There are various operation modes on the AFM with different features. The contact mode (static mode) is the first operation mode of the AFM. For explaining, the force-displacement curve (force curve) is illustrated in Figure 1.4. The y-axis represents the flexural deflection of the cantilever, and the x-axis is the z displacement of the piezoelectric scanner. At the initial position (index 1), the tip is far from the sample, and there is no force acting on the cantilever. Next, the sample is brought close to the tip continuously. Until the tip is very close to the sample (index 2), the capillary force caused by the thin water layer on the sample and the Van der Waals force attract the cantilever to the sample. Following the closer distance, the tip will contact with the sample, then the repulsive force between atoms will bend the cantilever upward linearly (index 3). The contact mode AFM is operated in this repulsive region. When the cantilever removes from the sample, the capillary force still grabs the tip until the cantilever spring force exceeds the attractive force. This curve presents the relation between the cantilever flexural deflection and the scanner displacement. Therefore, the curve is called the force-displacement curve or the force curve. For capturing the topography of the sample, the tip will scan the sample surface along the X-Y axes by the piezoelectric scanner, and a feedback controller is used to keep the cantilever deflection constant by adjusting the Z axis of the scanner. Therefore, the tip-sample interactive force is maintained constant during scanning. The recorded 3-D displacement of the scanner represents the acquisitive topography that will be showed on the computer. In the contact mode, the cantilever tip is always kept contact with the sample. Some techniques must be operated in the contact mode like the FFM and the conductive AFM (CAFM). However, the contact mode induces larger lateral force, and could damage soft samples easily.

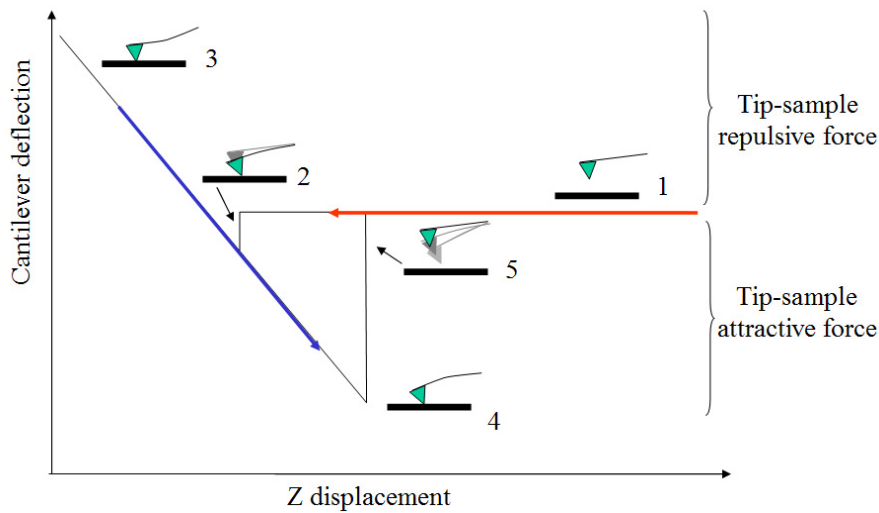


Figure 1.4 Force-displacement curve of contact mode

The tapping mode (intermittent contact mode) is the most common mode in the AFM today. This mode improves the resolution and reduces damage to soft samples [21, 22]. In the tapping mode, the cantilever tip is oscillated around its resonant frequency, and lightly taps on the sample surface. Since the tip is no longer continuously in contact with the sample, the lateral friction between the tip and the sample is reduced significantly. Similar to the contact mode, the force-displacement curve illustrates the operating region of the reference signal. An experimental force-displacement curve on a hard substrate is shown in Figure 1.5 [23]. Figure 1.5(a) shows the relation between the cantilever oscillation amplitude and the z-axis scanner displacement. The amplitude doesn't change when the cantilever tip is still far from the sample. A small amplitude reduction occurs when the tip falls in the attractive region intermittently, and the repulsive force keeps reducing the amplitude to zero with the tip-sample distance decreasing. Substituting the cantilever deflection signal, the amplitude signal is chosen as the reference signal for z-axis feedback control. Therefore, the tapping mode is also specified as the amplitude modulation AFM (AM-AFM). In the tapping mode, the

phase signal represents the phase shift between the excitation signal and the cantilever oscillation. The phase signal is very sensitive to the material properties, and provides an intense contrast between different materials [24]. The phase signal also varies with the z-axis displacement as shown in Figure. 1.5(b). Through the amplitude and phase signals, the total energy transmission on the cantilever can be calculated, and the tip-sample energy dissipation is evaluated as shown in Figure. 1.5(c). Similarly, the phase modulation AFM (PM-AFM) utilizes the phase signal as the feedback reference signal [25]. The PM-AFM is claimed to be more suitable for high speed imaging, because its time response is not influenced by the Q-factor of the cantilever. Except the AM-AFM and the PM-AFM, the mode used the frequency shift of the cantilever resonant frequency is so called the frequency modulation AFM (FM-AFM) [26]. Besides the high resolution imaging ability [27], the measurement of dissipative energy is also proposed by the FM-AFM [28]. However, the FM-AFM also requires a stable cantilever deflection signal, and could be disrupted by occasional disturbance such as the tip crash, adhesion and environmental thermal variation. In contrast with the contact mode, these modes with the oscillation are classified into the dynamic mode.



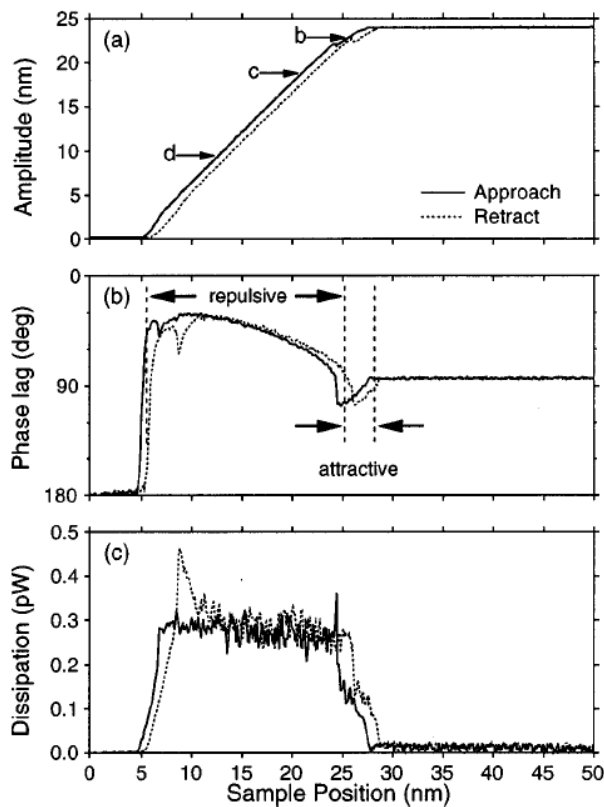


Figure 1.5 Force-displacement curves of tapping mode [23]

The dynamic mode mentioned above is associated with the electric signal modulation. From the point of mechanics, the cantilever tip has infinite different resonant modes itself. Figure 1.6 shows several modes of a rectangular cantilever tip. Most often, the fundamental flexural mode is used for the dynamic mode. Some higher order resonant modes of the cantilever can also get stable images, and their phase images have high contrast on different materials [29]. Another associated method detects the higher harmonics of the fundamental resonance [30, 31]. In this method, the force-displacement curve is constructed from higher harmonic signals, and the material mechanical properties can be evaluated by theoretic equations. In the torsion mode AFM (TR-AFM), the cantilever executes a small torsion resonant oscillation on its long axis as shown in Figure 1.6(d). The TR-AFM can measure the in-plane sample properties

such as friction and elasticity [32], and the AM and FM techniques can also adapt to the TR-AFM [33]. Comparing with the fundamental flexural mode, the Q-factor of the torsion mode is higher, and the long-range normal force has less influence on the frequency shift [34].

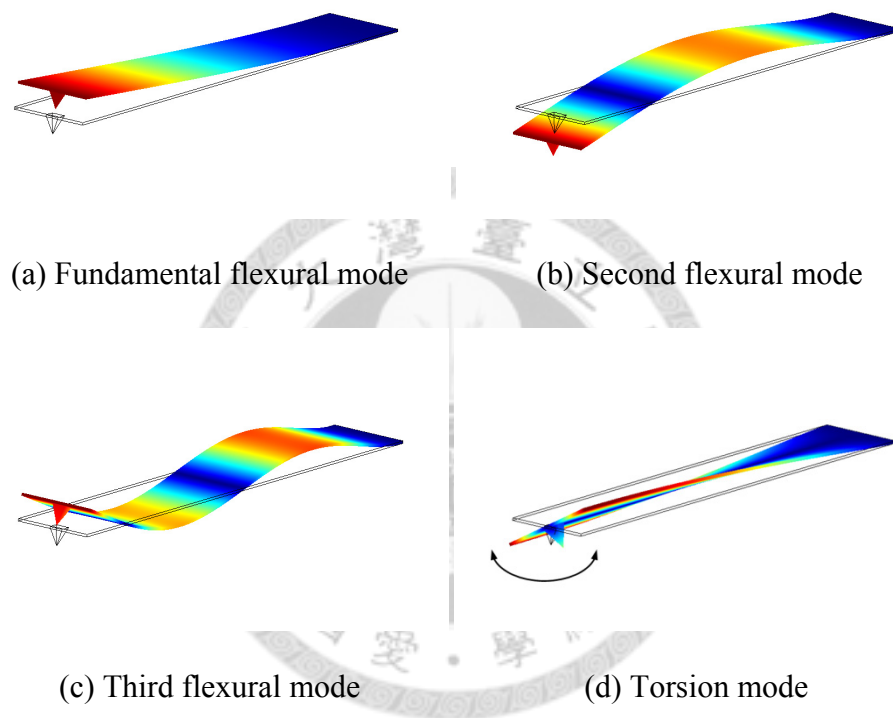


Figure 1.6 Cantilever resonant modes

### 1.2.3 Phenomenons in liquid

Although the dynamic mode has many advantages for soft bio-samples. Some problems occur in liquid environment. The liquid viscosity significantly dampens the dynamic properties such as the resonant frequency and the Q-factor. In the AM-AFM, the minimum time required for measuring the cantilever amplitude is inverse proportioned to the resonant frequency. Therefore, the reduction of the resonant

frequency decreases the response bandwidth of the cantilever. Besides, the Q-factor is usually below 10 in water, and lowers the force sensitivity. Furthermore, the excitation spectrum is usually no longer pure as in air. Schäffer *et al.* showed the experimental results as Figure 1.7 [35]. Figure 1.7(a), (b), and (c) represent the spectra of three cantilevers with different lengths of 203  $\mu\text{m}$ , 130  $\mu\text{m}$ , and 78  $\mu\text{m}$ , respectively. The lowest line in each figure represents the spectrum caused by the thermal fluctuation, and other spectra are excited by the piezoelectric actuator with different modules. Comparing with the results of the external excitation, the resonant peak in the thermal fluctuation spectrum is pure and blunt. The resonant frequency from the thermal fluctuation spectrum changes with the cantilever length. This phenomenon corresponds with the theoretical tendency. On the other hand, the resonant peaks are similar on the same module, but independent of the cantilever length. Therefore, these complex peaks are not the original resonant peak of the cantilever. There spurious peaks could be caused by the fluid driving, and well known as “forest of peaks”.

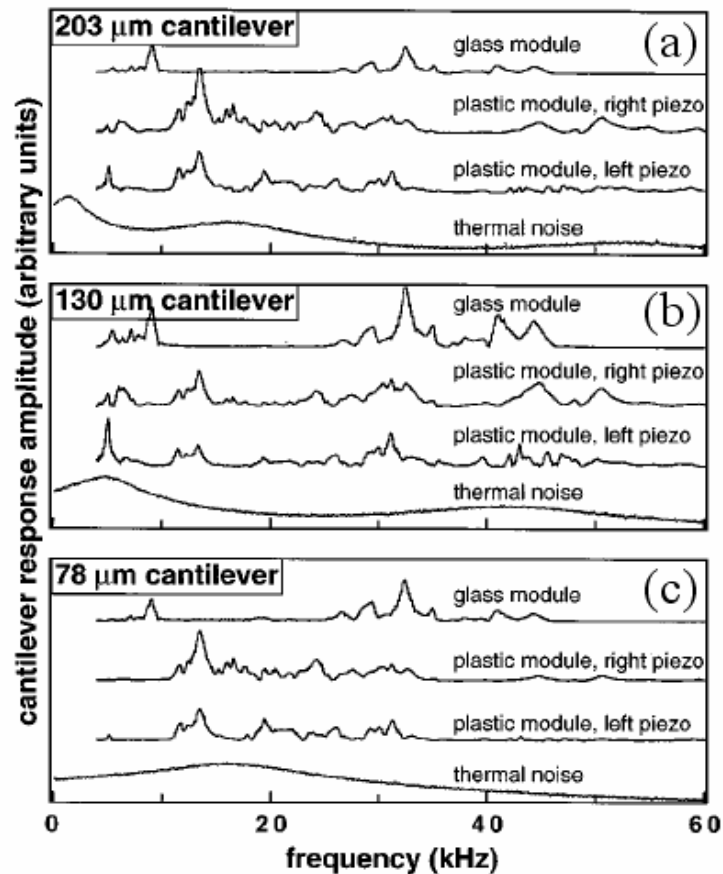


Figure 1.7 Spectra of different length cantilevers [35]

This phenomenon is common on commercial AFMs, and causes not only a difficulty in determining the operating frequency, but also an error on the quantitative force and dissipation measurements. Kiracofe and Raman measured the cantilever and vibrated base motion carefully by a scanning laser Doppler vibrometer [36]. The energy transmission from the piezoelectric actuator is interpreted in Figure. 1.8. The cantilever is excited by the mechanical motion of the cantilever base and acoustic fluid waves through fluid. Because the base motion can't be measured directly by the optical beam deflection method in the typical AFM, the quantitative energy calculation is difficult to obtain in liquid.

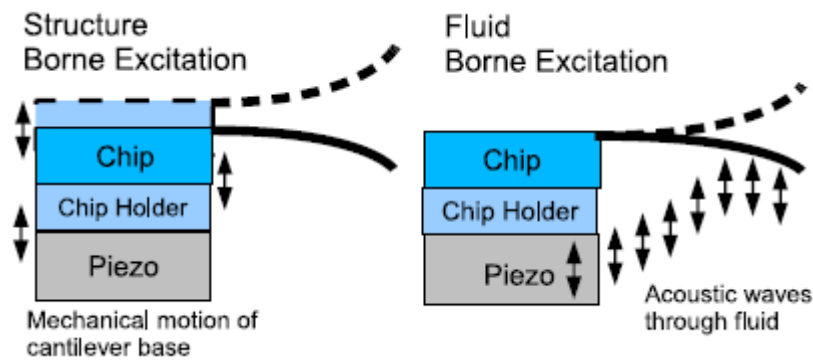


Figure 1.8 Two different transmissive ways [36]

### 1.3 Contribution

This dissertation devotes to improve the disadvantageous tendencies in liquid. For increasing the resonant frequency and the Q-factor of the cantilever, the cantilever geometry is studied. The relation between rectangular cantilever dimensions and dynamic properties are presented and examined. Besides, the higher order resonant modes are proposed for improving the mass sensitivity, and this method can be utilized for biosensing applications.

To overcome the “forest of peaks”, a series of cantilever tip holders is designed and developed. The effects of the materials and preload are examined. Spurious peaks can be reduced, and the real resonant peaks can be enhanced on both flexural and torsional spectrums by the developed holder.

For detecting the cantilever deflection, an astigmatic detection method is adopted. Its sensitivity is optimized for liquid environment, and the optical scanning method is demonstrated for imaging the bio-sample in liquid. Comparing with the typical optical beam deflection method, the astigmatic detection method is more sensitive to the vertical displacement and less sensitive to the angular displacement of the cantilever. Therefore, an efficient method of cantilever spring constant calibration is realized, and

the tipless cantilever is also adapted.

Finally, an AFM system is developed for liquid environment with the astigmatic detection system (ADS). The single atomic layer of the graphite (HOPG) and DNA samples are imaged in liquid successfully.

## **1.4 Thesis Organization**

The dissertation consists of seven chapters. Chapter 2 introduces the basic structure and components of the AFM. In Chapter 3, the affection of the cantilever dimensions is discussed through theorems and experiments. Basing on the analysis, a mass sensing method by cantilever high order resonances in water is also demonstrated. In Chapter 4, different cantilever holder designs are developed. The points for reducing the complex acoustic interference are discussed according to the experimental results. The astigmatic detection method is studied in Chapter 5. The sensitivity of the astigmatic detection system is examined, and the optimum condition is proposed for operating in water. Besides, the spring constant calibration process is presented by the astigmatic detection system. Chapter 6 displays the configuration and experimental results of a homemade AFM for liquid environment. In the final chapter, a summary of this dissertation is made.

## Chapter 2

### Preliminary

In this chapter, the AFM system is divided into the force sensing system, the actuator system, and the control system. The functions in these three sub-systems are introduced respectively. Besides, some typical phenomena and limitations of the AFM components are also presented.

#### 2.1 AFM System Structure

The force sensing system, actuator system, and control system are three main components of an AFM. A system block diagram is shown in Figure 2.1. The force sensing system measures the interactive force between the cantilever tip and the sample. For the dynamic mode, an excitation source is essential to resonate the cantilever. When the cantilever deformation is small, the cantilever force sensor is equivalent to a linear spring. The cantilever deformation is detected by the cantilever detection system, and is usually transduced to the voltage signal for the controller. The actuator system is responsible to produce the precise relative displacement between the tip and the sample. The surface image is scanned through the XYZ scanner. Because the maximum displacement range of the scanner is usually at micrometer scale, the tip and the sample must be brought closely by another Z-axis approaching system. The control system receives the cantilever deformation signal from the force sensing system, and commands the actuator system for the scanning. For the dynamic mode, a lock-in amplifier or a phase lock loop (PLL) is required for driving the excitation source and getting the amplitude, phase, or frequency signals. In an AFM with an automatic

approaching function, the Z-axis approaching system is also controlled by the control system. The user interface, data processes are executed by the software in the computer.

Furthermore, some additional implements can also be combined in the AFM system. An optical microscope (OM) and a XY coarse stage are helpful to specify the scanning area on the sample, when the sample has some larger features. The combination of the Raman spectroscopy and the fluorescence imaging can also be realized on the OM-based AFM for molecular identification.

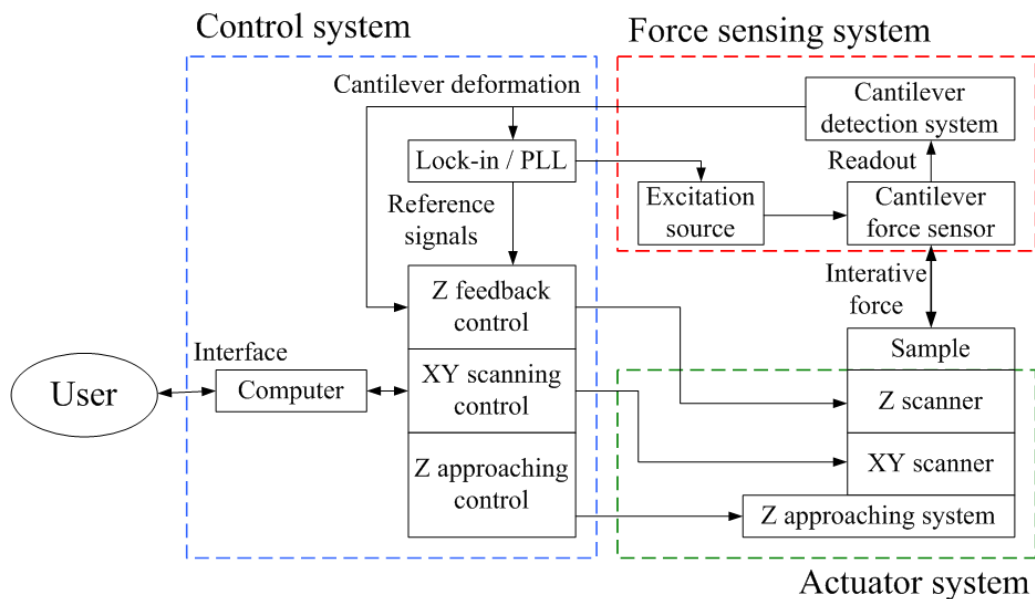


Figure 2.1 Force sensing system, actuator system, and control system

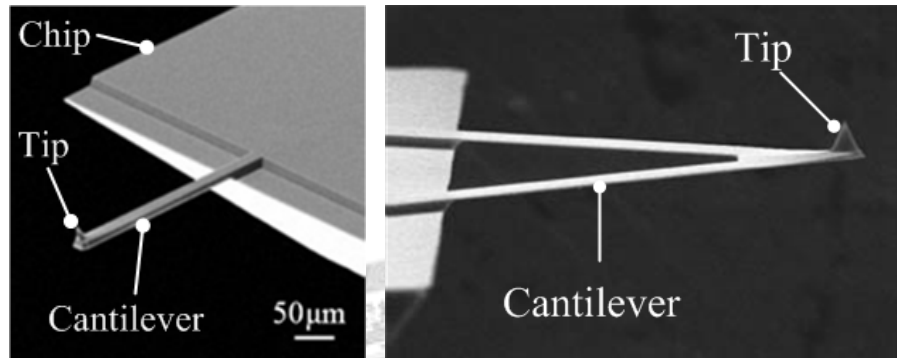
## 2.2 Force Sensing System

### 2.2.1 Cantilever force sensor

The force sensor is a critical element in the AFM, and includes the cantilever and the tip. Figures 2.2 show the scanning electron microscope (SEM) images of commercial cantilever tips. The cantilever is based on a chip for handling easily. A tiny tip sites on the front end of the cantilever and faces to the measured sample. The structure is made by the microelectromechanical systems (MEMS) process. The



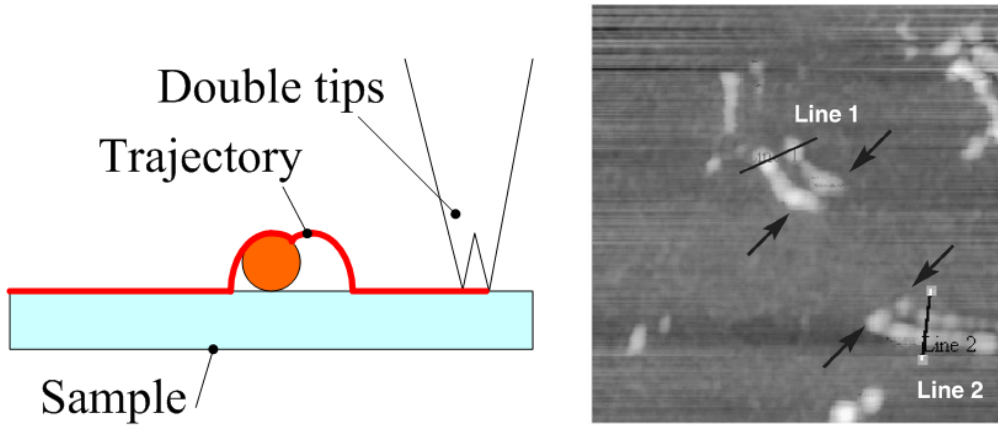
cantilever geometry is designed for different requirements. Figure 2.2(a) and Figure 2.2(b) present a rectangular cantilever and a triangular cantilever, respectively. The rectangular cantilever has uniform cross-section, and its spring constant and resonant frequency can be evaluated simply. The triangular cantilever is less sensitive to the lateral force and disturbance.



(a) Rectangular cantilever tip (b) Triangular cantilever tip

Figure 2.2 SEM images of commercial cantilevers (MikroMasch)

The sharpness of the tip influences the resolution in XY plane directly. Nowadays, the apex radius of the commercial tip is about several nanometers. However, large force between the tip and the sample could wear the tip. The tip could also be polluted due to adherent dust or biomolecules. For example, a typical artifact caused by the double tips is illustrated in Figure 2.3(a). Two tips contact with the sample alternately, and cause an error on the scanning trajectory. Figure 2.3(b) shows the pectin aggregates image captured by the double tips [37].



(a) Scheme of double tips trajectory (b) Pectin aggregates image of double tips [37]

Figure 2.3 Double tips artifact

The cantilever is another significant component, which affects the force sensitivity and the scanning speed directly. When the cantilever deformation is much smaller than its dimensions, the cantilever can be seen as a linear spring. On a homogeneous rectangular cantilever, the spring constant  $k$  and the fundamental resonant frequency  $f_r$  of the fundamental flexural mode can be approximated by following Equations (2.1) and (2.2) [38]:

$$k = \frac{Ebh^3}{4L^3}, \quad (2.1)$$

$$f_r = 0.162 \sqrt{\frac{E}{\rho_c}} \frac{h}{L^2}, \quad (2.2)$$

where  $E$  is the Young's modulus of cantilever,  $b$ ,  $h$ , and  $L$  are the width, thickness, and length of the cantilever, and  $\rho_c$  is the cantilever density.

For the contact mode, smaller spring constant  $k$  is preferred. Therefore, long and thin cantilevers are usually adapted. On the other hand, the dynamic mode often uses shorter and thicker cantilevers, which have higher resonant frequency  $f_r$ . The cantilever with high resonant frequency can reduce the response time, and improve the scanning

speed. However, the spring constant is also increased. This result causes larger interactive force between the tip and the sample. To overcome this conflict, the cantilever size trends to diminish in all dimensions, including the length, width, and thickness. Besides, the cantilever detection system also needs to be modified for the smaller cantilever.

### 2.2.2 Excitation source

In the dynamic mode, the cantilever has to be excited around its resonant frequency. The most common method utilizes a piezoelectric actuator to generate the oscillation energy as shown in Figure 2.4. The energy transfers to the cantilever through the mechanical parts on the cantilever holder. In liquid environment, “forest of peaks” phenomenon also appears generally. For avoiding this problem, different methods such as magnetic excitation and photothermal excitation are also developed.

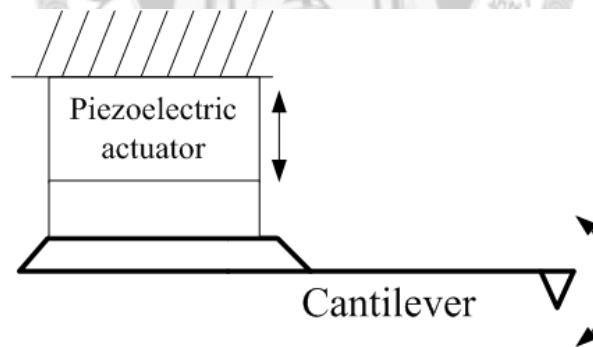


Figure 2.4 Scheme of piezoelectric actuator excitation

The magnetic excitation method applies an AC magnetic field on a magnetic cantilever as shown in Figure 2.5 [39, 40]. The magnetic excitation force applies on the cantilever directly, and a pure peak can be got in the tuning spectrum in liquid.

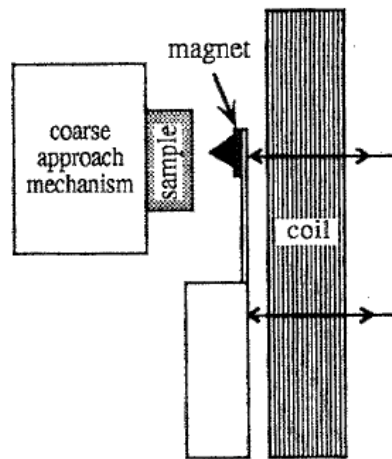


Figure 2.5 Scheme of magnetic excitation method [39]

The Lorentz force excitation method is illustrated in Figure 2.6 [41, 42]. Unlike the magnetic excitation method, the magnetic field is constant. The AC current passes through a triangular cantilever, and generates the vertical force on the cantilever. However, this method could also induce a coupling between the flexural mode and the torsion mode of the cantilever [43]. Besides, it could affect the imaging due to the immersed electrode in liquid buffer.

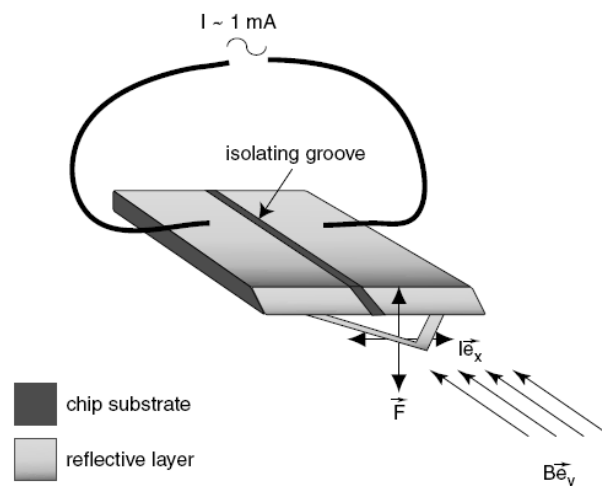


Figure 2.6 Scheme of Lorentz force excitation method [42]

Figure 2.7 displays a setup of the photothermal excitation method [44, 45]. Except the cantilever detection system, an additional laser is focused on the cantilever. The cantilever oscillation is induced by the heat expansion, and the oscillation frequency is controlled through the laser modulation.

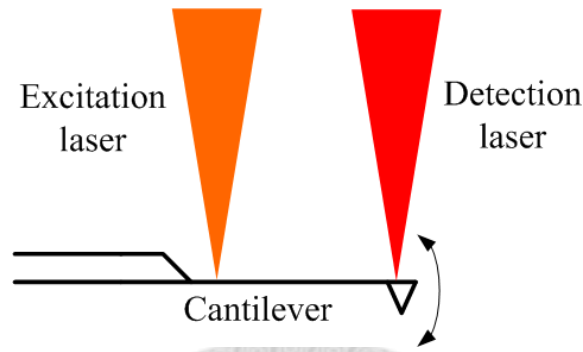


Figure 2.7 Scheme of photothermal excitation method

Summarizing these methods, applying excitation force on the cantilever directly is an effective way to eliminate the spurious peaks. However, additional equipment is required and complicates the system design. Furthermore, the magnetic and Lorentz force excitation methods limit the available cantilevers, and involve magnetic field and current into the measured environment. Therefore, some modifications based on piezoelectric excitation are also proposed on the other hand. Adams *et al.* studied the contact surface between the cantilever chip and the holder [46]. Typically in air, adjusting the cantilever position on the holder can eliminate the spurious peaks. Basing on this observation, the affection of dust or silicon shards on the cantilever is considered. Through modifying the chip surface by adding pattern, lowering the chip contact surface area decreased the occurrence of spurious peaks. This result can likely be attributed to a higher occurrence of particles trapped on larger contact area.

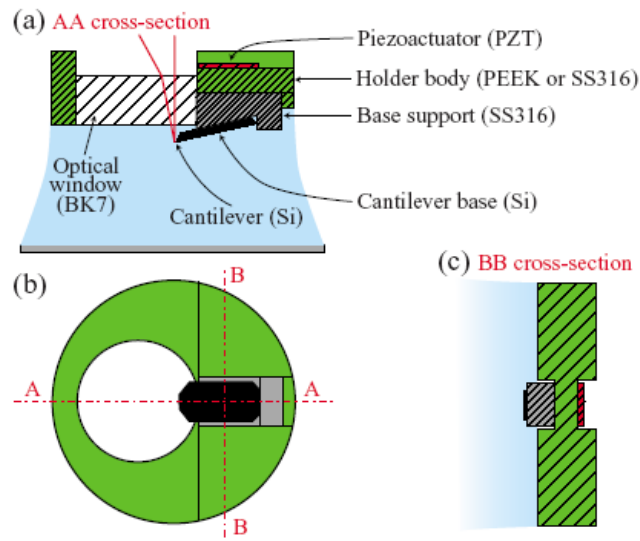
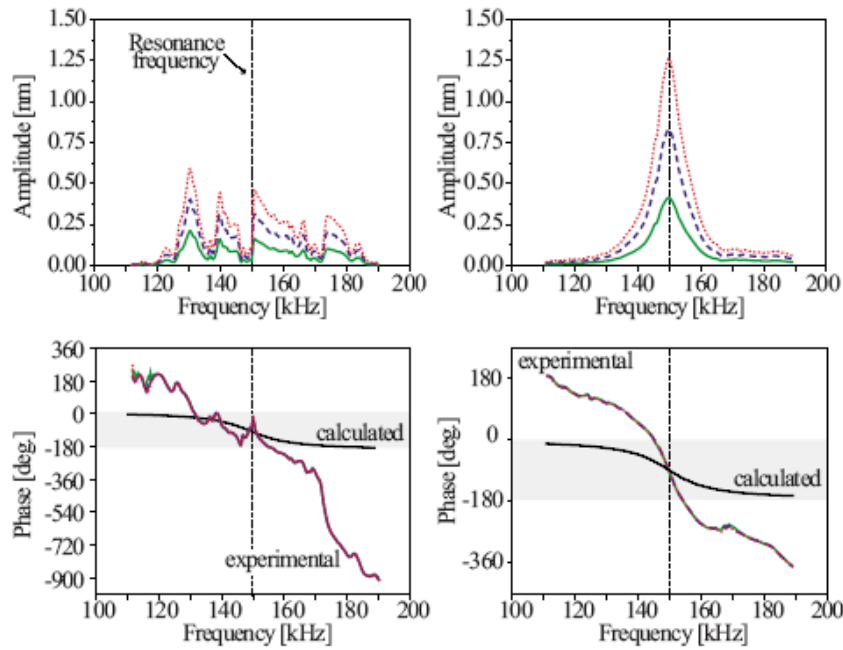


Figure 2.8 Cantilever holder design of Asakawa and Fukuma [47]

Asakawa and Fukuma considered the acoustic wave propagation from the piezoelectric actuator to the cantilever, and proposed a holder structure as shown in Figure 2.8 [47]. First, for suppressing the acoustic wave caused by the holder boundary stress, a PEEK holder body was placed between the piezoelectric actuator and the steel chip support. Second, the cantilever was excited by the flexure drive mechanism, which was achieved by a flexure hinge design as shown in Figure 2.8(c). Figure 2.9 shows the experimental results of their modified holder with two different holder materials. Figure 2.9(a) represents the bode plot with the steel holder body, and Figure 2.9(b) is the bode plot with the PEEK material. A single peak was captured on the PEEK holder successfully. However, the flexure drive mechanism caused the phase delay, which may need to be compensated for the FM-AFM and phase imaging.



(a) Bode plot on steel holder      (b) Bode plot on PEEK holder

Figure 2.9 Excitation spectrum comparison between two materials [47]

### 2.2.3 Cantilever detection system

The deformation of the cantilever has to be detected by a detection system. The resolution of the detection system affects the AFM force sensitivity directly. Besides, the bandwidth of the cantilever detection system also limits the scanning speed. Several detection methods are shown in Figure 2.10. The earliest method utilizes a STM tip to measure the tunneling current between the STM tip and the cantilever as shown in Figure 2.10(a) [4]. Utilizing the resistance variation of a piezoresistive cantilever, the cantilever deflection can be measured by a Wheatstone bridge as shown in Figure 2.10(b) [48]. This embedded piezoresistive sensor on the cantilever simplifies the alignment of the external detection sensor, but also complicates the cantilever manufacture. The capacitive sensor can also be integrated with the cantilever for applications of sensor arrays [49], but it is not suited for the large deflection and liquid

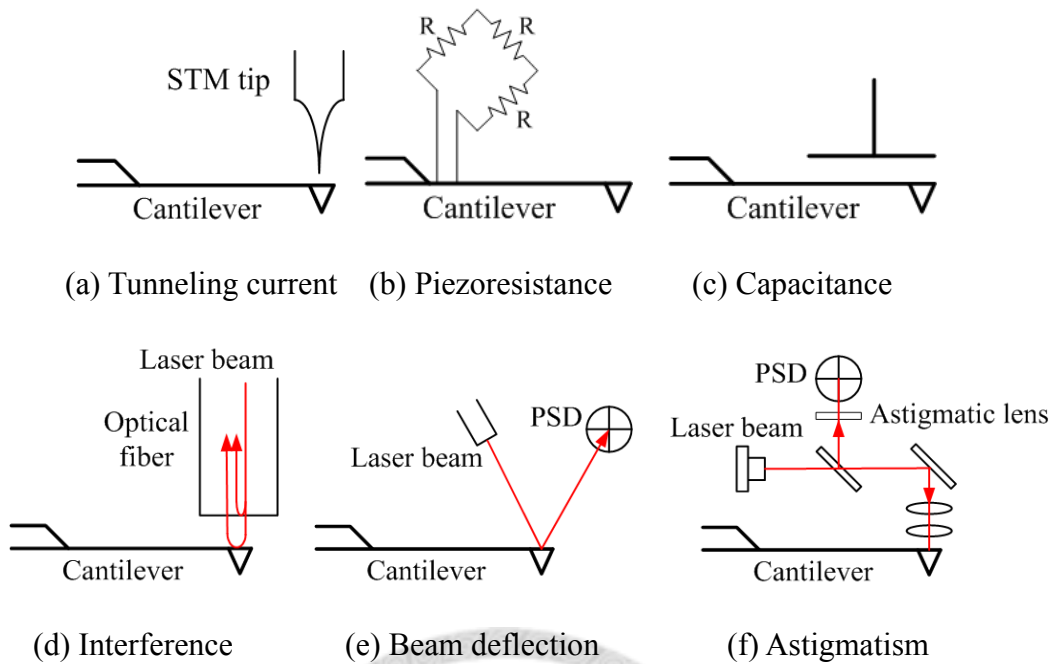


Figure 2.10 Cantilever detection methods

environment. Besides the electric methods, different optical methods are also utilized. Figure 2.10(d) shows the interferometry method using an optical fiber, and this method has high sensitivity and provides absolute displacement measurement [50]. This technique needs the complex signal processing and implementation cost, and positioning the optical fiber is also a demanding task. The optical beam deflection method is the most popular method, and its principle is illustrated in Figure 2.10(e) [51, 52]. In this method, a laser beam is focused on the cantilever, and the reflective beam is detected by a position sensing detector (PSD). Beam deflection method is sensitive to the cantilever angular variation, and provides both the cantilever flexural and torsional deflection signals. The astigmatic detection method is widely used in the digital versatile disk (DVD) pickup head. Figure 2.10(f) is a schematic setup for the cantilever detection [53, 54]. The vertical displacement and two-dimensional angular tilts of the cantilever can be detected in this method. Utilizing the commercial astigmatic pickup



head, an astigmatic detection system can be compact and cheap. Furthermore, it has small laser spot size and high bandwidth. The detailed comparison between beam deflection and astigmatic detection methods is discussed in Chapter 5.

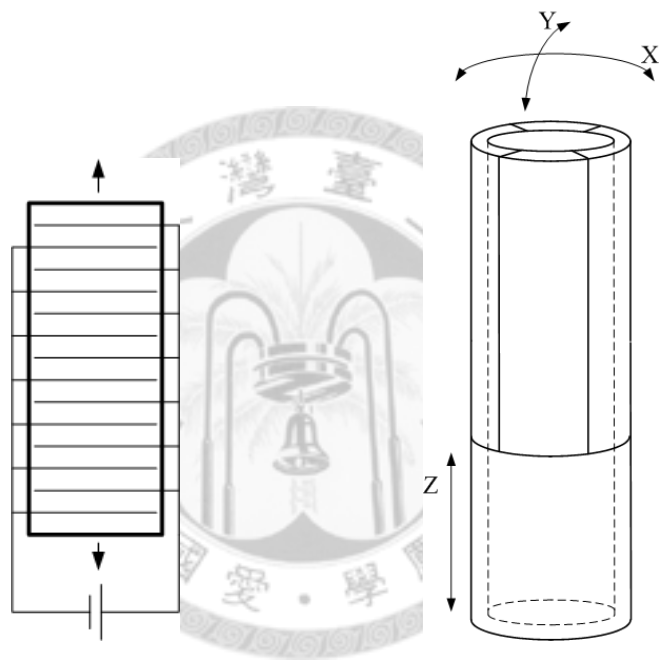
## 2.3 Actuator System

### 2.3.1 Scanner

The AFM scanner provides precise relative displacement between the cantilever tip and the sample. By moving either the tip or the sample, the AFM design can be classified to the scanning tip type or the scanning sample type roughly. For applications with small and light samples, the scanning sample type is preferred, because its bandwidth doesn't reduce much due to the weight of sample. On the other hand, the scanning tip type is suitable for the large and heavy sample. However, the affection on the cantilever detection system due to the movement has to be avoided.

Most AFM scanners use the piezoelectric material to achieve precise displacement. Piezoelectric ceramic material such as lead zirconate titanate (PZT) is a transducer between the electric charge and the mechanical force. The piezoelectric actuator can produce extension through applying voltage directly, and generates precise displacement. On the contrary, high input voltage is required for larger displacement. The multilayer piezoelectric stack increases the displacement by stacking piezoelectric actuators as shown in Figure 2.11(a). A three-axes scanner can be achieved by collocating three piezoelectric stacks with an appropriate mechanism. The piezoelectric tube is another common design for the AFM scanner. The piezoelectric tube has upper and lower sections as shown in Figure 2.11(b). The outside electrode of the upper section is divided into four segments, and its inner electrode is grounded. Each pair of opposite

electrodes provides one dimensional movement. Therefore, the upper section is responsible for the XY-axes movement, and the lower section controls the Z-axis extension. The tube scanner can provide the three-axes movement by one single structure, and simplifies the assembling problem. However, the XY-axes movement causes crosstalk on the Z-axis when the scanning area is far from the tube center. Another drawback of the tube scanner is the spacial limitation. The tube scanner occupies the bottom space of the sample, and the invert OM is not compatible.



(a) Multilayer piezoelectric stack      (b) Piezoelectric tube

Figure 2.11 Piezoelectric scanner

Although the piezoelectric actuator is precise and easy to use, nonlinear and changeable properties of the piezoelectric actuator should be reminded. Similar to the electromagnetic actuator, the hysteresis phenomenon also exhibits on the piezoelectric actuator. In the piezoelectric material, hysteresis is caused by crystalline polarization effects and the molecular friction. Figure 2.12 illustrates the hysteresis phenomenon, where the X-axis and Y-axis are the input voltage and output displacement respectively.

The hysteresis effect is related to operation parameters such as input amplitude, load, temperature, etc. This nonlinear property causes the image distortion problem as shown in Figure 2.13(a). The sample is a square grating with 3  $\mu\text{m}$  pitch and 20 nm height. The distortion of the square structures is obvious due to the hysteresis. Another issue is the scanner bandwidth, which limits the maximum scanning speed. Without the Z-axis feedback control, Figure 2.13(b) shows the cantilever deflection image of the same square grating with 800 line/sec scanning rate. Because the Z displacement of the scanner is constant, the deflection signal is proportional to the topography. The high scanning rate causes serious distortion and oscillation, and the scanning range also decreases. Except the scanner properties, the environmental temperature variation can induce a slow position drift due to the thermal expansion of the whole mechanism.

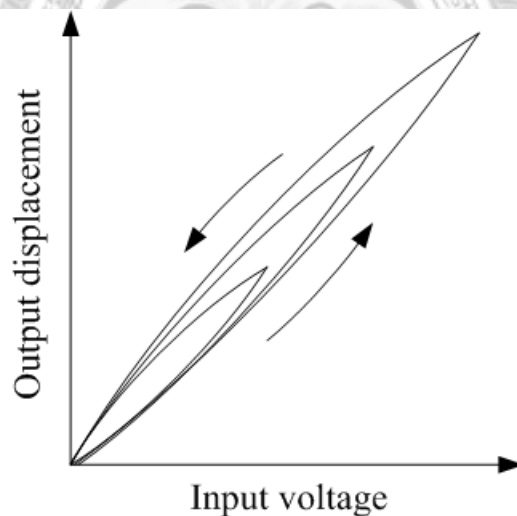
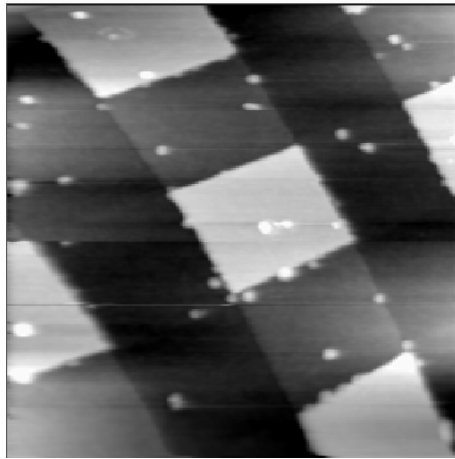
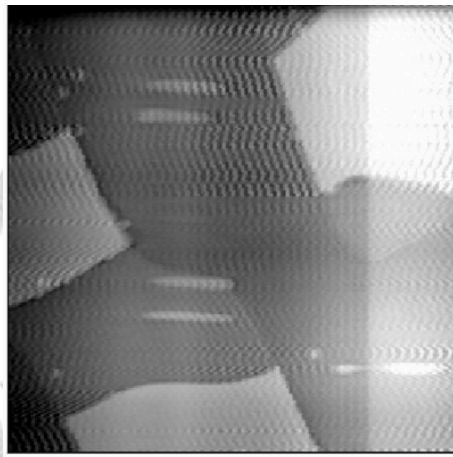


Figure 2.12 Piezoelectric hysteresis with different input amplitudes



(a) Topography image with scanning rate of 1 line/sec



(b) Deflection image with scanning rate of 800 line/sec

Figure 2.13 AFM images of calibration grating with 3  $\mu\text{m}$  pitch

Some nonlinear scanner properties can be solved by control methods. The open-loop control method calibrates the scanner displacement by adjusting the input driving signal. The upper diagram of Figure 2.14 is a typical calibrated driving waveform, and the output displacement becomes linear as the lower diagram. The open-loop calibration can solve the hysteresis phenomenon, but can't deal with the thermal drift problem.

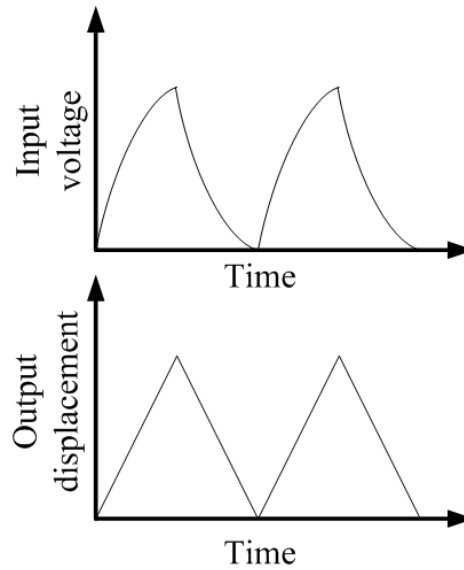
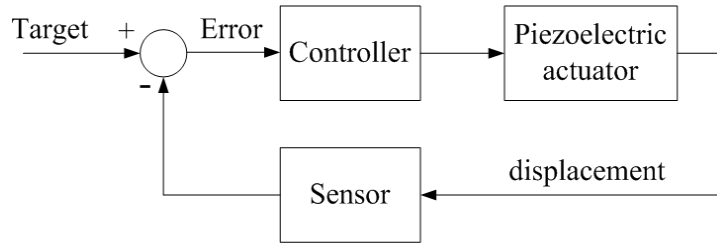
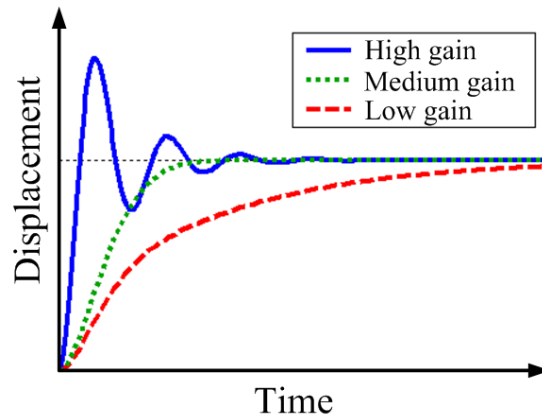


Figure 2.14 Open-loop scanner calibration

The closed-loop method performs an accurate positioning by a feedback control loop as shown in Figure 2.15(a). In this method, a position sensor detects the accurate displacement of the actuator. Then, the actuator displacement signal is compared with the target signal, and a controller compensates the driving signal to minimize the error signal. The proportional-integral-derivation (PID) controller is used in the AFM generally. For optimizing the performance, the PID gains should be adjusted for applications. Figure 2.15(b) demonstrates the step response with different controller gains setting. If the gains are too high, the overshooting occurs and causes an oscillation. On the contrast, the settling time will be extended when the gains are reduced. The closed-loop is helpful for the applications that need accurate positioning. However, the essential position sensor also complicates the scanner design, and the sensor noise restricts the scanning resolution.



(a) System block diagram



(b) Step response with different controller gains

Figure 2.15 Closed-loop scanner control

### 2.3.2 Z-axis approaching system

Before scanning, the cantilever tip must approach the sample surface into the scanner range. This step can be achieved by manual operation or a motorized system. The stepper motor system is easy to control the displacement, and is widely used for approaching. Two considerations here are the tip colliding and time consumption, and two tactics are introduced as follows.

In the continuous approaching method, the Z-axis scanner and the stepper motor work simultaneously. The Z-axis feedback controller monitors the tip-sample interactive force during the stepper motor running. When the tip contacts with the sample, the scanner will draw back. After the scanner retracting to its half range, the stepper motor stops. In this method, the motor speed and feedback parameters must be adjusted

appropriately. Otherwise, the impact force could damage the tip at the contact instant.

In the alternate approaching method, the Z-axis scanner and the stepper motor work alternately. After the stepper motor running a small distance, the force-displacement curve is performed to detect the tip-sample distance. Similarly, this loop stops when the sample is located around the half range of the scanner. The alternate approaching method can avoid large interactive force during approaching. However, it cost more time than the continuous approaching method. For improving the approaching efficiency, an OM can monitor the tip-sample distance roughly. First, the tip is brought close to the sample rapidly with the OM monitor. Then, the alternate approaching method is adopted.

## 2.4 Control System

Various functions such as the scanning and the force-displacement curve measurement are controlled by the control system. The digital control system is flexible for adjusting parameters, and is adopted in most AFM systems. In the tapping mode AFM, the lock-in amplifier is necessary for getting the cantilever amplitude and phase signals. The Z-axis feedback control collaborates with the XY-axes scanning function for measuring the surface image.

### 2.4.1 Lock-in amplifier

Figure 2.16 illustrates the principle of a digital lock-in amplifier. The sinusoidal driving signal with frequency  $\omega$  is generated by a direct digital synthesizer (DDS), and transferred to the excitation source after a digital-to-analog converter (DAC). For simplification, the supposed cantilever response is an ideal sinusoidal wave with amplitude  $A$  and phase shift  $\theta$ . For measuring  $A$  and  $\theta$ , the cantilever response signal is

multiplied by  $\sin(\omega t)$  and  $\cos(\omega t)$ , respectively. After a low pass filter (LPF), the remaining dc terms  $x$  and  $y$  represent the Cartesian coordinates of the point on the unit circle. Therefore,  $A$  and  $\theta$  can be calculated by trigonometric functions. In practice, these signal processing can be realized by the field-programmable gate array (FPGA) or the digital signal processor (DSP). During scanning, the cantilever response could not be an ideal sinusoidal wave due to the complex interactive force with the sample. Lowering the cutoff frequency of LPF can reduce the noise, but the bandwidth is also reduced.

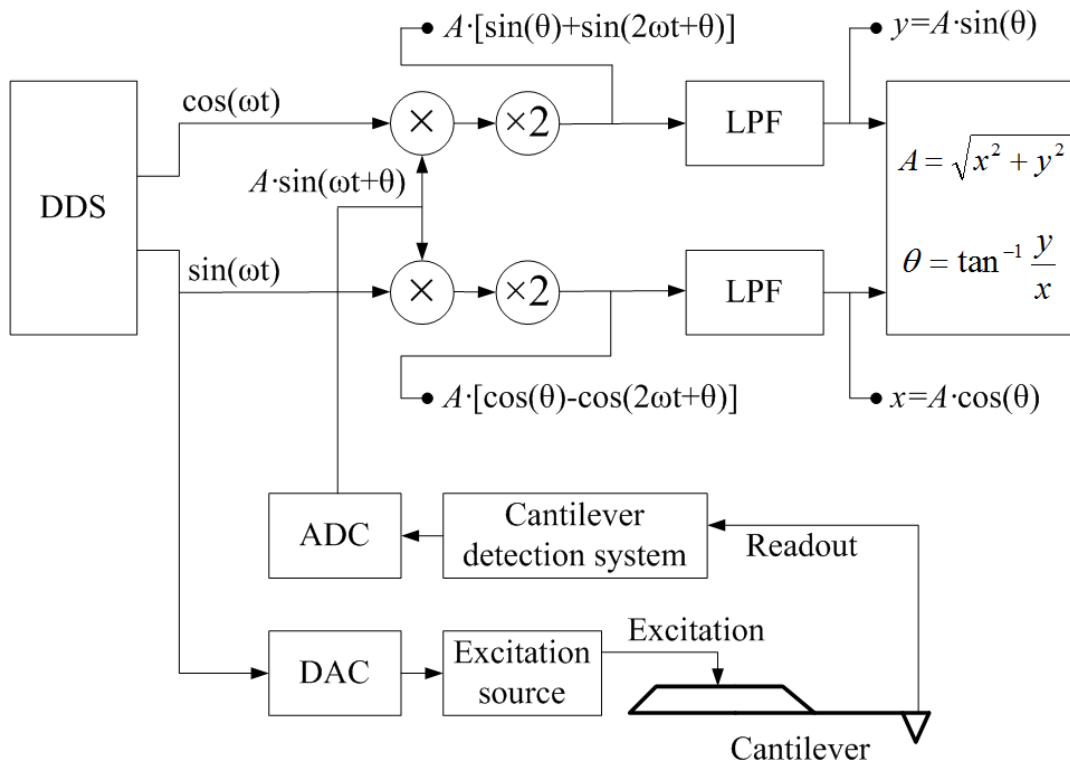


Figure 2.16 Digital lock-in amplifier diagram

## 2.4.2 Z-axis feedback control

The Z-axis feedback controller is responsible for adjusting the interactive force between the tip and the sample. Figure 2.17 presents a Z-axis feedback loop. At first, user determines the setpoint, which is the tracking value of the reference signal. The



reference signal depends on the operation mode. In the contact mode, the cantilever deflection signal is selected for reference. In the dynamic mode, the amplitude, the phase, or the frequency signal can be adopted. The error between the setpoint and the reference signal is inputted to a PID controller, and the driving signal to the Z-axis scanner is generated. The Z-axis displacement of the scanner is adjusted to minimize the error signal. During the scanning, the tip-sample distance can be kept constant, and the Z-axis displacement represents the topography of the sample. Similar to the closed-loop scanner control, the PID gains should be adjusted to optimize the tracking performance. However, this adjustment is much difficult in the Z-axis feedback control than the closed-loop scanner control. In the closed-loop scanner, only the sample weight changes. On the other hand, the tip and sample system is complicated. Various interactive forces such as the mechanical contact force, van der Waals force, electrostatic force and capillary force exist between the tip and the sample. Besides, the tip geometry, environmental humidity, pressure, temperature and sample material also affect these interactive forces. Therefore, the scanning parameters are adjusted according to the scanning conditions.

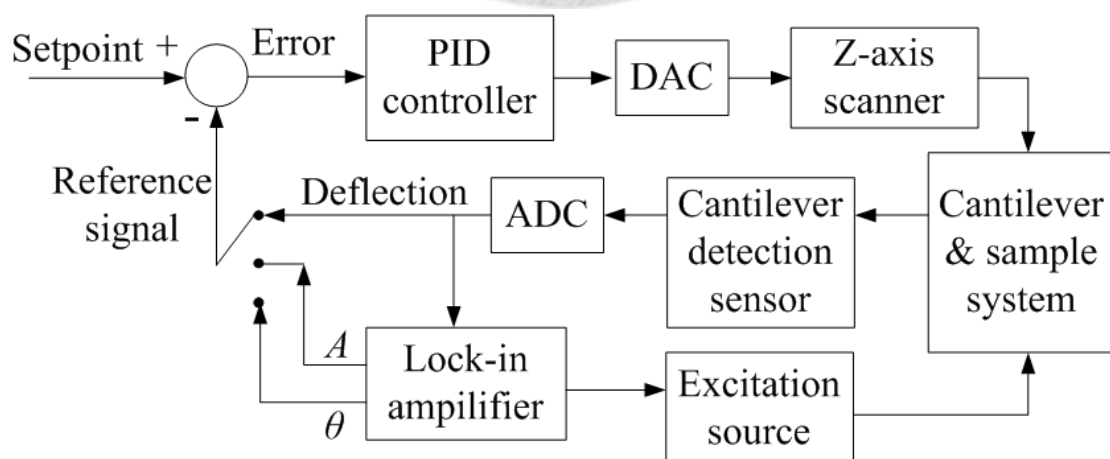


Figure 2.17 Z-axis feedback control diagram

### 2.4.3 XY-axes scanning control

The XY-axes scanning control is used for measuring an area data. The raster scan is the most common method, and Figure 2.18(a) shows its trajectory on the XY plane. In this case, X-axis is the fast axis, which moves forward and backward. Then the slow Y-axis moves to the next line. A square area can be scanned after repeating these two steps. This method is intuitional and easy to program. The surface information can be presented in a two dimensional array, which is easy for the image process and display. However, the triangular waveform of the fast axis contains harmonic terms with higher frequencies. It is unfavorable for the high speed scanning, and could induce oscillations easily.

Another method called the spiral scan method is proposed for high speed applications [55]. The cosine and sine signals with varying amplitudes are applied to X-axis and Y-axis, and produce a spiral trajectory as shown in Figure 2.18(b). The spiral trajectory without suddenly direction change is more suitable for the high speed scanning. However, the image process and the pixel mapping on the monitor become more complicated.

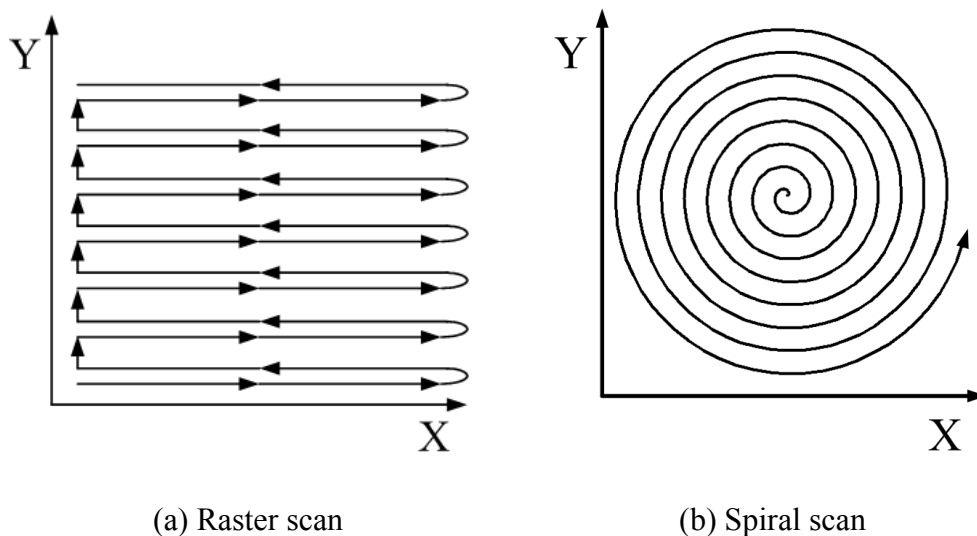


Figure 2.18 XY-axes scanning control

## Chapter 3

### Cantilever Force Sensor

The cantilever tip is a sensitive force sensor in the AFM, and its dynamic properties in liquid are significant for scanning speed and quality. In this chapter, the dimensional effect and high order resonances of the cantilever are discussed theoretically and experimentally.

#### 3.1 Cantilever Dimensional Effect

##### 3.1.1 Theoretical calculation

The rectangular cantilever has a uniform cross-section and is the most common geometric design for the AFM. The governing equation of the cantilever deflection is derived under several assumptions as follows: (1) The cross-section is uniform; (2) The cantilever length is greatly larger than its width; (3) The cantilever is isotropic, linear, and elastic material; (4) The cantilever deflection is far smaller than the cantilever dimensions. According to the Euler–Lagrange equation [56], the dynamic deflection of the cantilever is expressed as Equation (3.1)

$$EI \frac{\partial^4 w(x,t)}{\partial x^4} + \rho_c b h \frac{\partial^2 w(x,t)}{\partial t^2} = f(x,t), \quad (3.1)$$

where  $E$  is the Young's modulus of the cantilever,  $I$  is the moment of inertia of the cantilever,  $\rho_c$  is the cantilever density,  $b$  and  $h$  are the width and the thickness of the cantilever,  $x$  is the spatial coordinate along the cantilever length,  $t$  is time,  $w(x,t)$  is the cantilever flexural deflection, and  $f(x,t)$  is the external applied force per unit length. Utilizing the separation of variables,  $w(x,t)$  is separated into the time and spatial variables as

$$w(x,t) = W(x)T(t), \quad (3.2)$$

where  $W(x)$  is the shape function, and  $T(t)$  is the time-dependent function. Considering the case of an undamping free vibration without the external force  $f(x,t)$ , Equation (3.3) is obtained by substituting Equation (3.2) into Equation (3.1):

$$\frac{EI}{\rho_c bh W(x)} \frac{d^4 W(x)}{dx^4} + \frac{1}{T(t)} \frac{d^2 T(t)}{dt^2} = 0. \quad (3.3)$$

The solution of  $T(t)$  must be periodic. Assuming the radial resonant frequency of the cantilever in vacuum is  $\omega_{vac}$ ,  $W(x)$  and  $T(t)$  can be solved by

$$\frac{EI}{\rho_c bh W(x)} \frac{d^4 W(x)}{dx^4} = -\frac{1}{T(t)} \frac{d^2 T(t)}{dt^2} = \omega_{vac}^2. \quad (3.4)$$

Substituting the boundary conditions at the clamped fix end and the free end, the shape function is obtained:

$$W(x) = \sin \frac{C_n}{L} x - \sinh \frac{C_n}{L} x - \left( \frac{\sin C_n + \sinh C_n}{\cos C_n + \cosh C_n} \right) \left( \cos \frac{C_n}{L} x - \cosh \frac{C_n}{L} x \right), \quad (3.5)$$

where

$$C_n^2 = \sqrt{\frac{\rho_c bh}{EI}} L^2 \omega_{vac}^2, \quad (3.6)$$

which satisfies the equation

$$1 + \cos C_n \cosh C_n = 0. \quad (3.7)$$

Equation (3.7) has infinite solutions  $C_n$ . Therefore, infinite shape functions  $W(x)$  exist, and represent different order resonances. The corresponded resonant frequency of the  $n$ th order resonance in vacuum is given by

$$\omega_{vac,n} = \frac{C_n^2}{L^2} \sqrt{\frac{EI}{\rho_c bh}} = \frac{C_n^2 h}{\sqrt{12} L^2} \sqrt{\frac{E}{\rho_c}}. \quad (3.8)$$

where  $L$  is the length of the cantilever. For an incompressible fluid environment, Sader introduced a hydrodynamic load into Equation (3.1) [57]. Through the Fourier transform of Equation (3.1), the dynamic equation becomes

$$EI \frac{d^4 W(x, \omega)}{dx^4} - \rho_c b h \omega^2 W(x, \omega) = F(x, \omega), \quad (3.9)$$

where  $\omega$  represents the vibrational frequency, and the external force is distinguished into two contributions:

$$F(x, \omega) = F_{hydro}(x, \omega) + F_{drive}(x, \omega), \quad (3.10)$$

where  $F_{hydro}(x, \omega)$  and  $F_{drive}(x, \omega)$  are the hydrodynamic load and the drive force, respectively. Based on the equations of motion for fluid, the general form of  $F_{hydro}(x, \omega)$  is given by

$$F_{hydro}(x, \omega) = \frac{\pi}{4} \rho_f \omega^2 b^2 \Gamma(\kappa, Re) W(x, \omega), \quad (3.11)$$

where  $\rho_f$  is the fluid density, and  $\Gamma(\kappa, Re)$  is the dimensionless hydrodynamic function, which depends on the Reynolds number  $Re$  and the aspect ratio  $\kappa$ :

$$Re = \frac{\rho \omega b^2}{\mu}, \quad (3.12)$$

$$\kappa = C_n \frac{b}{L}, \quad (3.13)$$

where  $\mu$  is the viscosity of the fluid. According to the Navier-Stokes equation,  $\Gamma(\kappa, Re)$  is given by [58,59]

$$\Gamma(\kappa, Re) = 8a_1, \quad (3.14)$$

where the coefficient  $a_1$  is solved by the linear equations

$$\sum_{m=1}^M (A_{q,m}^{\kappa} + A_{q,m}^{Re}) a_m = \begin{cases} 1, & q = 1 \\ 0, & q > 1 \end{cases}, \quad (3.15)$$

where the integer  $M$  must be large enough to obtain a convergent solution, and  $A_{q,m}^{\kappa}$  and  $A_{q,m}^{Re}$  are the terms of Meijer  $G$  functions:

$$A_{q,m}^{\kappa} = -\frac{4^{2q-1}}{\sqrt{\pi}} G_{13}^{21} \left( \frac{\kappa^2}{16} \middle| \begin{matrix} 3/2 \\ 0 & q+m-1 & q-m+1 \end{matrix} \right), \quad (3.16)$$

$$A_{q,m}^{\kappa} = -\kappa^2 \frac{2^{4q-5}}{\sqrt{\pi}} G_{13}^{21} \left( \begin{matrix} \kappa^2 - i \operatorname{Re} \\ 16 \end{matrix} \middle| \begin{matrix} 1/2 \\ 0 \end{matrix} \begin{matrix} q+m-2 \\ q-m \end{matrix} \right) \\ - \frac{2^{4q-1}}{\sqrt{\pi}} G_{13}^{21} \left( \begin{matrix} \kappa^2 - i \operatorname{Re} \\ 16 \end{matrix} \middle| \begin{matrix} 1/2 \\ 0 \end{matrix} \begin{matrix} q+m-1 \\ q-m+1 \end{matrix} \right). \quad (3.17)$$

Substituting Equations (3.10) and (3.11) into Equation (3.9), the dynamic equation becomes

$$\frac{d^4 W(x, \omega)}{dx^4} - \frac{\rho_c b h \omega^2}{EI} \left( 1 + \frac{\pi \rho_f b}{4 \rho_c h} \Gamma(\kappa, \operatorname{Re}) \right) W(x, \omega) = \frac{F_{drive}(x, \omega)}{EI}. \quad (3.18)$$

For calculating the resonant frequency in fluid,  $F_{drive}(x, \omega)$  is neglected, and Equation (3.8) is substituted into Equation (3.18) to obtain

$$\frac{d^4 W(x, \omega)}{dx^4} - \frac{C_n^4 \omega^2}{L^4 \omega_{vac,n}^2} \left( 1 + \frac{\pi \rho_f b}{4 \rho_c h} \Gamma(\kappa, \operatorname{Re}) \right) W(x, \omega) = 0. \quad (3.19)$$

Neglecting dissipative effects, the relation between the resonant frequencies in fluid  $\omega_{fluid}$  and vacuum  $\omega_{vac}$  is described by

$$\frac{\omega_{fluid}}{\omega_{vac}} = \left( 1 + \frac{\pi \rho_f b}{4 \rho_c h} \Gamma_r(\kappa, \operatorname{Re}) \right)^{-1/2}, \quad (3.20)$$

and the Q-factor is

$$Q = \frac{(4 \rho_c h / \pi \rho_f b) + \Gamma_r(\kappa, \operatorname{Re})}{\Gamma_i(\kappa, \operatorname{Re})}, \quad (3.21)$$

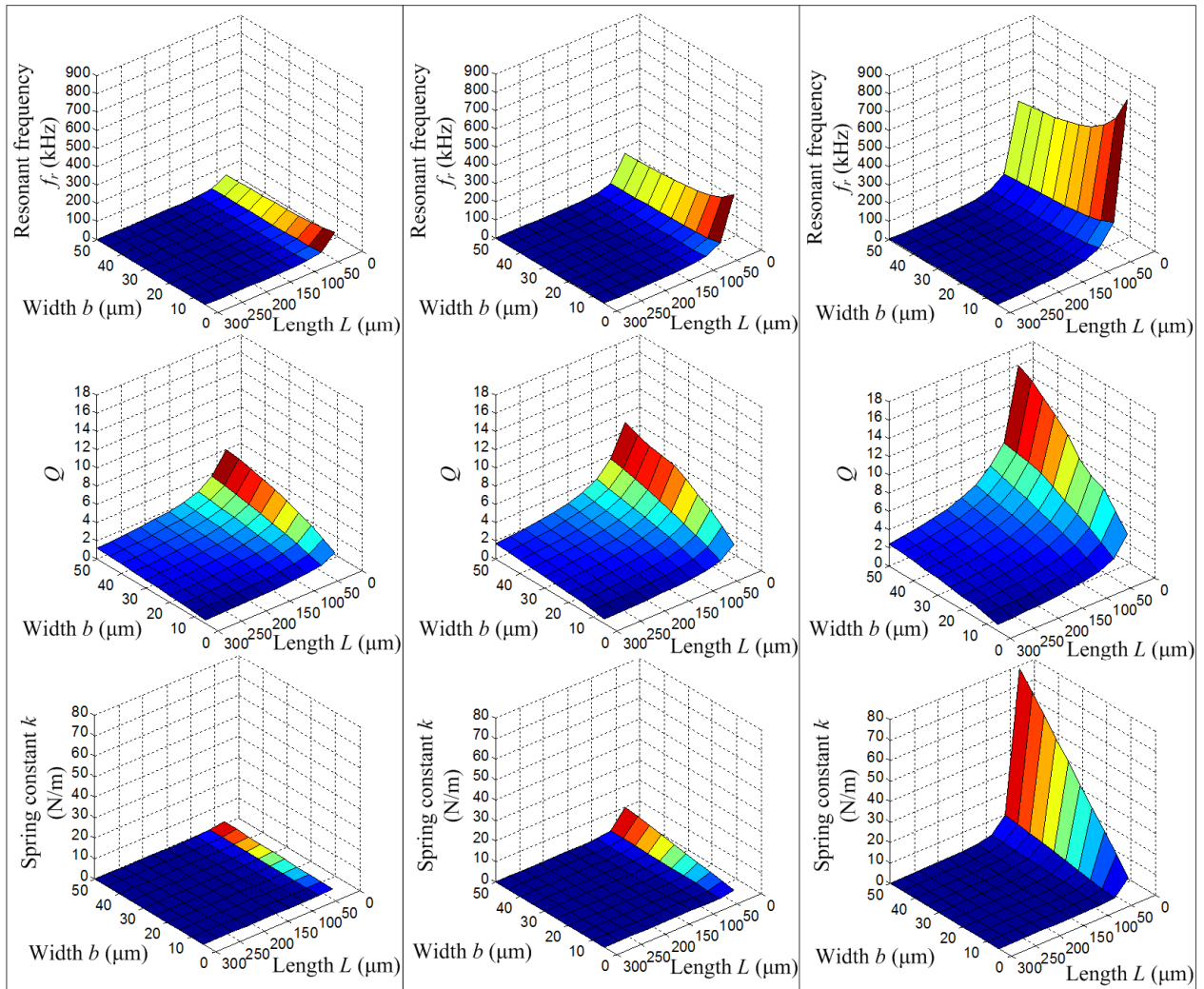
where the subscript  $r$  and  $i$  refer to the real and imaginary components of  $\Gamma(\kappa, \operatorname{Re})$ . For numerical calculation of a silicon cantilever in water, the values of the parameters are listed in Table 3.1. For calculating  $\operatorname{Re}$  initially, the frequency in Equation (3.12) is evaluated by

$$\omega = \omega_{vac,n} \left( 1 + \frac{\pi \rho_f b}{4 \rho_c h} \right)^{-1/2}. \quad (3.22)$$

Table 3.1 Numerical values of parameters

Symbol	Description	Value
$E$	Young's modulus of cantilever	$169 \times 10^9 \text{ N/m}^2$
$C_1$	Dimensionless number of first resonance	1.8751
$\rho_c$	Cantilever density	$2330 \text{ kg/m}^3$
$L$	Length of cantilever	$30 \sim 300 \mu\text{m}$
$b$	Width of cantilever	$5 \sim 50 \mu\text{m}$
$h$	Thickness of cantilever	$0.25 \sim 1 \mu\text{m}$
$I$	Moment of inertial of cantilever	$b \cdot h^3 / 12$
$k$	Spring constant of cantilever	$Ebh^3 / 4L^3$
$\mu$	Viscosity of water	$8.94 \times 10^{-4} \text{ Pa}\cdot\text{s}$ (at $25 \text{ }^\circ\text{C}$ )
$\rho_f$	Density of water	$997 \text{ kg/m}^3$ (at $25 \text{ }^\circ\text{C}$ )
$M$	Number of summation in Equation (3.15)	10

The resonant frequency  $f_r$  in hertz, the Q-factor  $Q$ , and the spring constant  $k$  of the cantilever are calculated under different cantilever length  $L$ , width  $b$ , and thickness  $h$ . Figures 3.1(a), (b), and (c) present the cantilever properties with the cantilever thicknesses  $h$  of  $0.25 \mu\text{m}$ ,  $0.5 \mu\text{m}$ , and  $1 \mu\text{m}$ , respectively. The longer cantilever has smaller  $k$ , but lower  $f_r$  and  $Q$ . Broadening the cantilever width can increase the  $Q$ , but reduces  $f_r$  and raises  $k$ . The thicker cantilever not only increases  $f_r$  and  $Q$ , but also raises  $k$ . Therefore,  $f_r$ ,  $Q$ , and  $k$  can't be improved simultaneously through modifying any single dimension of the cantilever directly.



(a)  $h = 0.25 \mu\text{m}$

(b)  $h = 0.5 \mu\text{m}$

(c)  $h = 0.1 \mu\text{m}$

Figure 3.1 Cantilever properties versus cantilever dimensions

According to Equation (2.1), the spring constant  $k$  is dominated by the cantilever length  $L$  and thickness  $h$ . Therefore,  $k$  can be kept constant through fixing the  $L$  to  $h$  ratio and the width  $b$ . Figure 3.2 shows the cantilever properties with  $L/h = 100$  and  $b = 5 \mu\text{m}$ . The result shows that the resonant frequency  $f_r$  and the Q-factor can be increased through decreasing  $h$  and  $L$  proportionally.



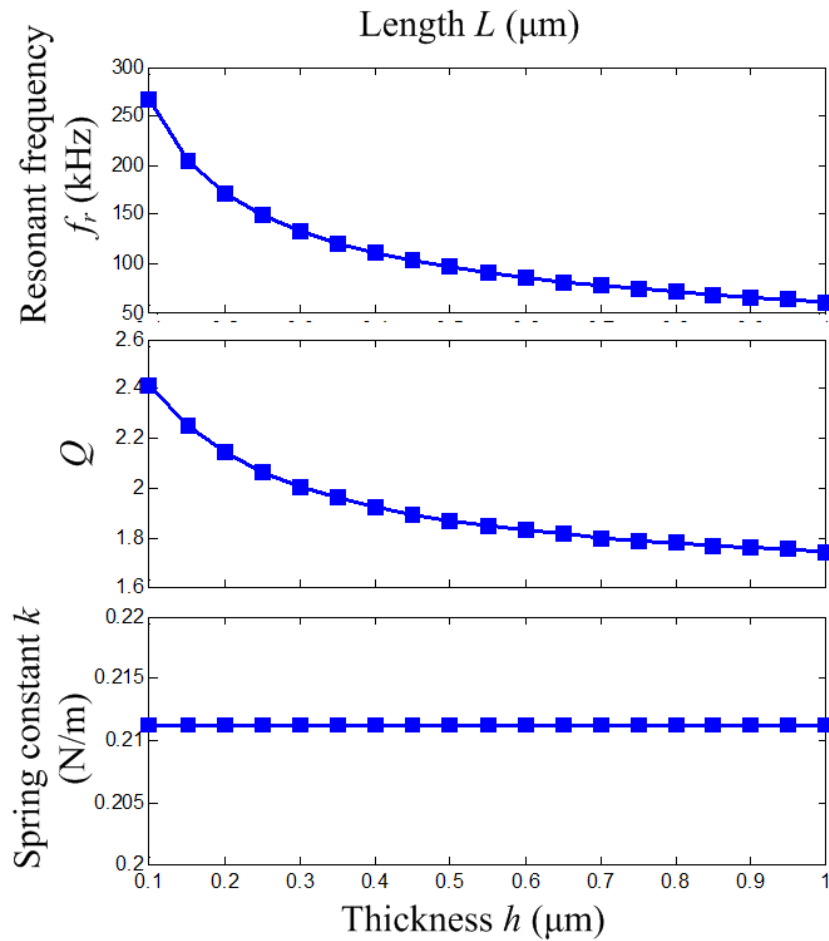
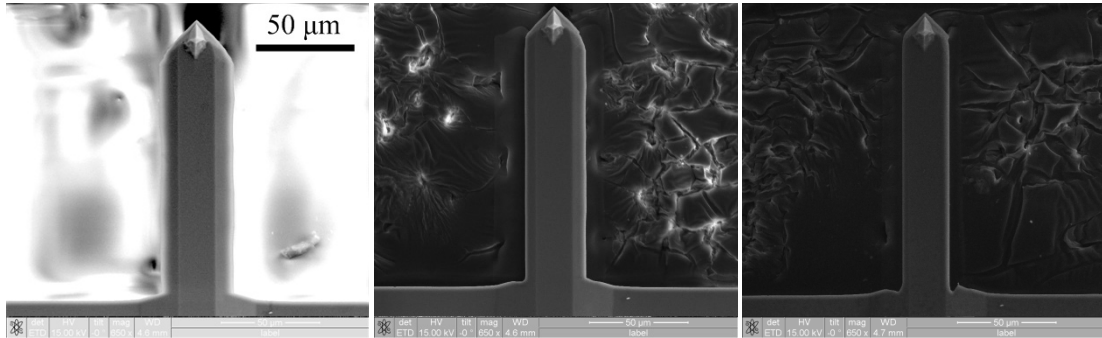


Figure 3.2 Cantilever properties with  $L/h = 100$  and  $b = 5 \mu\text{m}$

### 3.1.2 Experimental results

For examining the cantilever dimensional effects, the width and the length of cantilevers are modified. The manufacturing process is performed in a dual beam focused ion beam (FIB) system (NOVA-600, FEI). The cantilever material is removed through Gallium ions collision in a vacuum condition. For eliminating the individual difference between cantilevers, the measurement and modification are repeated on an identical cantilever. Figure 3.3 shows a commercial cantilever (PPP-NCHAuD, NANOSENSORS), which is modified from the widths of  $37 \mu\text{m}$  to  $14 \mu\text{m}$ . The

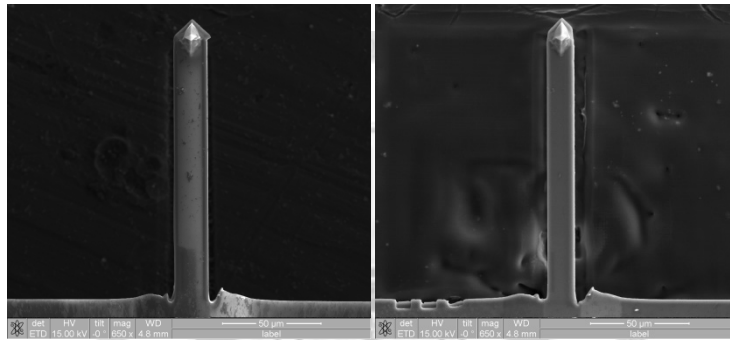
cantilever length (138  $\mu\text{m}$ ) and thickness (4  $\mu\text{m}$ ) are measured by SEM. The cantilever has an Au coating on the detector side of the cantilever for increasing the reflectivity.



(a)  $b = 37 \mu\text{m}$

(b)  $b = 31 \mu\text{m}$

(c)  $b = 24 \mu\text{m}$



(d)  $b = 17 \mu\text{m}$

(e)  $b = 14 \mu\text{m}$

Figure 3.3 Cantilever No.02 with different widths

For measuring the resonant frequency and the Q-factor in air and water, a commercial AFM (MultiMode, Bruker) is utilized. Without external excitation, the thermal fluctuation spectrum is acquired through the fast Fourier transform (FFT) of the cantilever deflection signal. The resonant frequency  $f_{r,wm}$  with width-modification and the Q-factor are calculated from the fitting curve of the thermal fluctuation spectrum. The sum voltage  $U_{sum}$  of the PSD represents the laser intensity on the PSD. Two cantilevers (cantilever No.01 and No.02) are measured in the same process, and the results are listed in Table 3.2.

Table 3.2 Experimental results of various widths

Cantilever No.01	Air			Water		
Width $b$ ( $\mu\text{m}$ )	Resonant frequency with width-modification $f_{r,wm}$ (kHz)	$Q$	$U_{sum}$ (V)	Resonant frequency with width-modification $f_{r,wm}$ (kHz)	$Q$	$U_{sum}$ (V)
37	251	478	6.5	124	NA	6.0
28	249	511	6.8	137	7.6	5.0
22	246	495	6.0	144	6.9	4.8
19	240	476	5.8	146	6.5	3.7
14	235	402	5.0	151	5.4	3.0
Cantilever No.02	Air			Water		
Width $b$ ( $\mu\text{m}$ )	Resonant frequency with width-modification $f_{r,wm}$ (kHz)	$Q$	$U_{sum}$ (V)	Resonant frequency with width-modification $f_{r,wm}$ (kHz)	$Q$	$U_{sum}$ (V)
37	257	457	5.0	128	7.7	6.1
31	255	535	6.8	136	7.5	5.4
24	253	485	6.1	146	7.3	4.9
17	241	368	5.8	149	6.8	3.5
14	233	338	5.2	152	5.6	3.0

Figure 3.4 compares the theoretical calculation with the experimental results. The results of the calculation and the experiment are close, but a larger error occurs when the cantilever width is narrow. The error may exist both in the calculation and experiment. In the theoretical calculation, the tip mass is neglected, and causes an over-estimation on the resonant frequency. Besides, the cantilever free end is triangular, and the original cross-section is trapezoid. Therefore, the cantilever geometry is not perfect rectangular. In the experiment, the sum voltage on the PSD reduces when the width becomes narrow, because the laser can't be reflected entirely. This effect could

causes a lower signal to noise ratio in the thermal fluctuation spectrum, but doesn't affect the measurement of the resonant frequency.

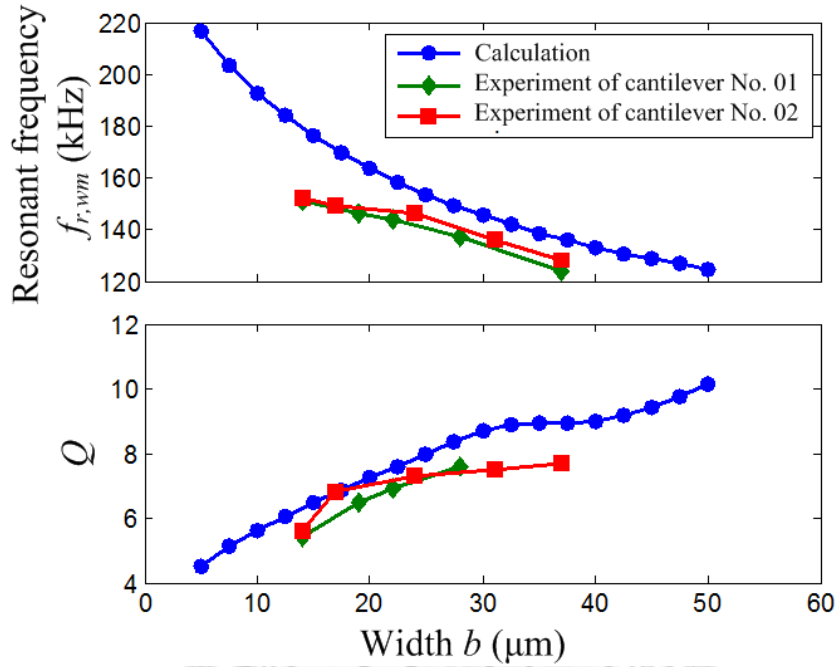
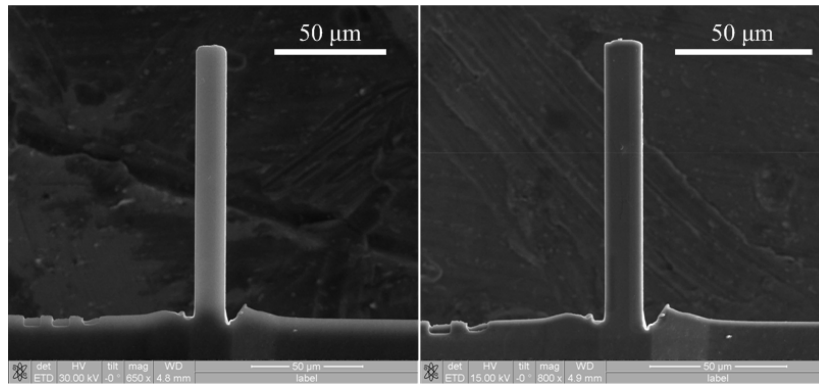


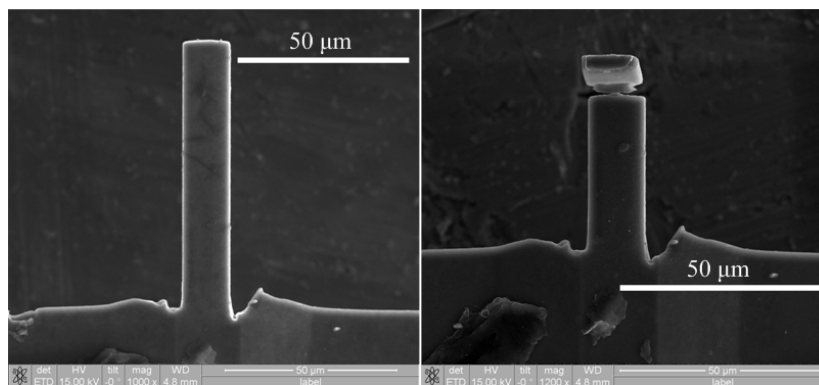
Figure 3.4 Cantilever properties versus cantilever width in water

Further, the lengths of the cantilever No.01 and No.02 are modified. As shown in Figure 3.5, the length of the cantilever No.02 is modified from 122  $\mu\text{m}$  to 38  $\mu\text{m}$ , and its width and thickness are 14  $\mu\text{m}$  and 4  $\mu\text{m}$ . The tip on the free end is removed. Besides, the trapezoid cross-section is also been eliminated after the width modification. Therefore, the cantilever is more approximate to the ideal rectangular model. The experimental results are listed in Table 3.3.



(a)  $L = 122 \mu\text{m}$

(b)  $L = 102 \mu\text{m}$



(c)  $L = 79 \mu\text{m}$

(d)  $L = 38 \mu\text{m}$

Figure 3.5 Cantilever No.02 with different lengths

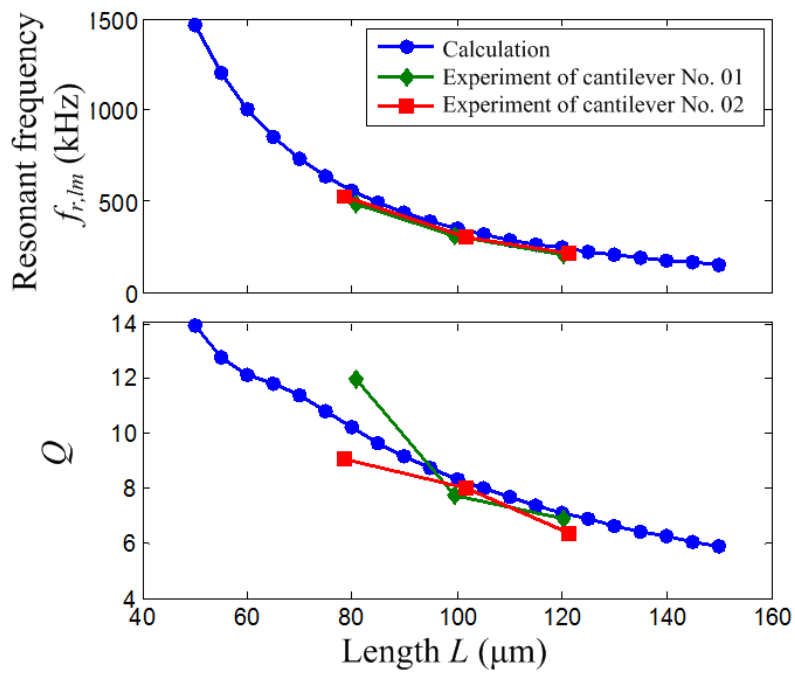


Figure 3.6 Dynamic properties versus cantilever length in water

The experimental results are listed in Table 3.3. The comparison between the calculation and experimental results are shown in Figure 3.6. The results of the calculation and experiment are close. However, the resonant peak can't be recognized when the length is reduced to 38  $\mu\text{m}$ . In air, the resonant frequency may be higher than the bandwidth of the commercial AFM. Besides, the magnitude of the thermal fluctuation may be too small for detection.

Table 3.3 Influence of cantilever length on dynamic properties

Cantilever No.01	Air			Water		
Length $L$ ( $\mu\text{m}$ )	Resonant frequency with length-modification $f_{r,lm}$ (kHz)	$Q$	$U_{sum}$ (V)	Resonant frequency with length-modification $f_{r,lm}$ (kHz)	$Q$	$U_{sum}$ (V)
120	330	540	4.6	207	6.86	2.5
100	489	540	4.2	310	7.74	2.5
81	745	651	2.6	483	11.97	2.2
38	NA	NA	4.2	NA	NA	2.3
Cantilever No.02	Air			Water		
Length $L$ ( $\mu\text{m}$ )	Resonant frequency with length-modification $f_{r,lm}$ (kHz)	$Q$	$U_{sum}$ (V)	Resonant frequency with length-modification $f_{r,lm}$ (kHz)	$Q$	$U_{sum}$ (V)
122	330	480	4.8	208	6.37	2.4
102	471	438	3.7	302	7.99	2.3
79	802	457	4.5	525	9.04	2.4
38	NA	NA	3.5	NA	NA	2.3

Although the mechanical properties can be improved through reducing the cantilever dimensions. However, the detective laser spot size limits the cantilever length

and width. Therefore, the cantilever area is reduced through manufacturing holes on the middle of the cantilever. The designed cantilever geometry is illustrated in Figure 3.7. A commercial cantilever tip (CSC38B, MikroMasch) has a length of 350  $\mu\text{m}$ , width of 35  $\mu\text{m}$ , and thickness of 1  $\mu\text{m}$ . The hole diameter is 20  $\mu\text{m}$ , and the distance between the holes is 50  $\mu\text{m}$ . For reducing the time consumption, six cantilevers with close resonant frequencies are chosen for experiments.

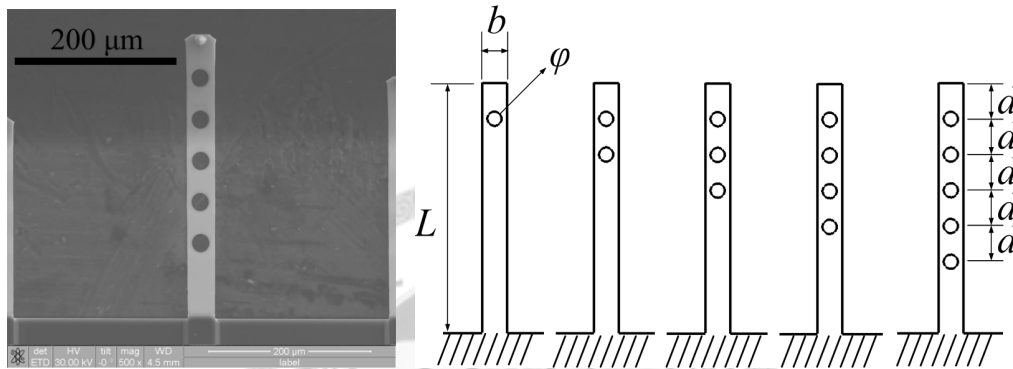


Figure 3.7 Modified cantilever with different hole layouts

A commercial AFM (MultiMode, Bruker) is utilized to measure the resonant frequency and the Q-factor in air and water. The results are listed in Table 3.4.

Table 3.4 Influence of number of holes on dynamic properties

Number of holes	Air			Water	
	Resonant frequency without modification $f_r$ (kHz)	Resonant frequency with hole-modification $f_{r,hm}$ (kHz)	$Q$	Resonant frequency with hole-modification $f_{r,hm}$ (kHz)	$Q$
0	11.27	11.27	66.8	3.95	2.2
1	11.21	11.61	67.3	4.18	2.0
2	11.05	11.62	57.1	4.05	1.9
3	11.23	11.70	61.4	4.16	1.9
4	11.03	11.04	56.2	4.08	1.8
5	11.39	10.58	55.3	3.91	1.7

Figure 3.8 shows the resonant frequencies in both air and water. The results show that the slight frequency shifts are less than 1 kHz. In air, the resonant frequencies increase when the number of the holes is below three. This phenomenon may be caused by the reduction of the equivalent mass. On the other hand, the resonant frequency decreases on the cantilever with five holes. This result could be explained by the reduction of the spring constant, because the location of the additional hole is close to the fixed end. In water, the frequency variation is below 200 Hz without an obvious tendency. Comparing with the width and length variation, the holes have insignificant affection to the cantilever in water.

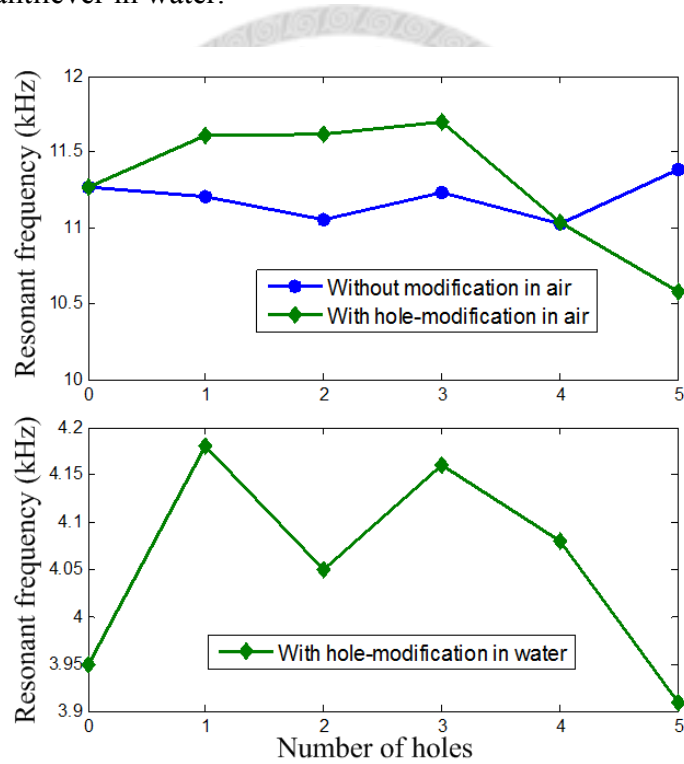


Figure 3.8 Resonant frequency versus number of holes

### 3.2 High Order Resonances

The resonant frequencies of high order resonances are higher than that of the fundamental resonance. The dynamics of high order resonances is more complicated for



AFM scanning. Therefore, the mass variation is utilized for studying their dynamic properties, and also implies an application for mass sensing in liquid environment.

### 3.2.1 Mass sensitivity in air

Cantilever-based mass sensors have been widely applied in bio-chemical examination. When molecules attach to the cantilever, the additional mass bends the cantilever and shifts the resonant frequency of the cantilever as well. The detective methods can be distinguished into the static mode and the dynamic mode. In the static mode, the mass variation  $\Delta m$  is calculated by the cantilever bending through the Hooke's law. In the dynamic mode, the mass variation  $\Delta m$  can be derived by detecting the shift of the resonant frequency as

$$\Delta m = \frac{k}{4\pi^2} \left( \frac{1}{(f_r + \Delta f)^2} - \frac{1}{f_r^2} \right), \quad (3.23)$$

where  $k$  is the cantilever spring constant,  $f_r$  is the original resonant frequency, and  $\Delta f$  is the frequency shift after mass variation. In order to maintain its linear association, the reacting region with the mass attachment is confined to the free end of the cantilever. For studying the relation between the mass variation  $\Delta m$  and frequency shift  $\Delta f$ , commercial tipless cantilevers (Arrow TL1Au, NanoWorld) are used for experiments. The shape of the tipless cantilever is shown in Figure. 3.9(a). For verifying its mass sensitivity, a square mass-tuning hole is made on the free end of the cantilever. And its mass-tuning function is fulfilled by changing the size of the hole. Because the magnitude of the high order resonances is smaller on the thermal fluctuation spectrum, a resonance-enhanced micromechanical cantilever (REM-cantilever) is designed for enhancing the second flexural mode. The geometrical design of the REM-cantilever is illustrated in Figure 3.9(b), and its corresponding dimensions are listed in Table 3.5. At the node of the second flexural mode, there are two seams created for enhancing the

resonance. Through this designed geometric shape, the REM-cantilever can effectively enhance the second flexural mode as shown in Figure 3.9(c). The detective laser spot is focused on the region between the square hole and two seams in experiments.

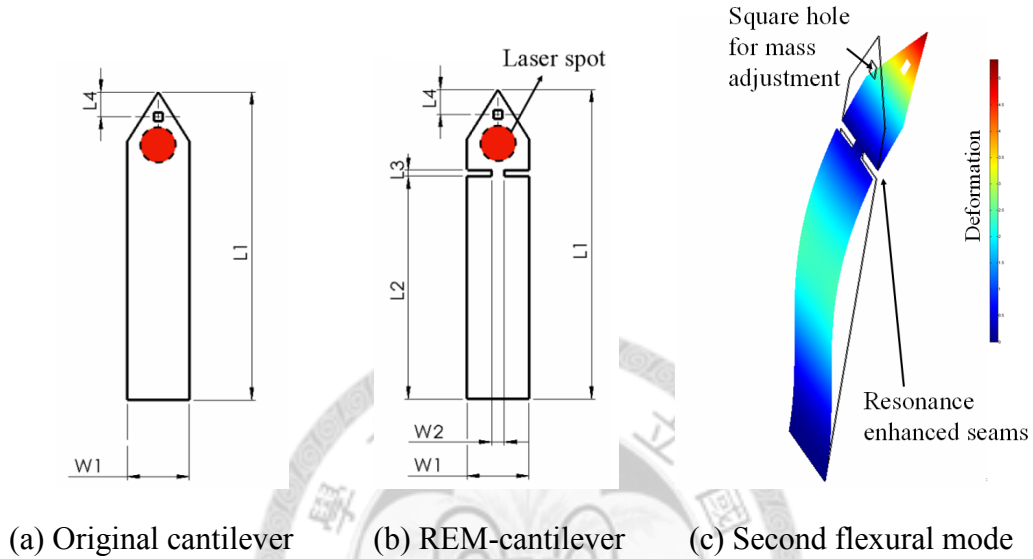


Figure 3.9 Cantilever dimensions

Table 3.5 Dimensions of REM-cantilevers

Symbol	Description	Value
$L1$	Total length	500 $\mu\text{m}$
$L2$	Distance from the end to the seam	360 $\mu\text{m}$
$L3$	Width of the seam	10 $\mu\text{m}$
$L4$	Distance from the tip to the center of the hole	40 $\mu\text{m}$
$W1$	Total width	100 $\mu\text{m}$
$W2$	Distance between the two seams	20 $\mu\text{m}$
$h$	Thickness	1 $\mu\text{m}$

For comprehending the frequency variation of the developed REM-cantilever, the finite element analytical (FEA) software FEMLAB is used. For deriving actual

eigen-frequencies of the cantilever, the fixed end surface must be constrained in all directions. The original micromechanical cantilever without mass-tuning hole has the first and second flexural resonant frequencies of 6.672 kHz and 44.714 kHz, respectively. The first and second flexural resonant frequencies of the REM-cantilever are 6.774 kHz and 43.239 kHz, respectively. Through modifying the side length of the square hole from 0 to 20.2  $\mu\text{m}$ , a mass variation ranged from 0 pg to -950 pg is achieved. The resonant frequency shifts with the mass variation of the original cantilever and the REM-cantilever are shown in Figures 3.10(a) and 3.10(b). The mass sensitivity is calculated by the first order polynomial curve fitting, and can be defined by the frequency shift  $\Delta f$  per unit mass variation  $\Delta m$ . Their mass sensitivities of the first and second flexural modes of the original cantilever are -0.1346 Hz/pg and -1.226 Hz/pg, respectively. The second flexural mode possesses a mass sensitivity 9.1 times higher than that of the first flexural mode. Similarly, the mass sensitivities of the first and second flexural modes of the REM-cantilever are -0.1502 Hz/pg and -1.4572 Hz/pg, respectively. The second flexural mode has also a mass sensitivity 9.7 times higher than that of the first flexural mode. For the original cantilever and the REM-cantilever, the second flexural mode has a higher mass sensitivity than that of the first flexural mode. The resonant frequency shift is near linear proportional to small mass variation. Nevertheless, the simulated second flexural resonant frequency has higher non-linear error than that of the first order one.

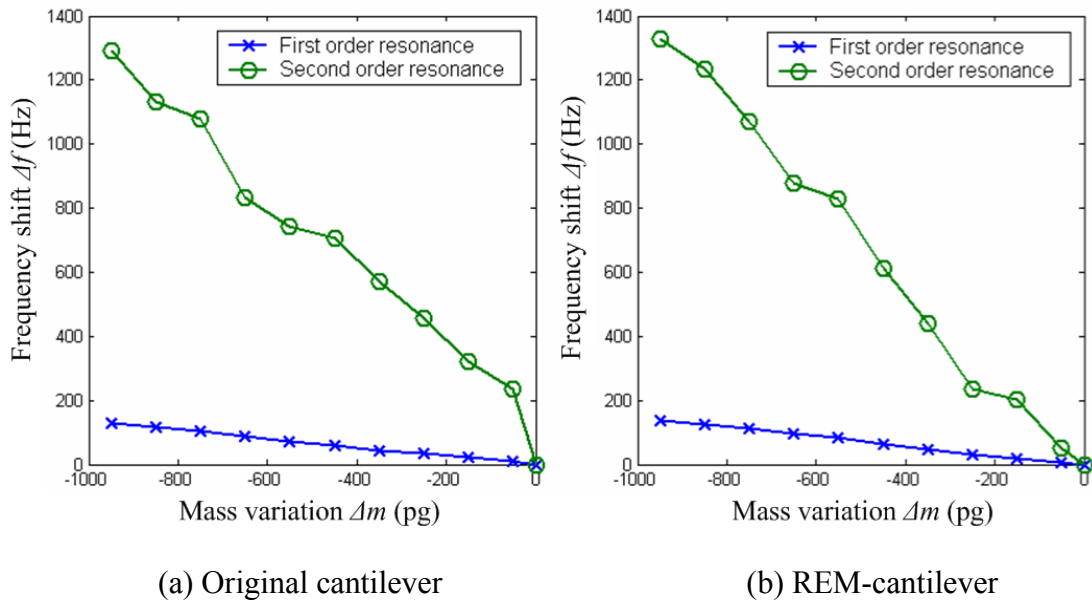


Figure 3.10 Resonant frequency shift  $\Delta f$  versus mass variation  $\Delta m$

In the experiment, an astigmatic detection system (ADS) based on an astigmatic pickup head (PUH) was utilized for detecting the micromechanical cantilever resonance. The experimental setup is shown in Figure 3.11. For monitoring the laser spot on the micromechanical cantilever, the ADS is integrated into the optical microscope (OM, Nikon Eclipse E100) through the adapter. The convex lens inside the adapter focuses the parallel light from the ADS and forms a real image to be observed by the 10X objective lens. Furthermore, the CCD camera is used to capture the image and transmit to the computer. Under this monitoring, the detected region of the cantilever can be aligned with the laser axis of the ADS by a XYZ stage. The signals from the PUH are first amplified and transformed into the focus error signal by the preamplifier, and the 14-bit high-speed digitizer (PCI-9820, ADLINK) with a sampling rate up to 130 MHz converts the focus error signal into the corresponding digital signal. The digital data are further transmitted into the computer and processed by the software (LabVIEW, National Instruments). The time domain signal is transformed into the frequency domain by

using the fast Fourier transform (FFT) algorithm, and the thermal fluctuation spectrum can be acquired.

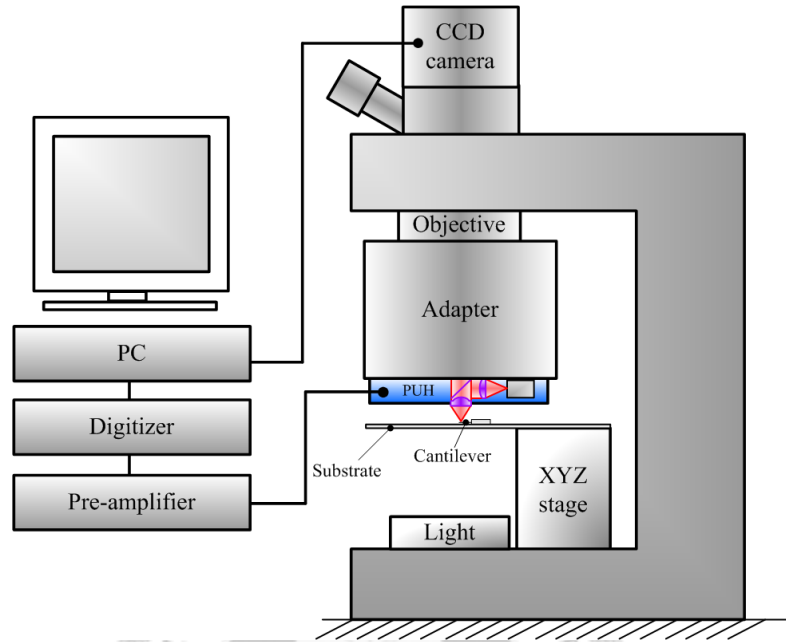
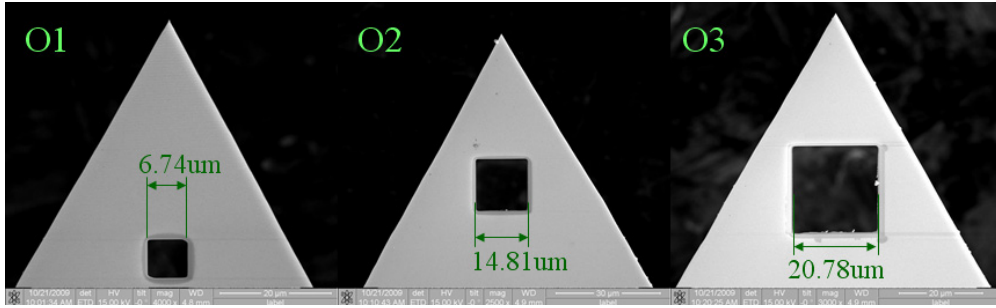
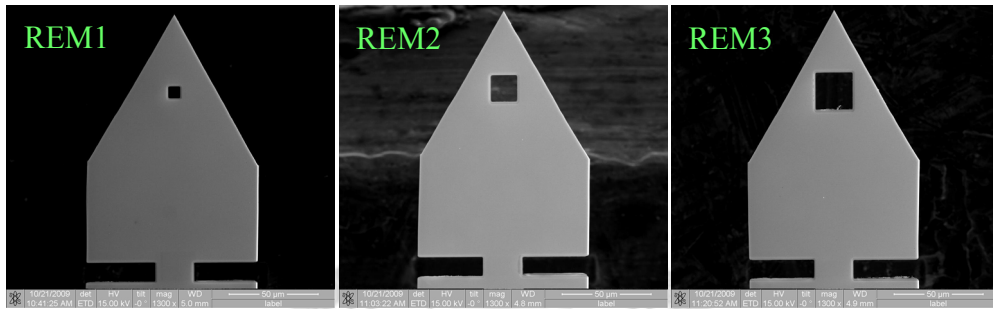


Figure 3.11 Configuration of experimental setup

For comparison, three original cantilevers O1, O2, and O3 are manufactured with different square mass-tuning holes, as shown in Figure 3.12(a), whose side lengths are  $6.74 \mu\text{m}$ ,  $14.81 \mu\text{m}$ , and  $20.78 \mu\text{m}$ , respectively. And their corresponding mass variations  $\Delta m$  are  $-105.8 \text{ pg}$ ,  $-511.1 \text{ pg}$ , and  $-1006.1 \text{ pg}$ , respectively. As evaluation counterparts, the mass variations on three REM-cantilevers REM1, REM2, and REM3 are  $-105.8 \text{ pg}$ ,  $-511.1 \text{ pg}$ , and  $-1006.1 \text{ pg}$ , respectively. Besides the square mass-tuning holes, two symmetric resonance-enhanced seams are simultaneously made on the REM-cantilevers as shown in Figure 3.12(b).



(a) Original-cantilevers with different mass variations



(b) REM-cantilevers with different mass variations

Figure 3.12 Modified cantilevers with mass variations

By setting the sampling rate of 5 MHz, the acquired thermal fluctuation spectrums of the original cantilevers are shown in Figure 3.13(a). The first flexural resonant peaks are distinct around 5 kHz, the second flexural resonant peaks can not be observed. For accurately identifying their resonant frequencies, the raw data of spectrums were processed by the curve-fitting method with nine order polynomial. The resonant frequency and the mass sensitivity of the  $n$ th flexural mode are denoted by  $f_{r,n}$  and  $S_n$ . The first flexural resonant frequencies  $f_{r,1}$  of O1, O2, and O3 are 5.378 kHz, 5.455 kHz, and 5.569 kHz, respectively. The sensitivity  $S_1$  of the resonant frequency to the mass variation is -0.21 Hz/pg. In comparison with the original cantilevers, Figure 3.13(b) shows the thermal fluctuation spectrums of the REM-cantilevers. Both the first and second flexural resonant peaks are distinctly observed. Their first flexural resonant frequencies  $f_{r,1}$  are 5.645 kHz, 5.722 kHz, and 5.798 kHz, and the sensitivity  $S_1$  of the

resonant frequency to the mass variation is  $-0.18 \text{ Hz/pg}$ . Their second flexural resonant frequencies  $f_{r,2}$  are  $31.853 \text{ kHz}$ ,  $32.387 \text{ kHz}$ , and  $32.578 \text{ kHz}$ , and the sensitivity  $S_2$  of the resonant frequency to the mass variation is  $-1.12 \text{ Hz/pg}$ . The second flexural mode has 6.2 times the mass sensitivity of the first flexural mode. The experimental results are listed in Table 3.6.

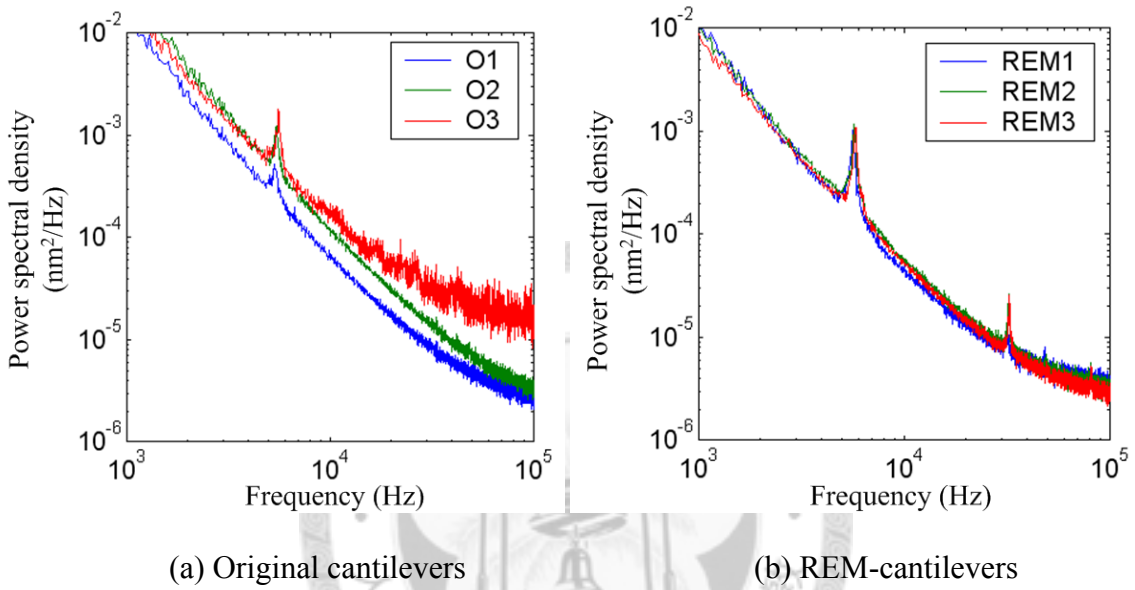


Figure 3.13 Thermal fluctuation spectrums

Table 3.6 Dynamic properties and mass sensitivity of modified cantilevers in air

Cantilever	First order resonant frequency $f_{r,1}$ (kHz)	Mass sensitivity on first order resonance $S_1$ (Hz/pg)	Second order resonant frequency $f_{r,2}$ (kHz)	Mass sensitivity on second order resonance $S_2$ (Hz/pg)	Mass variation $\Delta m$ (pg)
O1	5.378	-0.21	NA	NA	-105.8
O2	5.455		NA		-511.1
O3	5.569		NA		-1006.1
REM1	5.645	-0.18	31.853	-1.12	-103.7
REM2	5.722		32.387		-472.5
REM3	5.798		32.578		-1018.7

Both the simulation and the experiment verify that the second flexural mode can improve the mass sensitivity without reducing the cantilever dimensions, which are usually limited by the laser spot size of the optical detection system. Our developed REM-cantilevers have been approved to realize the resonance-enhanced function in the second flexural mode. The REM-cantilever is not only for the optical detection system but also adapted to other pickup systems such as capacitive and piezo-resistive sensors.

### 3.2.2 Mass sensitivity in water

For studying the higher order resonances in water, the mass-tuning cantilever O3 is compared with a cantilever without mass variation. For analyzing the dynamic performance of the cantilever, a FEA software (MULTIPHYSICS, COMSOL) is used to evaluate the influence on the variation of the resonant frequency. For creating a water environment, a 800  $\mu\text{m}$ -diameter water sphere is set around the cantilever. The resonant frequency shifts of five flexural modes are listed in Table 3.7. The  $n$ th flexural resonant frequency of the cantilever without mass variation in water is denoted by  $f_{liq,o,n}$ , and  $f_{liq,m,n}$  represents the resonant frequency of the mass-tuning cantilever. The fifth flexural mode has a frequency shift of 4176 Hz, which is about 77 times the frequency shift of the first flexural mode. The mass sensitivities of the fifth flexural mode and the first flexural mode are -4.48 Hz/pg and -0.058 Hz/pg, respectively.



Table 3.7 Simulated dynamic properties and mass sensitivity

Flexural mode $n$	Resonant frequency without mass-tuning $f_{liq,o,n}$ (kHz)	Resonant frequency with mass-tuning $f_{liq,m,n}$ (kHz)	Frequency shift $\Delta f_n$ (Hz)	Mass sensitivity $S_n$ (Hz/pg)
1	1.241	1.295	54	-0.058
2	8.324	8.689	365	-0.391
3	24.555	25.709	1154	-1.238
4	53.316	55.957	2641	-2.833
5	97.861	102.037	4176	-4.480

In the experiment, an AFM system (MFP-3D, Asylum Research) is utilized. The cantilever deflection signal is transformed by the 16 bits analog-to-digital converter (ADC) with 5 MHz sampling rate in the AFM controller. And the 131072 sampling data of the thermal fluctuation spectrum are processed by the fast Fourier transform (FFT). By using the simple harmonic oscillator (SHO) fitting curve, the resonant frequency and the Q-factor can be calculated from the derived spectrum data.

Figure 3.14(a) shows the spectra of flexural deflection signals with and without mass-tuning in air. The blue line represents the result of the unmodified cantilever, and the green line is the result of the modified cantilever with  $\Delta m$  of -1006 pg. The first four resonant peaks can be obviously distinguished in air. While the unmodified cantilever has resonant frequencies of 5.299 kHz, 32.088 kHz, 87.473 kHz, and 167.094 kHz; the modified cantilever possesses resonant frequencies of 5.564 kHz, 33.850 kHz, 92.510 kHz, and 176.289 kHz. Their average Q-factors are 25, 75, 133, and 198, and their frequency shifts are 265 Hz, 1762 Hz, 5037 Hz, and 9195 Hz. The mass sensitivities of the first flexural mode and the fourth flexural mode are -0.260 Hz/pg and -9.140 Hz/pg, and their difference reaches 35 times. Similarly, Figure 3.14(b) shows the spectra of flexural deflection signal in water. The resonant frequencies drop about 5 times those in air, and their Q-factors also decrease significantly. Even though, the fifth flexural mode

can be still recognized. Its mass sensitivity (-5.397 Hz/pg) is 94 times that of the first flexural mode (-0.057 Hz/pg), and its Q-factor (11) is about 5 times that of the first one (2). The experimental results are listed in Table 3.8.

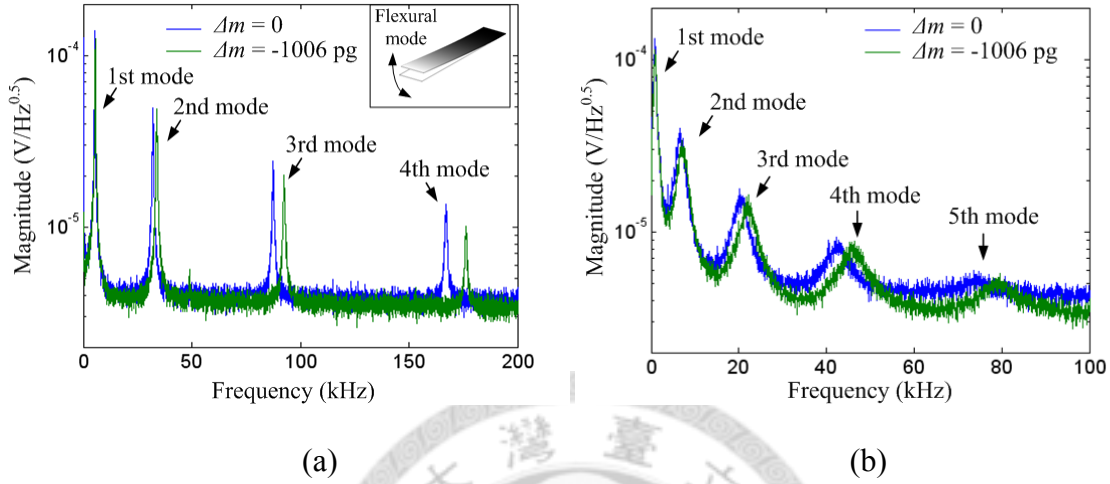


Figure 3.14 Thermal fluctuation spectra of  $n$ th flexural deflection with and without mass-tuning (a) in air and (b) in water

Table 3.8 Influence of resonant mode on dynamic properties and mass sensitivity

Flexural mode $n$	Resonant frequency without mass-tuning $f_{air,o,n}$ & $f_{liq,o,n}$ (kHz)	Resonant frequency with mass-tuning $f_{air,o,n}$ & $f_{liq,o,n}$ (kHz)	Average Q-factor	Mass sensitivity $S_n$ (Hz/pg)
In air				
1	5.299	5.564	25	-0.260
2	32.088	33.850	75	-1.751
3	87.473	92.510	133	-5.006
4	167.094	176.289	198	-9.140
torsion	47.414	48.890	89	-1.467
In water				
1	0.956	1.014	2	-0.057
2	6.561	7.074	3	-0.509
3	20.555	22.197	6	-1.632
4	42.605	46.351	8	-3.723
5	74.082	79.512	11	-5.397
torsion	13.233	13.882	3	-0.645

The mass sensitivities from the FEA-simulation and the experiment are compared in Figure 3.15. The evaluated mass sensitivity  $-0.058$  Hz/pg of the first flexural mode is very close to the experimental result  $-0.057$  Hz/pg, but the evaluated sensitivity  $-4.480$  Hz/pg of the fifth flexural mode has 17% deviation to the experimental result  $-5.397$  Hz/pg.

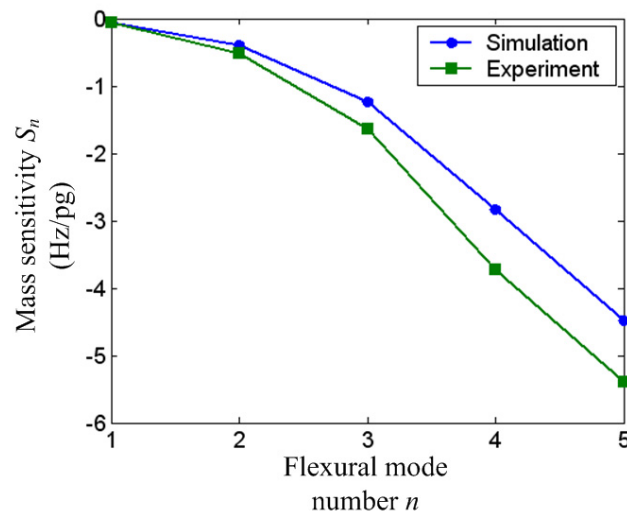


Figure 3.15 Experimental and simulated mass sensitivity of five flexural modes in water

Figure 3.16 shows the thermal fluctuation spectra of the torsional deflection signal with and without mass variation in air and water. The mass sensitivity reduced from  $-1.467$  Hz/pg to  $-0.645$  Hz/pg, the sensitivity decrease is about 56%. The mass sensitivity decrements of the first four flexural modes are 78%, 71%, 67%, and 59% respectively. In comparison with the flexural modes in water, the torsion mode has less sensitivity reduction, but its Q-factor has no obvious increment.

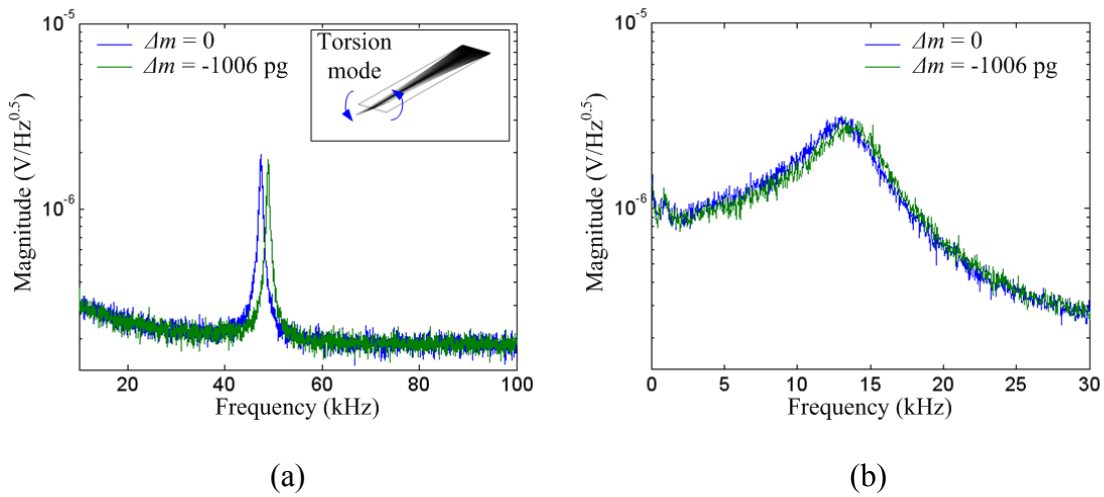


Figure 3.16 Thermal fluctuation spectra of torsional deflection signal with and without mass-tuning (a) in air and (b) in water

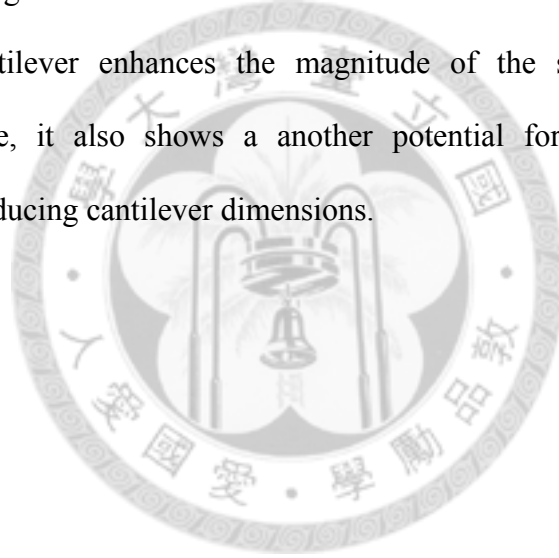
### 3.3 Conclusion

Utilizing the Sader's calculation method, the cantilever properties versus the cantilever length, width, and thickness are presented. The results show that the resonant frequency, the Q-factor, and the spring constant can't be improved simultaneously by modifying any single dimension of the cantilever directly. Through keeping the length to thickness ratio and the width constants, the spring constant can be maintained. The resonant frequency and the Q-factor can be raised through decreasing the cantilever thickness and the length proportionally. In the experiment, the width and the length of the cantilever are modified. The experimental results correspond to the calculation. However, the laser energy on the PSD reduces when the width becomes smaller, because the laser can't be reflected by the cantilever completely anymore. This phenomenon is obvious in water especially due to the focal length change and the laser divergence. Therefore, the laser spot size restricts the cantilever dimensions.

To overcome this limitation, another approach of making holes on the cantilever is

tested. However, comparing with the width and length variation, the holes have insignificant affection to the cantilever in water.

The resonant frequencies of high order resonances are higher than that of the fundamental resonance. Through simulated and experimental verification, we have approved that the high-order resonances can provide higher mass sensitivity in both air and water. The first five flexural modes in water can be acquired in the experiment. The mass sensitivity of the fifth flexural mode is 94 times that of the first flexural mode in water, and its Q-factor is also 5 times that of the first one mode. Although the signal to noise ratios of the high order resonances are smaller than the fundamental one. The developed REM-cantilever enhances the magnitude of the second flexural mode effectively. Therefore, it also shows a another potential for increasing the force sensitivity without reducing cantilever dimensions.



## Chapter 4

### Excitation Source and Transmission

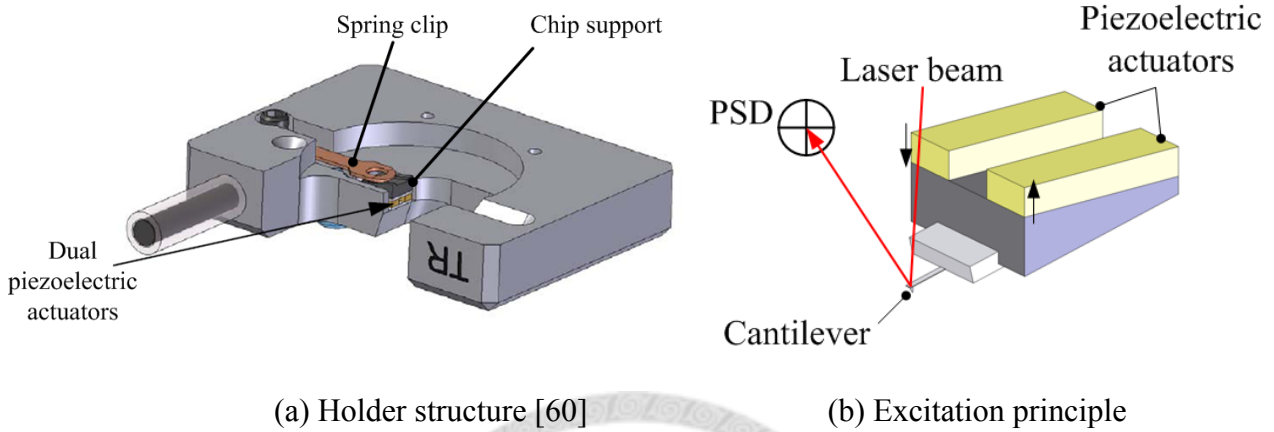
The piezoelectric actuator can provide precise and stable displacement, and is easy to control by a voltage signal. Therefore, the piezoelectric actuator is used for the excitation source in the AFM commonly. However, a complex excitation spectrum of the cantilever usually occurs in water. To overcome the problem, different cantilever holders are developed and tested. Besides, the both flexural excitation and torsional excitation are also examined.

#### 4.1 Cantilever Holder Design

##### 4.1.1 Modified commercial holder

The experiments are based on a commercial AFM (MultiMode, Bruker), which provides a cantilever holder for the TR-AFM [60]. Figure 4.1(a) shows the structure of the TR-mode holder. For installing the cantilever tip, the cantilever chip is placed on the chip support, and clamped by a spring chip. After cantilever installation, the holder is inverted, and inserted into the optical beam deflection system. Figure 4.1(b) illustrates the excitation principle. The two piezoelectric actuators can be driven by either the flexural excitation or the torsional excitation. The flexural excitation drives two actuators simultaneously, and is used for enhancing the cantilever flexural mode. On the other hand, the torsional excitation drives two actuators with 180 degree phase lag for the TM-AFM. The cantilever flexural and torsional dynamics can be detected by the vertical displacement and the lateral displacement of the laser spot on the PSD, and are denoted by the flexural signal and the lateral signal, respectively. However, the

commercial TR-mode holder is not designed for liquid environment. Therefore, a glass slice is glued between the incident laser and the cantilever. Then a liquid drop can be contained between the glass slice and the substrate, and surrounds the cantilever.



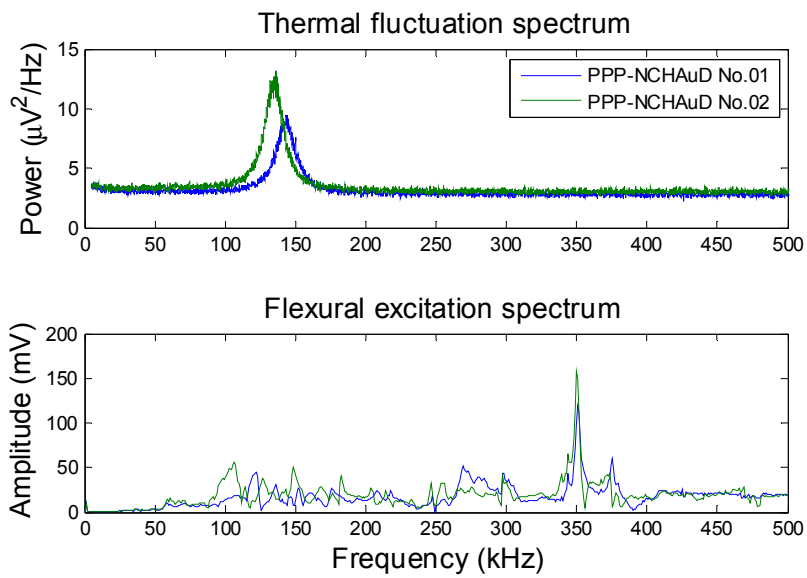
(c) Modified TR-holder pictures  
 Figure 4.1 Commercial TR-mode holder

For testing the excitation performance of the holder, two types of cantilevers are utilized. The cantilever PPP-NCHAuD (NANOSENSORS) is a typical cantilever for the tapping mode. It has a length of 125  $\mu\text{m}$ , a width of 30  $\mu\text{m}$ , and a thickness of 4  $\mu\text{m}$ . The cantilever CSC38-B (CSC38-lever B, MikroMasch) has a length of 350  $\mu\text{m}$ , a width of 35  $\mu\text{m}$ , and a thickness of 1  $\mu\text{m}$ , and is used for the contact mode generally. Both types of the cantilevers have Au coating for enhancing the reflectivity. For each type, two cantilevers are measured for examining the repeatability. For avoiding the pollution

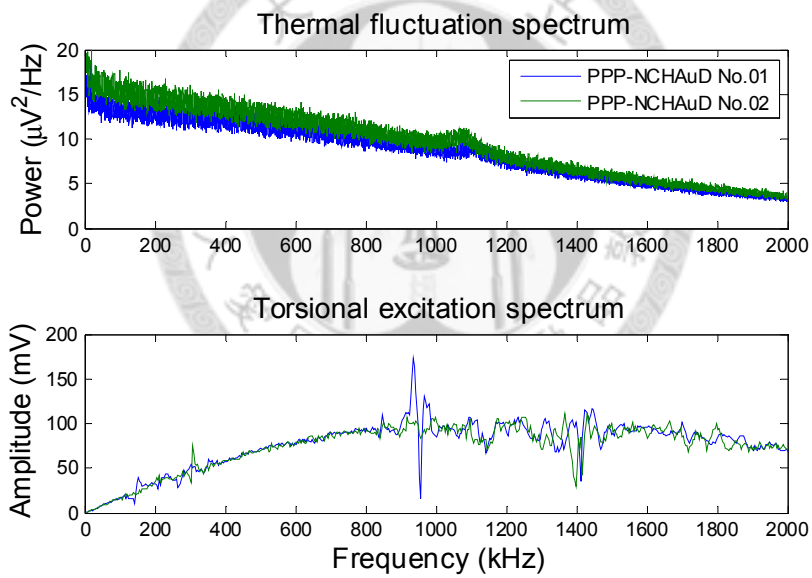
from the substrate, a cleaved graphite sample is used, and the distance between the sample and the cantilever is about 1 ~ 2 mm. The de-ionized water (DI water) of 50 ~ 100  $\mu\text{l}$  is dropped by a pipe. The thermal fluctuation spectrum is measured for identifying the cantilever resonant peaks first. The spectrums of the flexural and torsional excitation are captured through a lock-in amplifier in the AFM controller.

Figure 4.2(a) shows the thermal fluctuation spectrums and the flexural excitation spectrums of the flexural signal in water. The results of two PPP-NCHAuD cantilevers named PPP-NCHAuD No.01 and No.02 are represented by the blue and green lines. From the thermal fluctuation spectrums, their resonant frequencies of the first flexural mode are 143.8 kHz and 135.4 kHz, and the Q-factors are 8.9 and 8.7. In the flexural excitation spectrums, the amplitude of the driving signal is set to 1 V for excitation in water. An unknown peak around 350 kHz appears on both cantilevers, and no obvious peak can be observed around the real resonant peaks. The thermal fluctuation spectrums and the torsional excitation spectrums of the lateral signal are shown in Figure 4.2(b). The torsional resonant frequencies of PPP-NCHAuD No.01 and No.02 are 1110 kHz and 1070 kHz in the thermal fluctuation spectrums. In the torsional excitation spectrum, only one peak appears at 935 kHz on PPP-NCHAuD No.01.





(a) Flexural signal

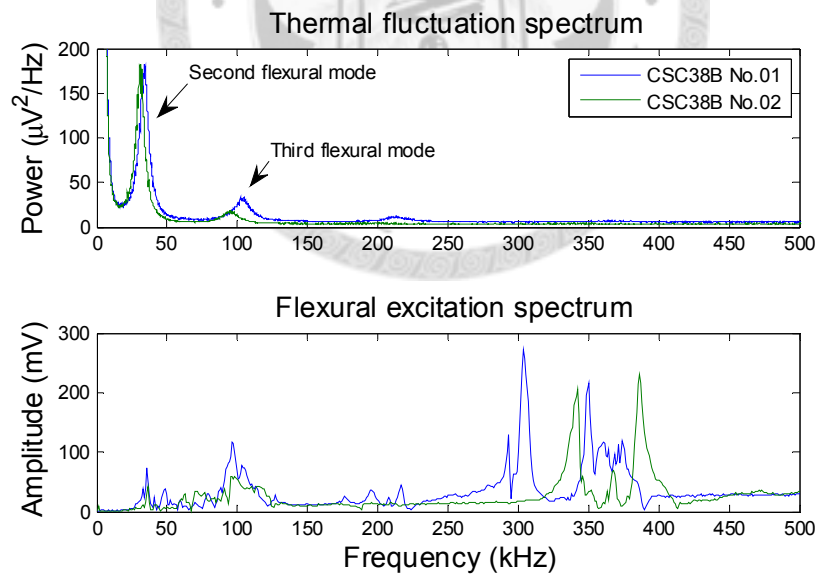


(b) Lateral signal

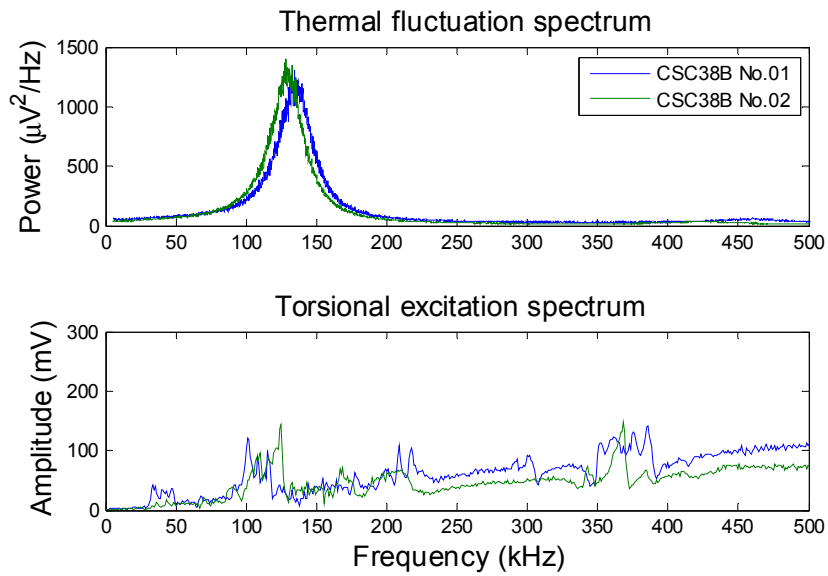
Figure 4.2 Spectrums of cantilever PPP-NCHAuD

Similarly, Figure 4.3(a) shows the thermal fluctuation spectrums and the flexural excitation spectrums of the CSC38B cantilevers. According to the thermal fluctuation spectrums, the first flexural resonant frequencies of CSC38B No.01 and No.02 are 4.2

kHz and 4.0 kHz. Because the frequency range in Figure 4.3(a) is adjusted for displaying the second and third resonant peaks, the first resonant peak can't be completely seen in the thermal fluctuation spectrum. Their second flexural resonant frequencies are 33.6 kHz and 31.0 kHz, and the third flexural resonant frequencies are 103 kHz and 95 kHz respectively. In the flexural excitation spectrum, the first resonant peak can't be excited, but the second resonant peaks around 35 kHz and third resonant peaks around 100 kHz are excited. Besides, large peaks appear between 300 ~ 400 kHz. In Figure 4.3(b), the torsional resonant frequencies of CSC38B No.01 and No.02 are 137.0 kHz and 131.2 kHz, and the Q-factors are 4.5 and 4.6 in the thermal fluctuation spectrums. In the torsional excitation spectrum, peaks still appear around 100 kHz and 350 kHz.



(a) Flexural signal



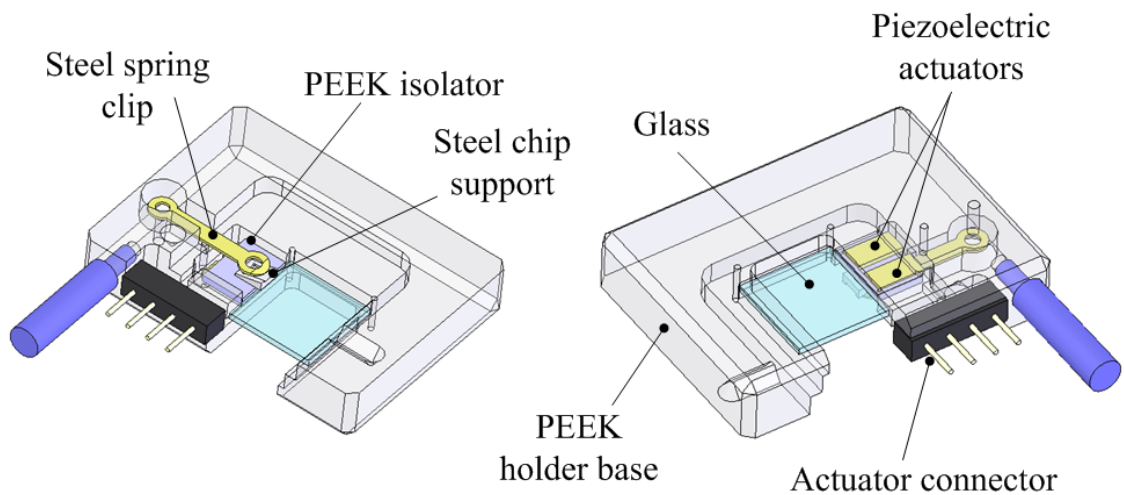
(b) Lateral signal

Figure 4.3 Spectrums of cantilever CSC38B

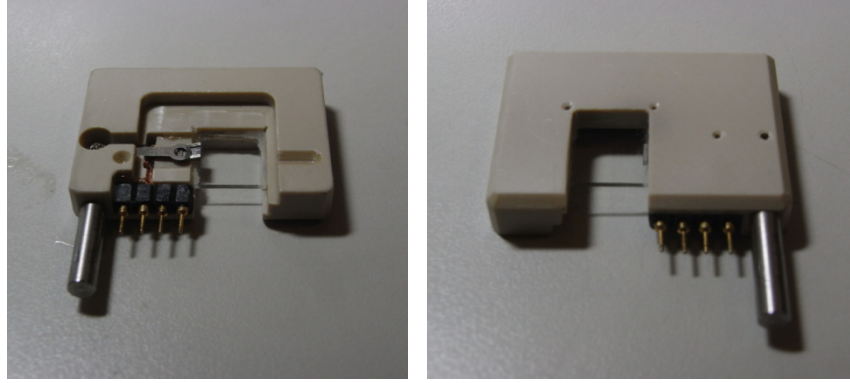
Summarizing the results on both types of cantilever, spurious peaks around 350 kHz always exist. Because no resonant mode can be observed around 350 kHz in the thermal fluctuation spectrums, these spurious peaks may be associated with the holder structure. On the PPP-NCHAuD cantilevers, no obvious peak can be recognized in both flexural and torsional excitation spectrums. On the CSC38B cantilevers, the second and third flexural modes can be excited. In the torsional excitation spectrum, although the peaks occur around the torsional resonant frequencies, peaks also appear in the flexural excitation spectrums with similar amplitudes. Therefore, these peaks are still difficult for classification.

### 4.1.2 Material modification

For getting the pure excitation spectrum in water, the material modification proposed by Asakawa and Fukuma is utilized [47]. The propagation of the acoustic wave is suppressed by the combination between steel and polyether ether ketone (PEEK) materials. However, their flexure hinge design is not applicable for the torsional excitation. Therefore, a PEEK-based cantilever is designed here for both the flexural and torsional excitation as shown in Figure 4.4(a). The dual piezoelectric actuators are glued between a PEEK holder base and a PEEK isolator, and the chip support and the spring chip are steel. Therefore, the acoustic wave must be transmitted to the cantilever through the PEEK-steel interface. A four pins actuator connector is connected with the piezoelectric actuators, and provides arbitrary driving interface on each actuator. A glass with the anti-reflective coating is also assembled for operation in liquid.



(a) Holder structure

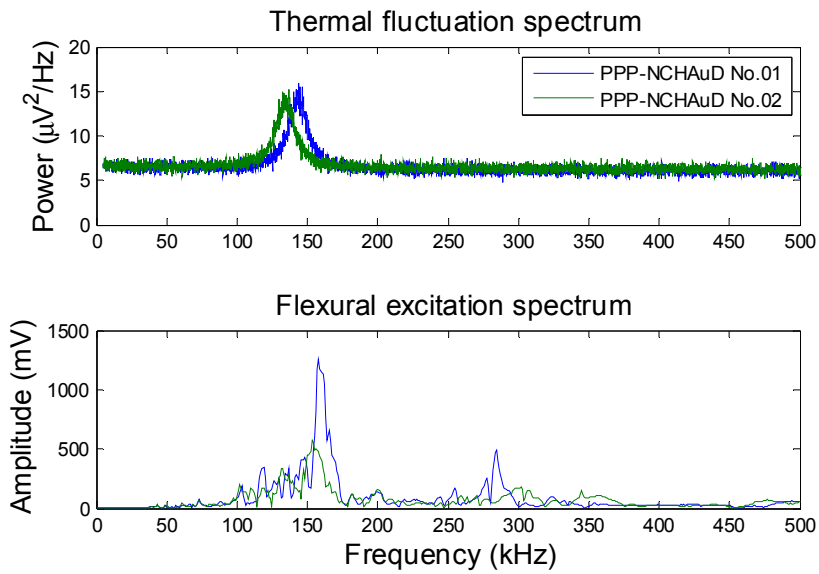


(b) Holder pictures

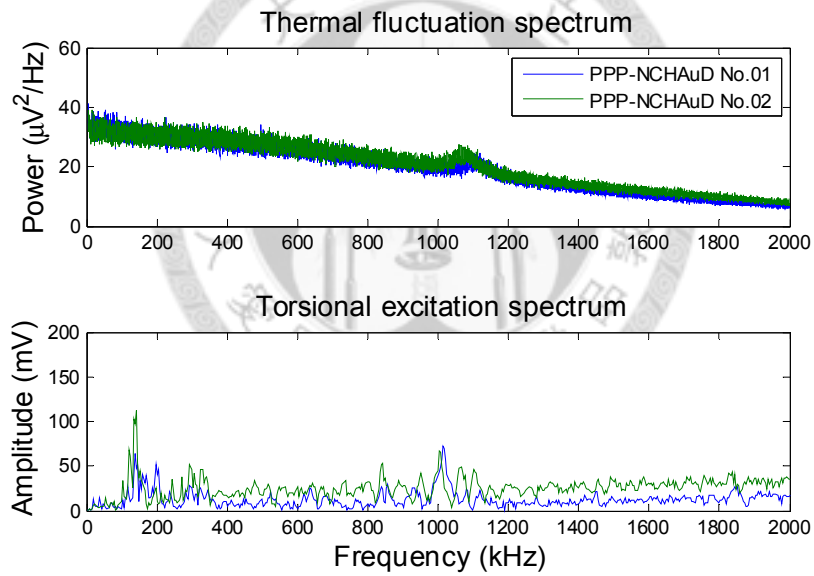
Figure 4.4 PEEK-based holder

In the experiments, the same cantilevers of PPP-NCHAuD and CSC38B are tested. The driving signal is connected to actuator connector from the signal access module of the AFM controller. The flexural excitation and the torsional excitation can be switched through changing the wiring directly.

Figure 4.5(a) shows the results of the flexural signal spectrums of the PPP-NCHAuD cantilevers. The resonant frequencies on the thermal fluctuation spectrums are same with the results on the modified commercial TR-holder. The flexural excitation spectrum is also captured with the excitation amplitude of 1 V. The first flexural resonant peaks of the two cantilevers can be excited. Although a peak still appears around 300 kHz on PPP-NCHAuD No.01, but its amplitude is smaller than the first flexural peak. On the other hand, the results of the lateral signal are shown in Figure 4.5(b). Small peaks occur at about 140 kHz and 1010 kHz, which are close to the first flexural and the torsional resonant frequencies respectively.



(a) Flexural signal

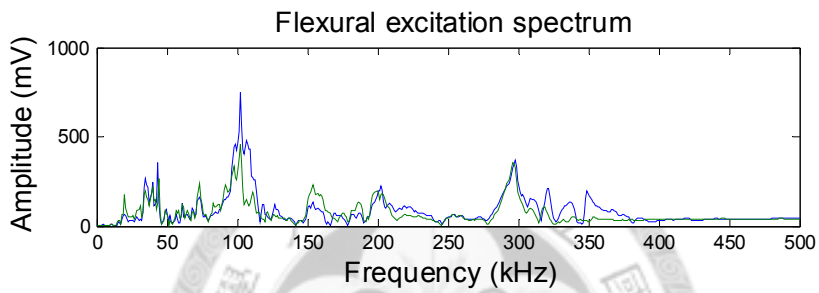
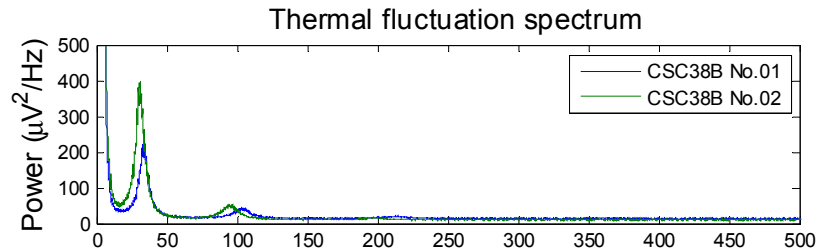


(b) Lateral signal

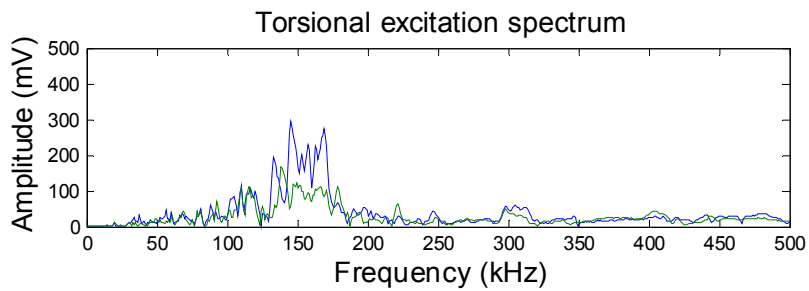
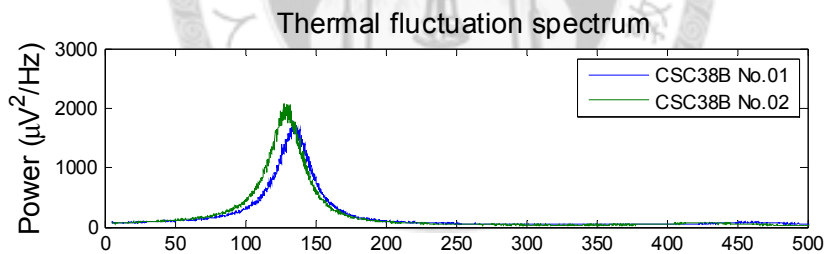
Figure 4.5 Spectrums of cantilever PPP-NCHAuD

The flexural and torsional excitation spectrums of the cantilevers CSC38B are shown in Figure 4.6(a) and 4.6(b), respectively. Besides the first and second resonant peaks, peaks still appear around 300 kHz in the flexural excitation spectrum. In the

torsional excitation spectrum, the torsional amplitude is larger around 150 kHz, and the other frequency range is quiet. However, the peaks are broad and noisy.



(a) Flexural signal



(b) Lateral signal

Figure 4.6 Spectrums of cantilever CSC38B

Comparing with the modified commercial TR-mode holder, the PEEK-based

holder induces less spurious peaks. Besides, the flexural resonant peak of PPP-NCHAuD and the torsional resonant peak of CSC38B can be excited.

For comparing the effect of the material, a steel-based holder is made as shown in Figure 4.7. The geometric design is same with the PEEK-based holder, but the PEEK parts are replaced by steel material. Besides, the piezoelectric actuators are isolated by two slices of glass.

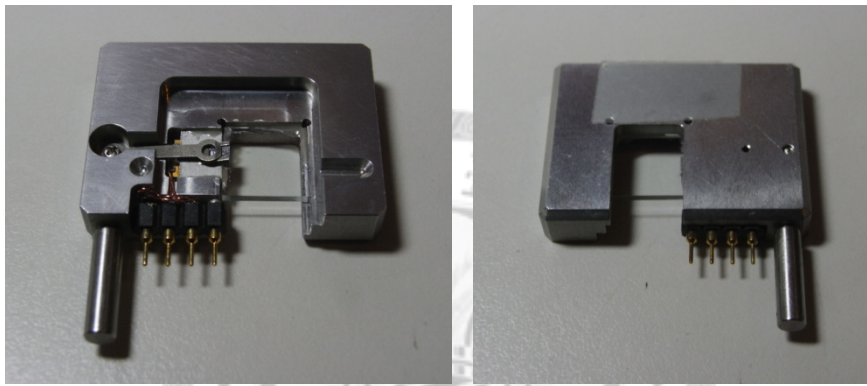
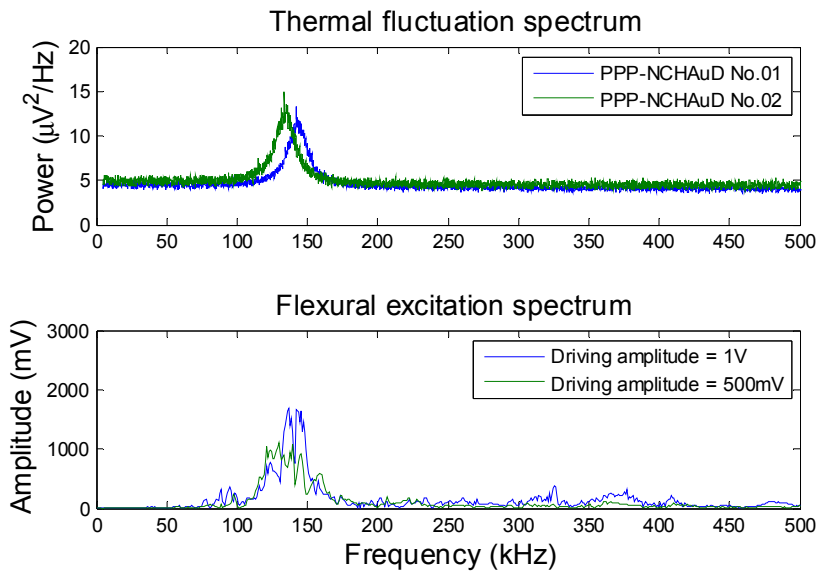


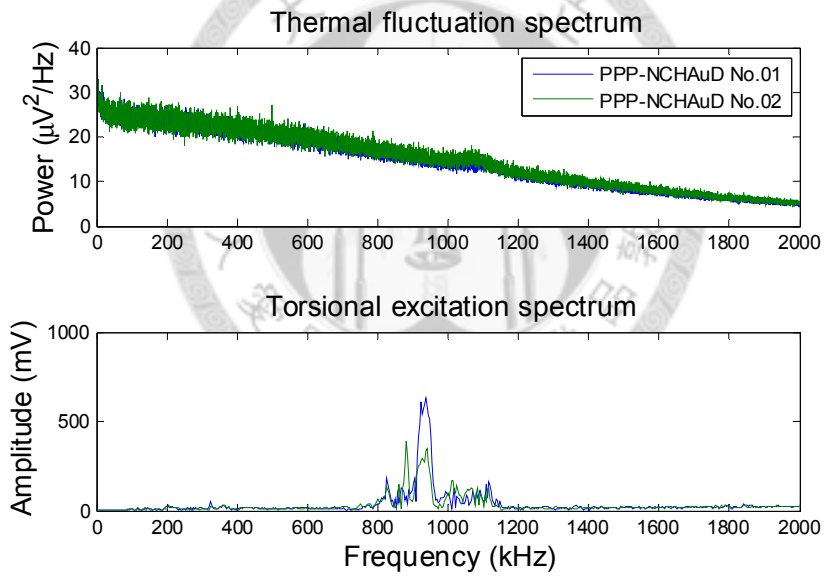
Figure 4.7 Steel-based holder

Figure 4.8(a) shows the results of the flexural signal spectrums of the PPP-NCHAuD cantilevers. Especially, the driving amplitude for PPP-NCHAuD No.2 is only 500 mV, because the cantilever amplitude is too large and causes an overload in the spectrum when the driving amplitude is 1 V. In our experience, although the driving amplitude affects the amplitude of peaks, but the form of the spectrum is almost the same. The results show the first flexural resonant peak can be excited, and no obvious spurious peaks appear. In Figure 4.8(b), a peak at 930 kHz is excited by the torsional excitation. However, it is about 100 kHz less than the peak in thermal fluctuation spectrum.





(a) Flexural signal



(b) Lateral signal

Figure 4.8 Spectrums of cantilever PPP-NCHAuD

The spectrums of CSC38B are shown in Figure 4.9. In the flexural excitation spectrum, besides the first and second resonant peaks, many peaks exist between 100 ~ 400 kHz. In the torsional excitation spectrum, a lot of peaks appear between the 50 ~ 250 kHz, and the torsional resonant peak can't be recognized. Comparing the results on

PEEK-based holder and steel-based holder, the suppressant effect of spurious peaks is better on the PEEK-based holder with CSC38B cantilever. On the other hand, the steel-based holder produces larger amplitude under the same driving amplitude.

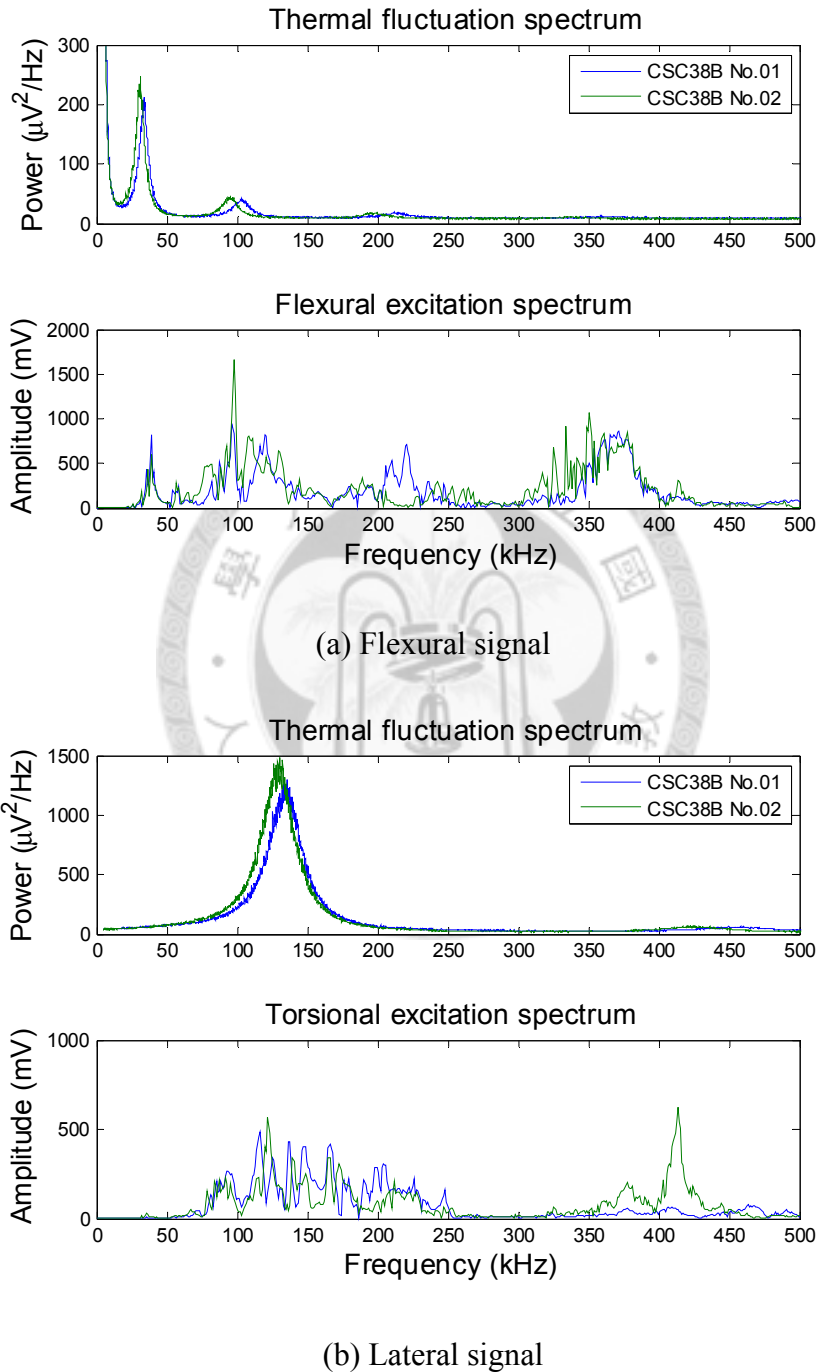
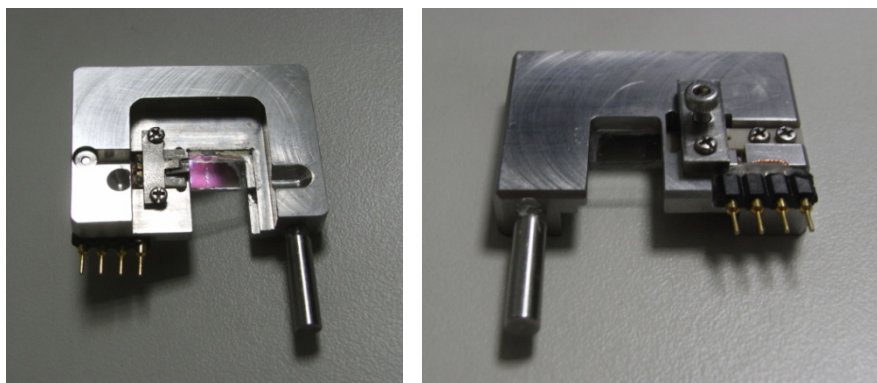
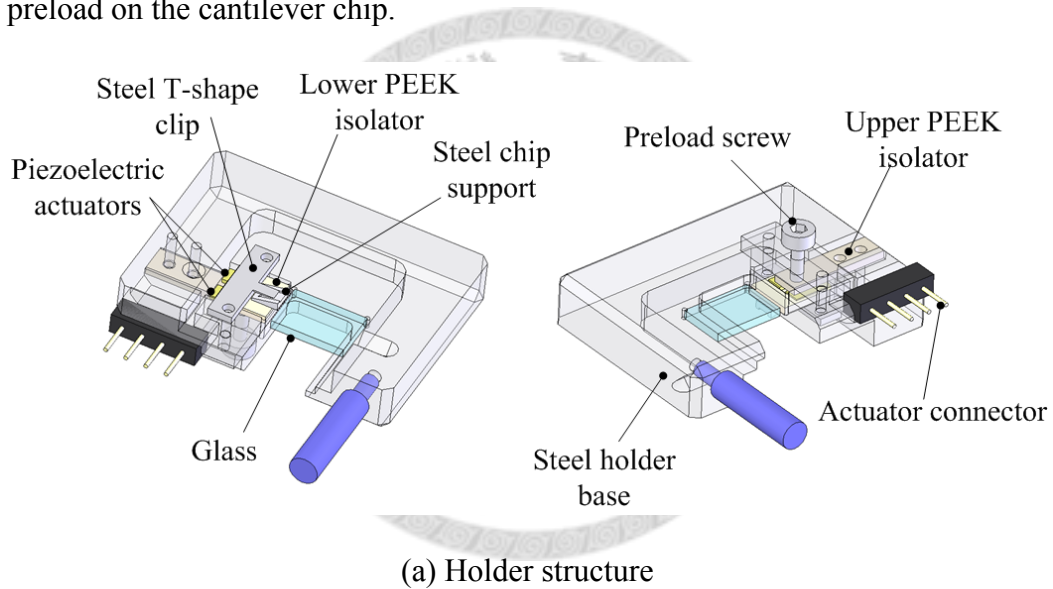


Figure 4.9 Spectrums of cantilever CSC38B

### 4.1.3 Preload adjustment

Besides the material issue, the preload on the cantilever chip is also considered. For adjusting the preload under the same condition, an adjustable preload holder is designed as shown in Figure 4.10. The dual piezoelectric actuators are placed between the upper and lower PEEK isolators, and the steel chip support is glued on the lower PEEK isolator. For providing larger preload, the original spring clip is replaced by a steel T-shape clip. The upper PEEK isolator is fixed on the steel holder base. For adjusting the preload, a screw is used to press the upper PEEK isolator, and increases the preload on the cantilever chip.



(b) Holder pictures

Figure 4.10 Adjustable preload holder

In the experiments, the driving signal amplitude is 500 mV. The preload is adjusted under the same condition, and the results are repeatable when the preload is tuned back. Figure 4.11(a) displays the variation of the flexural excitation spectrum of the cantilever PPP-NCHAuD. The preload is increased gradually, and is distinguished into six states, where the black square represents the magnitude of the preload. At state 1, the peak of first flexural mode is in the spurious peaks between 150 ~ 250 kHz. A pure peak can be obtained through increasing the preload to state 2. At state 3, a peak around 220 kHz appears. The amplitude of the first flexural resonant peak starts to decay at state 4, and disappears at state 5. From state 1 to state 4, the resonant frequency of the first mode reduces with the preload increasing, and approaches to the resonant frequency in the thermal fluctuation spectrum. In the lateral signal as shown in Figure 4.11(b), peaks appear between 600 kHz to 1200 kHz. Besides, the peak around 200 kHz also appears. The peak around 700 kHz has the maximum amplitude at state 3, and its resonant frequency also decreases following the preload increasing.

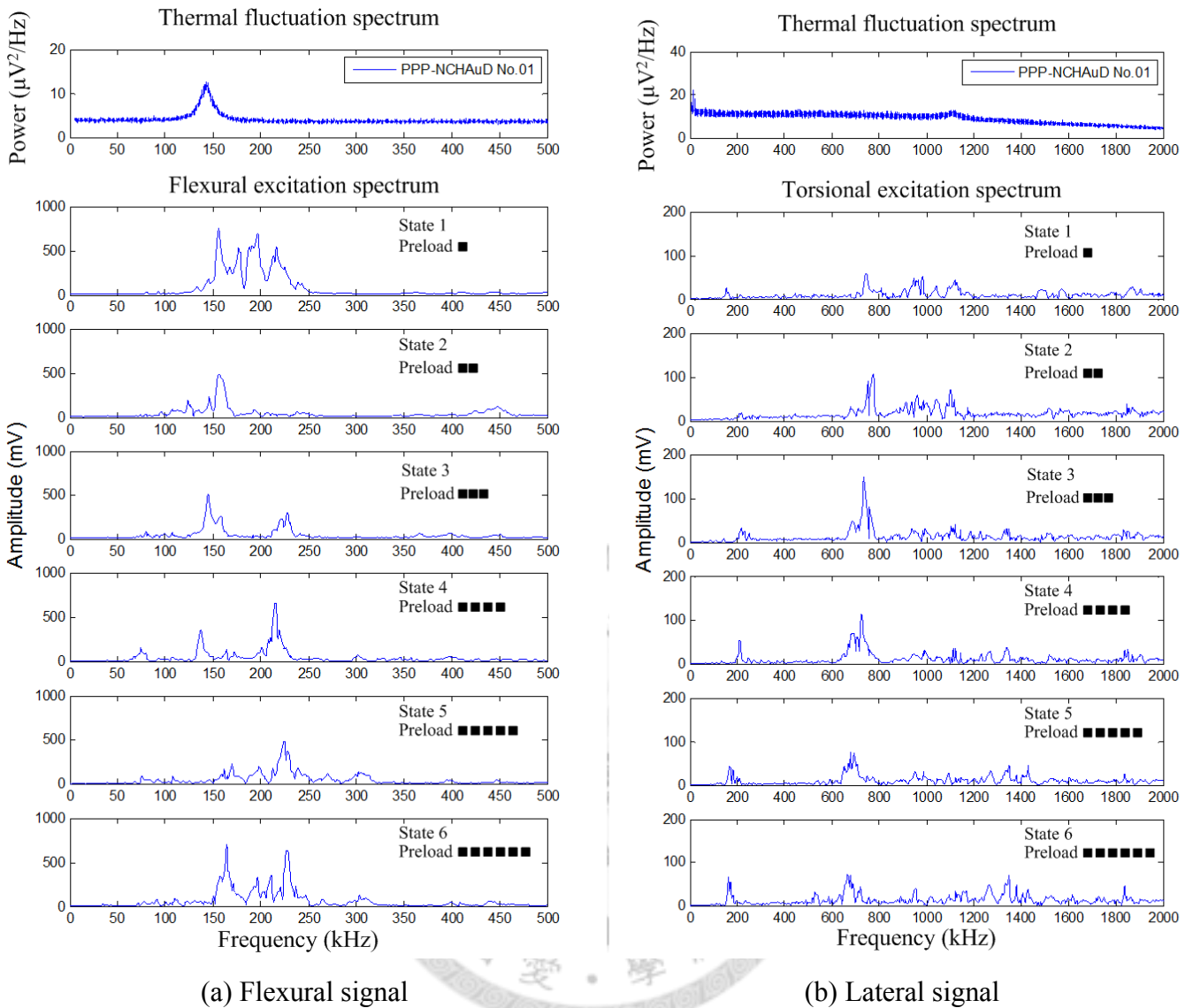
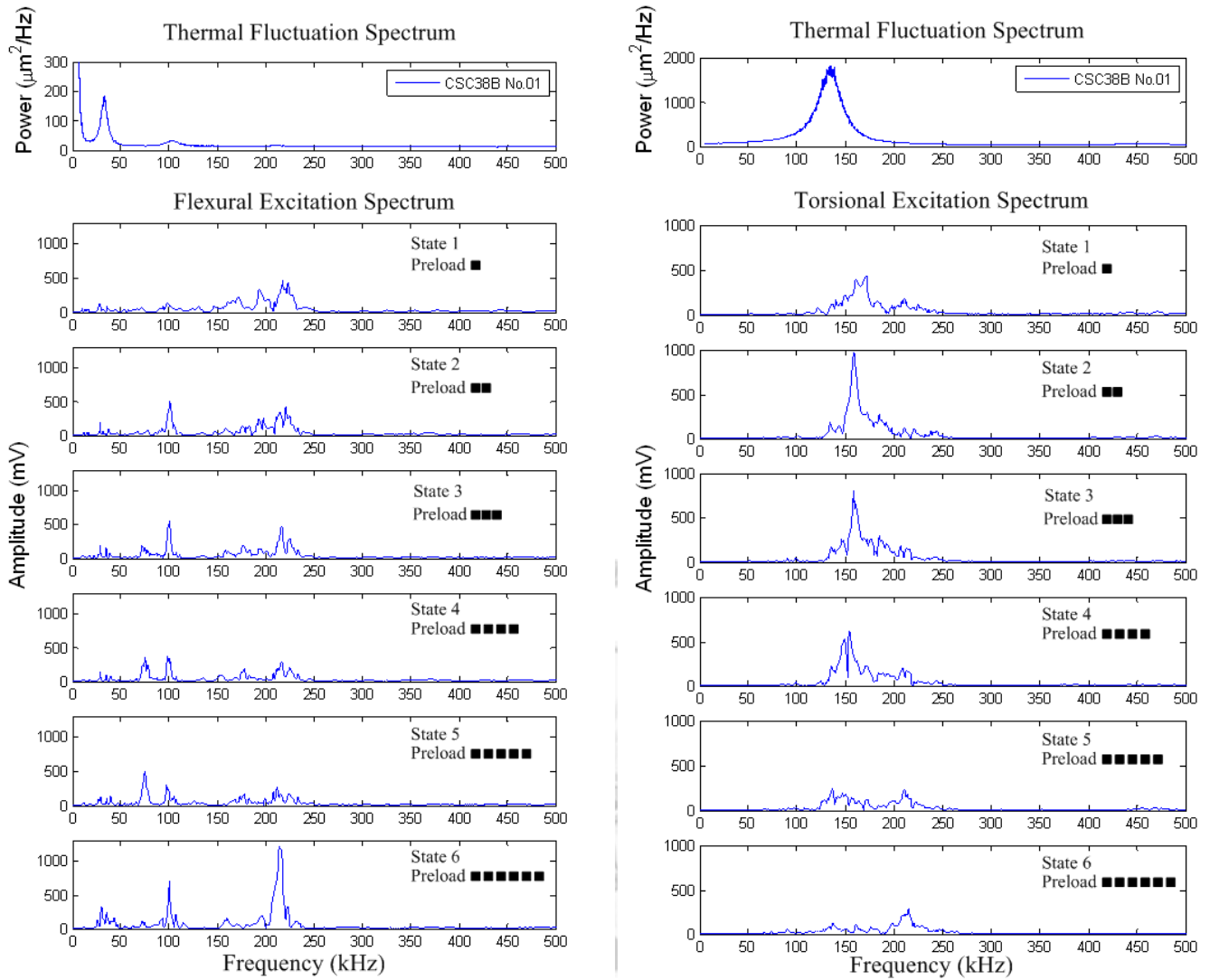


Figure 4.11 Spectrums of cantilever PPP-NCHAuD with different preload

The flexural spectrums of the cantilever CSC38B are shown in Figure 4.12(a). The third flexural resonant peak appears from state 2, and the peak around 200 kHz still exists. At state 6, the second flexural resonant peak becomes obvious. Besides, the third flexural resonant peak and the peak around 200 kHz also have maximum amplitudes. On the lateral signal as shown in Figure 4.12(b), a pure torsional peak can be obtained at state 2. When the preload is increased continuously, its amplitude and frequency reduce, and the peak disappears at state 5.



(a) Flexural signal

(b) Lateral signal

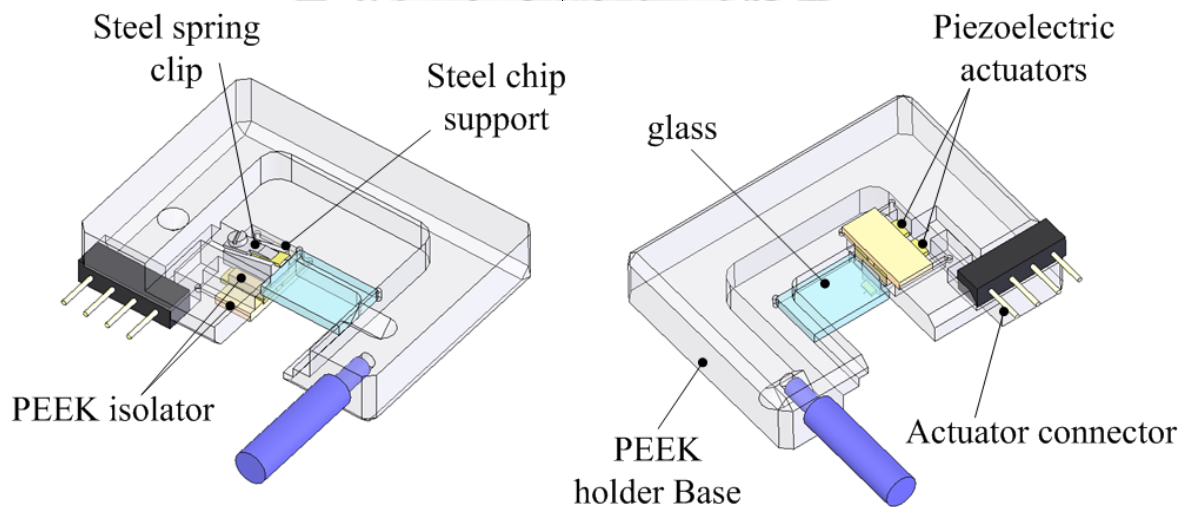
Figure 4.12 Spectrums of cantilever CSC38B with different preload

The peak around 200 kHz appears on both types of cantilevers. Therefore, it may be caused by the holder structure. The pure flexural resonant peak of PPP-NCHAuD can be obtained through adjusting the preload, but the torsional peak can't be excited. On the cantilever CSC38B, the second and third flexural modes can be excited, but the peak around 200 kHz can't be eliminated. The pure torsional peak can be also obtained through adjusting the preload. In this holder design, the preload not only changes the clamped force on the cantilever chip, but the preload on the piezoelectric actuators and

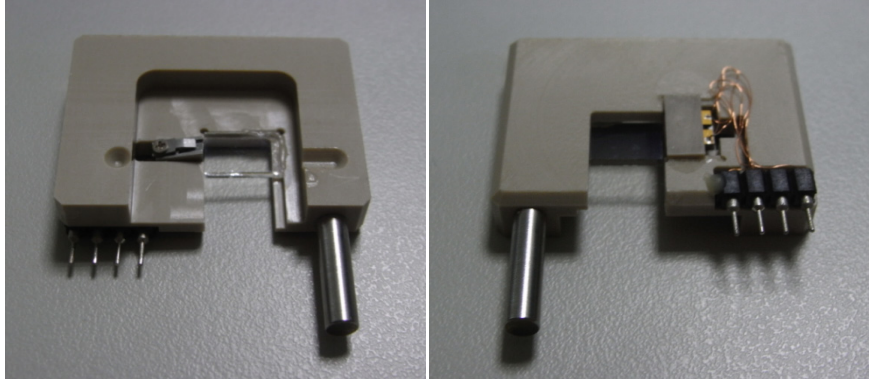
the holder structure. These coupling affections cause the principle of the preload adjustment indistinctly.

#### 4.1.4 Chip-clamped modification

The adjustable preload holder not only changes the preload on the cantilever chip, but also the preload on the piezoelectric actuators. Therefore, the cantilever clamp design could constrain the movement of the piezoelectric actuators. Besides, the steel T-shape clip connects the cantilever chip and the holder base, and the vibration can also transmit through it. Therefore, a clamp-modification holder is developed for decreasing the affection from the holder base. As shown in Figure 4.13, the steel spring chip is isolated to the holder base, and is screwed on the chip support directly.



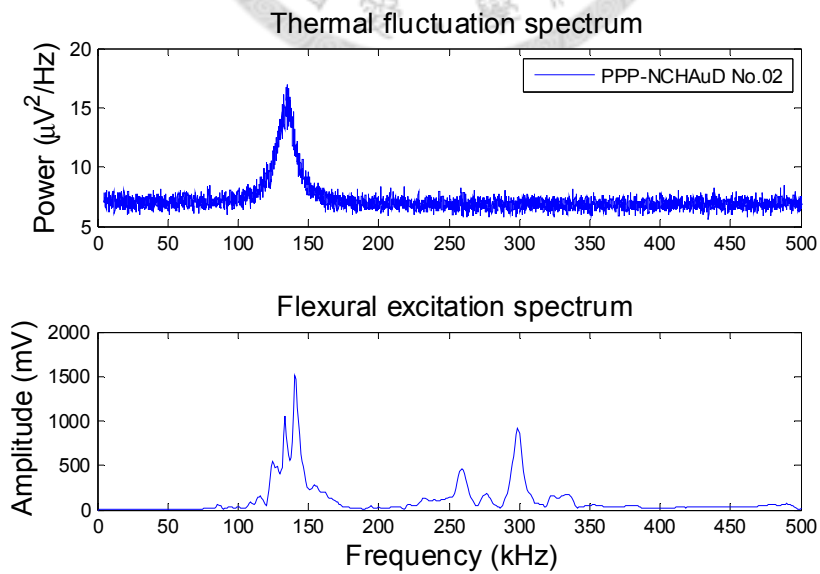
(a) Holder structure



(b) Holder pictures

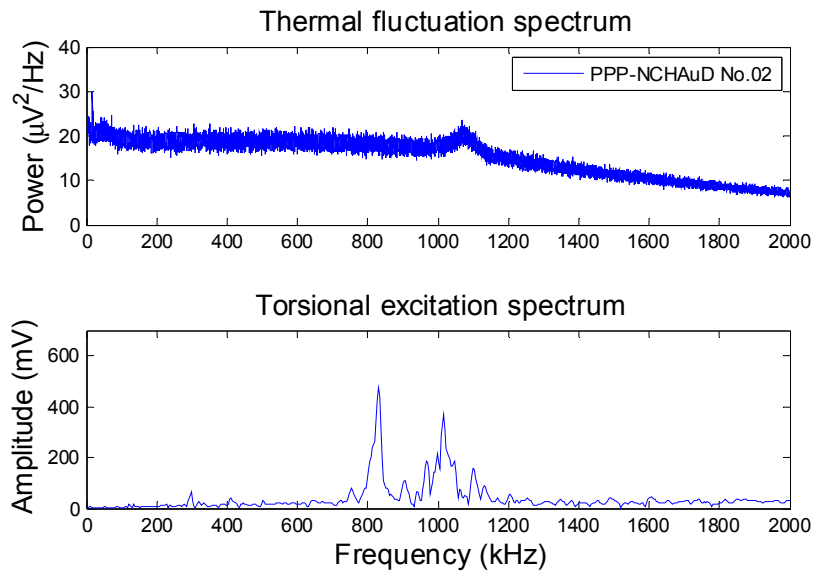
Figure 4.13 Clamp-modification holder

The driving amplitude is 1V, and Figure 4.14(a) shows the result of the flexural signal spectrum of the PPP-NCHAuD cantilever. Only the PPP-NCHAuD No.2 is shown, because the PPP-NCHAuD No.01 is broken accidentally during handling the cantilever. The result shows the first flexural resonant peak can be excited, but few peaks appear around 300 kHz. Figure 4.14(b) shows the lateral signal spectrum, and two peaks appear around 830 kHz and 1015 kHz.



(a) Flexural signal

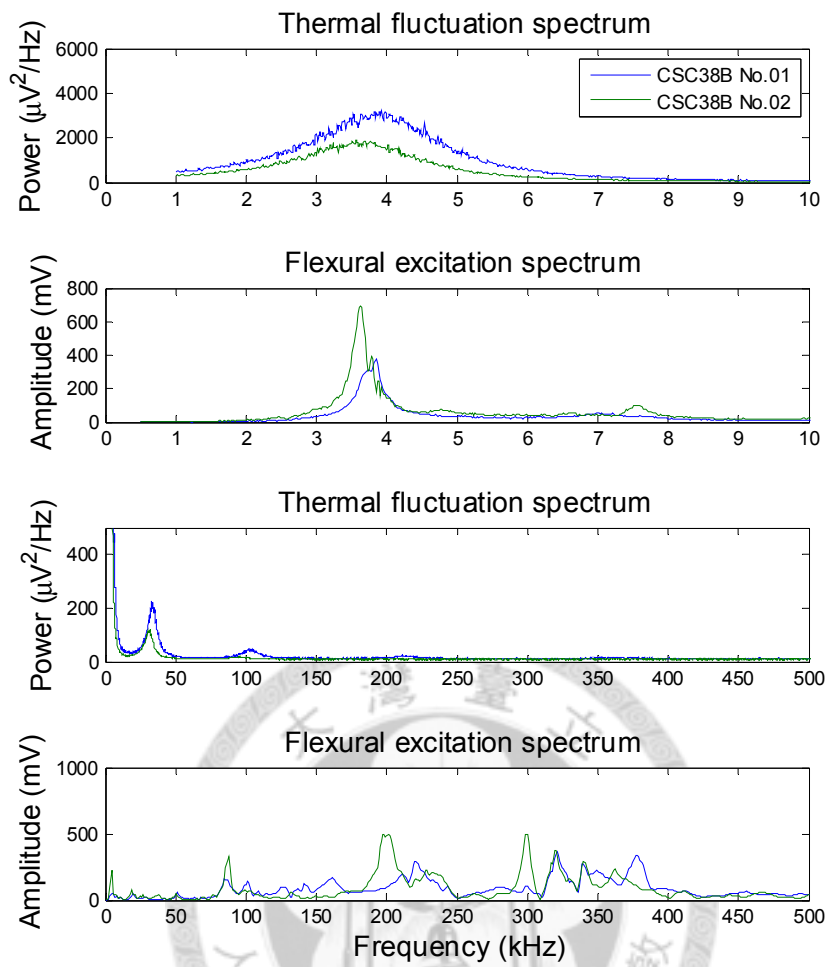




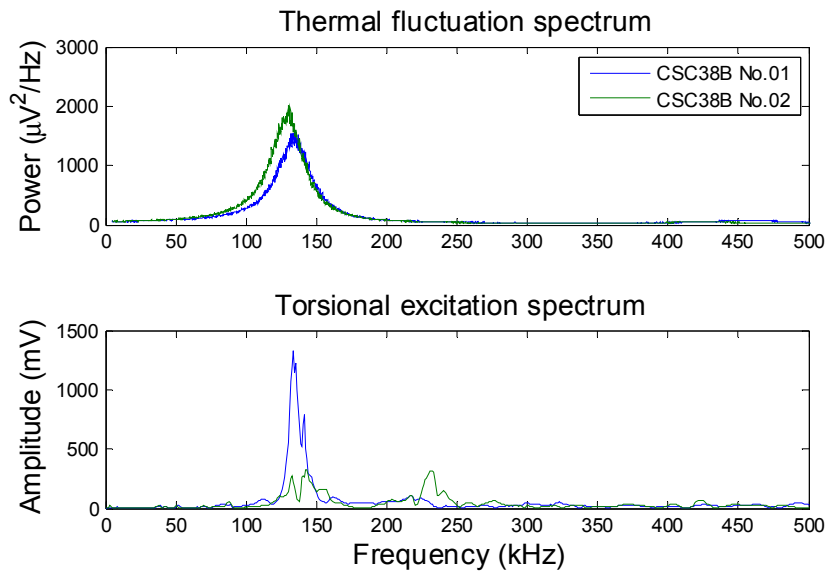
(b) Lateral signal

Figure 4.14 Spectrums of cantilever PPP-NCHAuD

The flexural signal spectrums of the CSC38B cantilevers with two different frequency ranges are shown in Figure 4.15(a). Unlike the experimental results of the previous holder, the first flexural resonant peak around 3~4 kHz can be excited clearly. However, the second flexural resonant peak can't be observed, and spurious peaks appear between 200 kHz and 400 kHz. Besides, the resonant peak in the excitation spectrum is sharper than that in the thermal fluctuation spectrum. The Q-factors of CSC38B No.01 and No.02 in the thermal fluctuation spectrums are 1.8 and 1.7. On the other hand, the Q-factors of the two cantilevers are 14.7 and 23.9 in the excitation spectrums. From the lateral signal spectrums shown in Figure 4.15(b), the torsional resonant peak can also be excited. No spurious peak is observed on the spectrum of the cantilever CSC38B No.01. However, the torsional resonant peak of the cantilever CSC38B No.02 is smaller, and a spurious peak appears around 230 kHz.



(a) Flexural signal



(b) Lateral signal

Figure 4.15 Spectrums of cantilever CSC38B

## 4.2 Conclusion

In this chapter, the material modification shows a suppressed effect for spurious peaks. Next, the adjustable preload holder is developed, and shows that the excitation spectrum can be optimized through adjusting the preload. However, it also changes the preload on the piezoelectric actuators, and the affection needs to be further identified. Finally, the clamp-modification holder is developed. This design isolates the spring clip and the holder base, and avoids the constriction on the piezoelectric actuators. On this holder with simple mechanical structure, both the flexural and torsional peaks can be excited on two different kinds of cantilevers.

## Chapter 5

### Cantilever Detection System

The cantilever detection system is used for measuring the cantilever deformation, and its sensitivity directly affects the force resolution. The astigmatic detection system (ADS) is adopted because of advantages of the small spot size ( $\sim 1 \mu\text{m}$ ), the high bandwidth (80 MHz), and the compact dimensions ( $48.7 \times 36.7 \times 7.5 \text{ mm}$ ) [54]. For realizing effective operation in water, the optimal water thickness is evaluated and examined to minimize the influence of water, and the optical scanning mode in water is also successfully demonstrated. Besides, a time-saving and non-damaging spring constant calibration process is proposed and verified based on the ADS, and this method can be extended to calibrate the other tipless cantilever used in biotechnology.

#### 5.1 Astigmatic Detection Method

The astigmatic detection method is widely used in the digital versatile disk (DVD) pickup head, and its optical configuration is illustrated in Figure 5.1(a). A laser beam is focused onto the cantilever through a collimator and an objective lens. After passing through a cylindrical lens, the reflective laser beam is detected by the photodetector integrated chip (PDIC). As shown in Figure 5.1(b), the four quadrant photosensors (A~D) on the PDIC generate voltage signal  $U_A$ ,  $U_B$ ,  $U_C$ , and  $U_D$ , respectively. When the laser is exactly focused on the cantilever, the laser spot on the PDIC is circular as illustrated at the point (II). But, any defocused displacement  $\pm z$  will cause the laser spot to change into elliptical shape as displayed at points (I) and (III). The cantilever displacement is measured by the focus error signal  $U_{FES} = (U_A + U_C) - (U_B + U_D)$ , and

the  $U_{FES}$  versus cantilever displacement curve (S-curve) characterizes their linear relationship with a range of  $\pm 3 \mu\text{m}$  roughly. The focus error signal  $U_{FES}$  can thus be directly related to the cantilever displacement in the linear region.

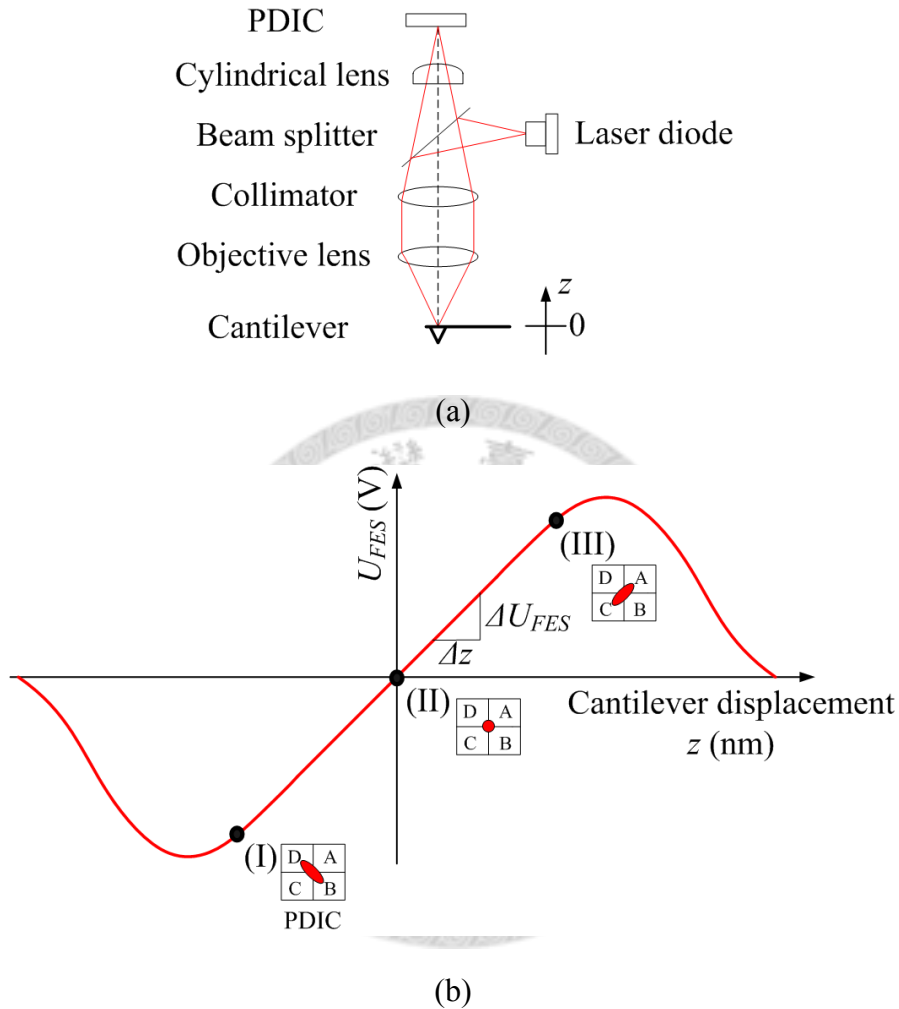


Figure 5.1 (a) Configuration of ADS and (b) focus error signal  $U_{FES}$  versus cantilever displacement

For further experiments, an astigmatic pickup head (TOP1100Sc, TopRay Technologies) is chosen, and its structure and specification are shown in Figure 5.2 and Table 5.1, respectively. The DVD-wavelength of 655 nm is adopted in the experiments, and the diffraction grating in the pickup head is removed for increasing the laser intensity.

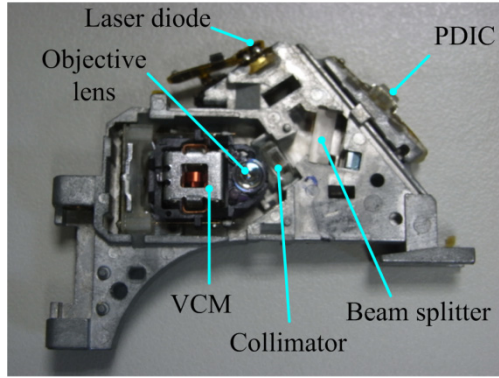


Figure 5.2 Astigmatic pickup head

Table 5.1 Specification of TopRay pickup head

Item	DVD	CD
Laser diode wavelength	655 nm	790 nm
Objective lens	Aspheric plastic lens	Aspheric plastic lens
Focal length (FL)	2.33 mm	2.35 mm
NA	0.6	0.47
Working distance	1.28 mm	0.91 mm
Detection method	Astigmatism	Astigmatism
Photo detector	PDIC with I/V amplifier	PDIC with I/V amplifier
PDIC response frequency	80 MHz	45 MHz
Dimensions	48.7 × 36.7 × 7.5 mm	
Unit weight	~18 g	
Operating temperature	0 ~ 60 °C	

## 5.2 Detective Sensitivity in Water

For reading the data on the DVD optical disc as shown in Figure 5.3(a), the astigmatic pickup head is designed with an objective lens, which has the focal length (FL) of 2.33 mm and the numerical aperture of 0.6. The numerical aperture (NA) and the refractive index  $n_{air}$  of air determine the focused angle  $\theta_{air}$  of laser in air as following Equation (5.1). The laser angle  $\theta_{air}$  in air is 36.87°.

$$NA = n_{air} \sin \theta_{air}, \quad (5.1)$$

A 0.6-mm thick polycarbonates layer refracts the laser beam to focus on the recording layer. Equation (5.2) describes its refractive relation. Through the refractive index  $n_{pc}$  of 1.58, it derives a focusing angle  $\theta_{pc}$  of  $22.32^\circ$ .

$$n_{air} \sin \theta_{air} = n_{pc} \sin \theta_{pc} \quad (5.2)$$

For measuring in water environment, the optical path is modified as Figure 5.3(b). A cover glass is placed above the water layer to avoid a cambered water surface. The thickness  $h_{glass}$  of the cover glass (Hecht Assistant) is 0.15 mm, and its refractive index  $n_{glass}$  is 1.52. The laser angles  $\theta_{glass}$  of  $23.24^\circ$  and  $\theta_{water}$  of  $26.82^\circ$  can be derived from

$$n_{air} \sin \theta_{air} = n_{glass} \sin \theta_{glass} \quad (5.3)$$

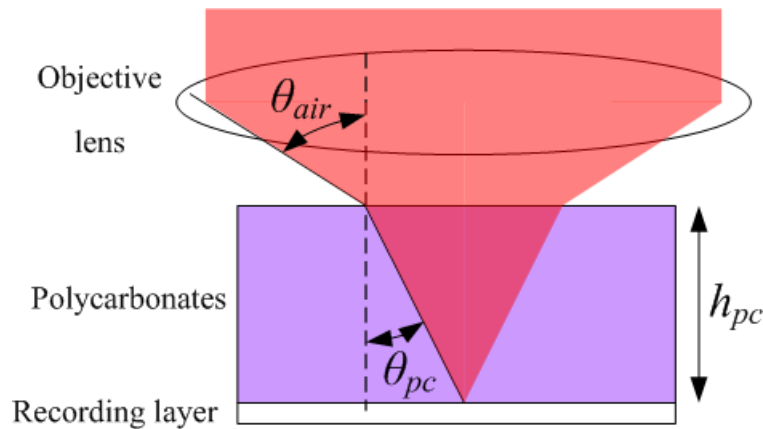
$$n_{glass} \sin \theta_{glass} = n_{water} \sin \theta_{water} \quad (5.4)$$

where the refractive index  $n_{water}$  of water is 1.33.

For compensating the change of mediums, the optimal water thickness  $h_{water}$  needs to be evaluated. Supposing that the laser path before into the glass is unvaried, the water thickness  $h_{water}$  should satisfy

$$h_{pc} \tan \theta_{pc} = h_{glass} \tan \theta_{glass} + h_{water} \tan \theta_{water} \quad (5.5)$$

where the calculated optimal water thickness  $h_{water}$  is 0.36 mm.



(a)

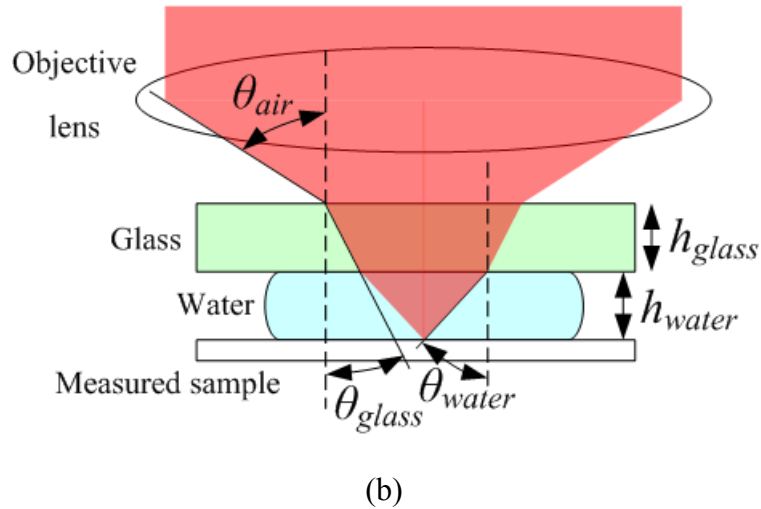


Figure 5.3 Optical paths of (a) DVD optical disc, and (b) water environment

For examining the sensitivity of the ADS, an experimental setup is established as shown in Figure 5.4. Glass slices are stacked on a mirror for adjusting the water thickness  $h_{water}$ , and water is contained between the mirror and the cover glass. The mirror is brought into the working distance of the pickup head through a Z stepper motor, and a closed-loop XYZ scanner (P611.3S NanoCube, Physik Instrumente) is utilized to obtain the S-curve. Besides the original objective lens with FL = 2.33 mm, a plastic aspheric lens with FL = 3.30 mm (CAY033, ThorLab) and a glass aspheric lens with FL = 3.10 mm (352330-B, ThorLab) are also tested for comparison.



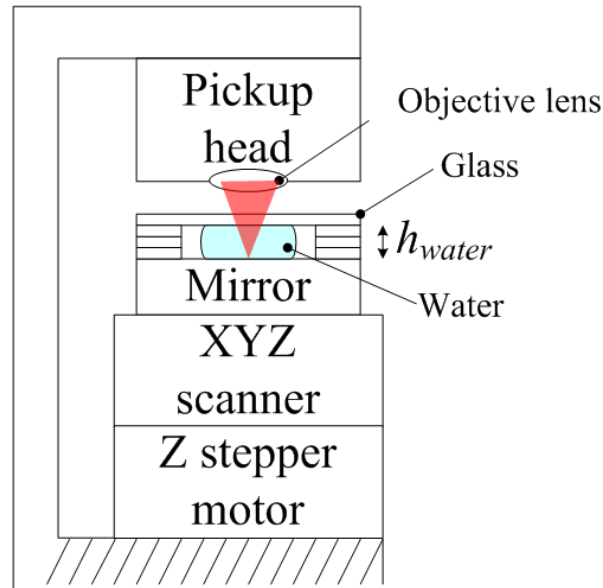
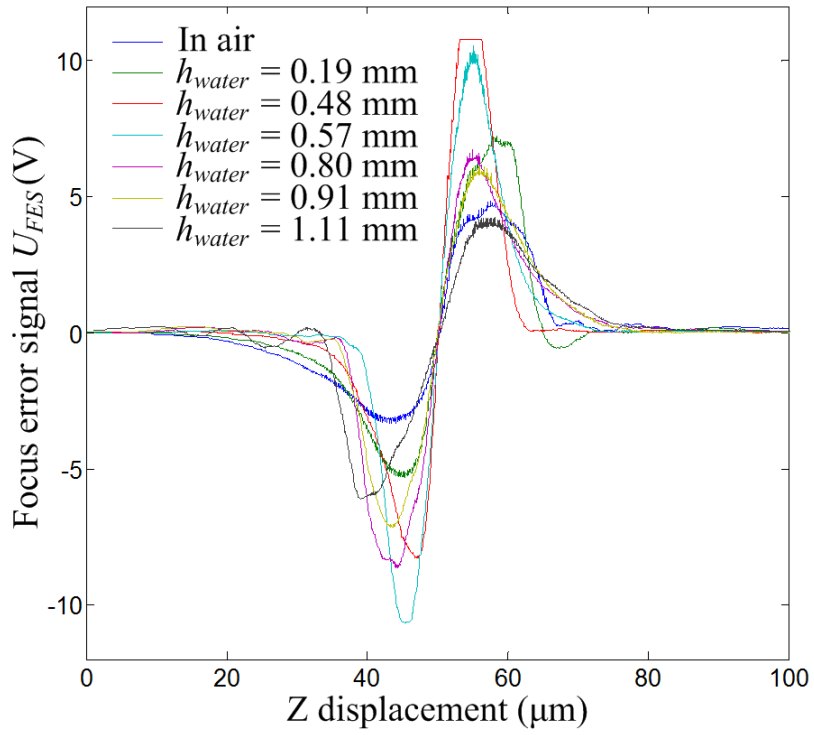
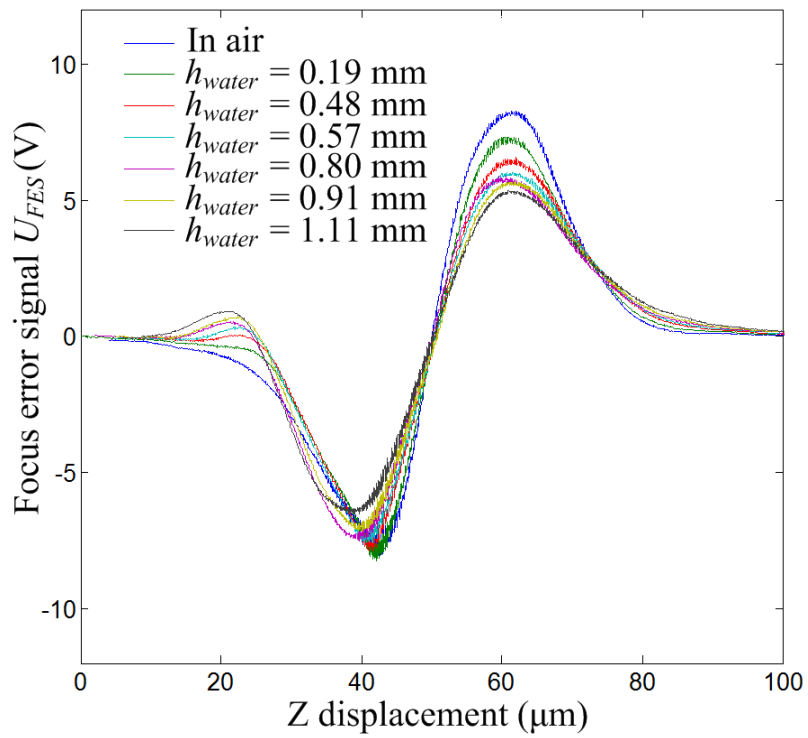


Figure 5.4 ADS sensitivity measurement setup

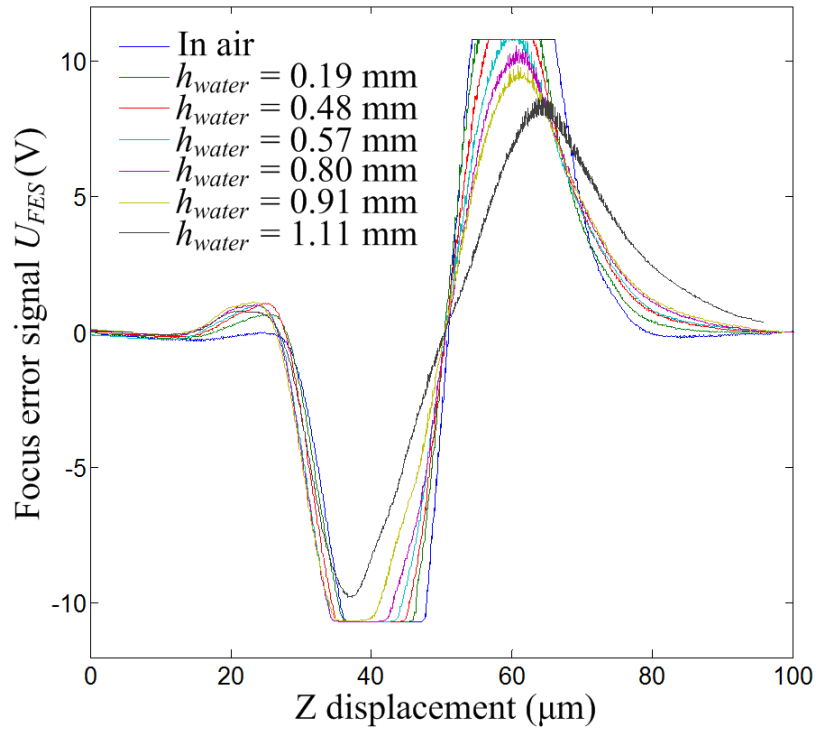
Figures 5.5(a) shows the S-curves equipped with the original objective lens with  $FL = 2.33$  mm, and Figures 5.5(b) and 5.5(c) represent the results of the lenses with  $FL = 3.30$  mm and  $FL = 3.10$  mm, respectively. The overload occurs when  $U_{FES}$  is over  $\pm 10.7$  V due to the output limitation of the pickup head pre-amplifier. The S-curves of the lenses with  $FL = 3.30$  mm and 3.10 mm are more symmetric than that of the original lens with  $FL = 2.33$  mm, and their peak to peak values are inverse proportioned to the water thickness  $h_{water}$ . Under the same water thickness  $h_{water}$ , the S-curve of lens with  $FL = 3.10$  mm has larger peak to peak value than that with  $FL = 3.30$  mm. On the other hand, the curve of the original lens with  $FL = 2.33$  mm has larger peak to peak value at  $h_{water} = 0.19$  and 0.48 mm.



(a) Original lens with FL = 2.33 mm



(b) Lens with FL = 3.30 mm



(c) Lens with FL = 3.10 mm

Figure 5.5  $U_{FES}$  versus displacement curves (S-curves)

The slope of the linear region of the S-curve is calculated through the first degree polynomial curving fitting, and represents the sensitivity  $S_{ADS}$  defined by the  $U_{FES}$  variation per unit displacement. The results are listed in Table 5.2, and the sensitivity variations with the water thickness  $h_{water}$  are shown in Figure 5.6. The lenses with FL = 3.30 mm and FL = 3.10 mm have highest sensitivities in air, and their sensitivities are inverse proportioned to the water thickness  $h_{water}$ . On the other hand, the original objective lens with FL = 2.33 mm has highest sensitivity of 4.040 mV/nm at  $h_{water} = 0.48$  mm. In this condition, the sensitivity approximates to the result obtained by passing through the polycarbonates layer in air. According to the experimental results, the sensitivity can be improved by utilizing an objective lens with short FL. However,

the shorter working distance will raise the difficulty on the cantilever holder design. Therefore, the original objective lens is still adopted, and the optimal combination of the cover glass ( $h_{glass} = 0.15$  mm) and the water thickness ( $h_{water} = 0.48$  mm) is obtained.

Table 5.2 Sensitivity  $S_{ADS}$  of objective lenses under different water thicknesses

Water thickness $h_{water}$ (mm)	Sensitivity $S_{ADS}$ (mV/nm)		
	Original objective Lens with FL = 2.33 mm	Objective Lens with FL = 3.30 mm	Objective Lens with FL = 3.10 mm
0.19	1.869	1.188	2.736
0.48	4.040	0.994	2.119
0.57	3.429	0.979	1.795
0.80	2.074	0.952	1.567
0.91	1.708	0.849	1.344
1.11	0.810	0.760	0.711
In air	1.210	1.569	3.382
Through polycarbonates layer in air	4.209		

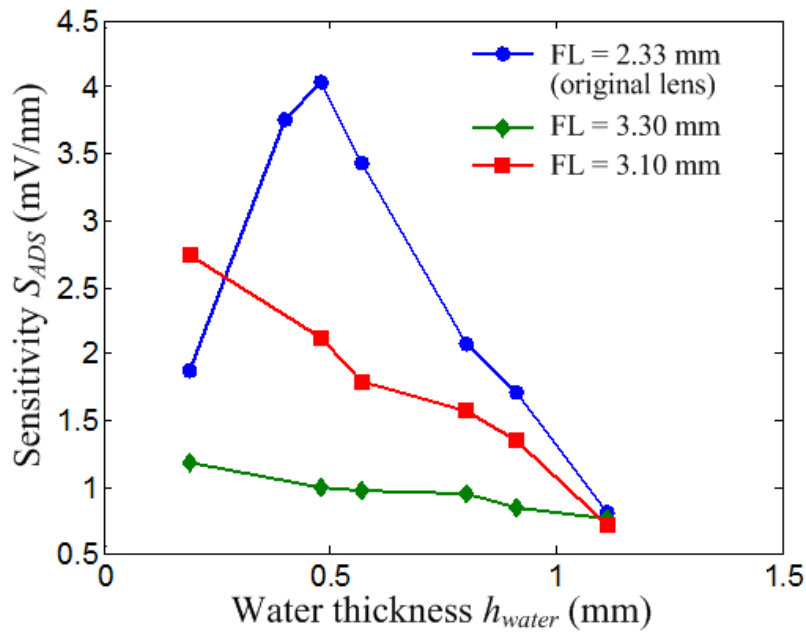


Figure 5.6 Sensitivity  $S_{ADS}$  versus water thickness  $h_{water}$

### 5.3 Optical Scanning Images in Water

For investigating the affections of the water thickness on the laser spatial resolution, the ADS setup in Figure 5.4 is utilized to scan a bio-sample in water [61]. The breast cancer cells Michigan cancer foundation – 7 (MCF-7) are prepared on a silica wafer, and water is dropped between the cover glass and the wafer. The sample is brought into the working distance of the pickup head by the Z stepper motor, and Figure 5.7 shows the S-curves obtained through the XYZ scanner. The blue and green lines represent the results at  $h_{water} = 1.56$  mm and  $h_{water} = 0.55$  mm, respectively. The peak to peak value at  $h_{water} = 1.56$  mm is smaller than that at  $h_{water} = 0.55$  mm, and their sensitivities  $S_{ADS}$  are 0.140 mV/nm and 0.474 mV/nm, respectively. Comparing with the results on the mirror, the sensitivity on the wafer is smaller, because the reflectivity of the wafer is lower than the mirror.

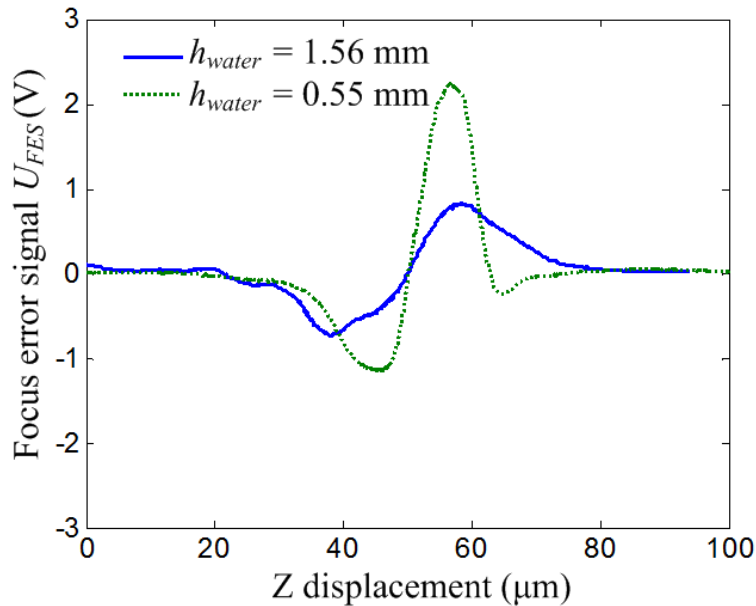
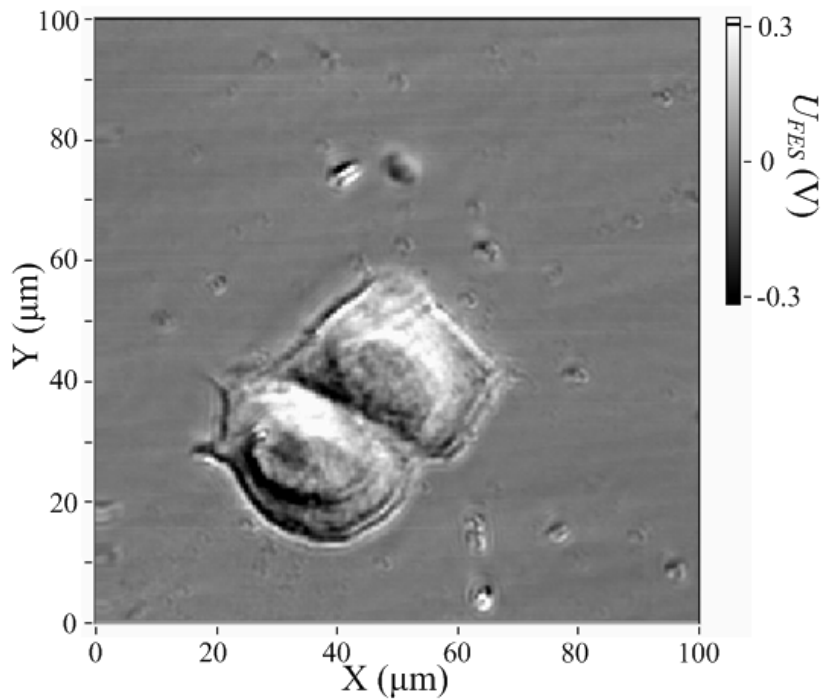
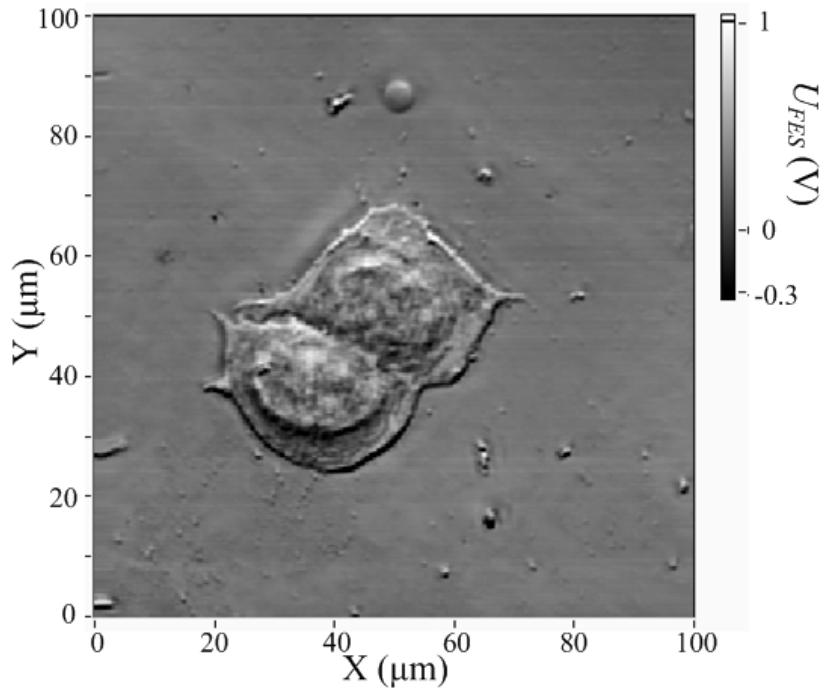


Figure 5.7  $U_{FES}$  versus displacement curves (S-curves)

For searching the target cell on the wafer, an additional optical microscope is equipped to observe the sample surface. When the target cell is positioned in the scan range of the XYZ scanner, the sample is scanned in the XY plane, and  $U_{FES}$  is recorded for imaging simultaneously. The Z position is kept constant during the scanning. Figure 5.8(a) and 5.8(b) show the optical scanning images of the cells at  $h_{water} = 1.56$  mm and  $h_{water} = 0.55$  mm, respectively. At  $h_{water} = 1.56$  mm, diffraction patterns appear around these two cells and particles, and obscure the image. On the other hand, no obvious diffraction can be observed at  $h_{water} = 0.55$  mm. The higher spatial resolution is achieved through applying an appropriate  $h_{water}$ . This result implies that the optimal water thickness  $h_{water}$  not only affects the detection sensitivity, but also changes the measurable minimum dimensions of the cantilever in water.



(a)  $h_{water} = 1.56$  mm



(b)  $h_{water} = 0.55 \text{ mm}$

Figure 5.8 Optical scanning images of MCF-7 breast cancer cell

## 5.4 Spring Constant Calibration

The spring constant of the cantilever is an essential parameter for quantitative measurements. For calibrating the spring constant, the thermal fluctuation method is widely practiced in the commercial AFM, because no extra additive such as the attached mass or information about the cantilever's dimensions is needed. In this method, the Equipartition theorem is used for the spring constant calculation through measuring the cantilever thermal fluctuation. However, for deriving the spring constant with the optical beam deflection technique, it requires to know the sensitivity of the position sensitive detector (PSD) to the cantilever deflection. During a routine calibration procedure, a cantilever probe is brought into contact with a stiff substrate to measure a force curve, which is normally quite time consuming. Not only so, this force measurement cannot be applied to a plain cantilever without a sharp tip, which has been

used in various mass sensing applications. Additionally, the calibration accuracy can also be affected by the potential scattered interference from the substrate in this approach. Furthermore, the tilt angle between the cantilever and the substrate also affects the sensitivity calibration of the PSD slightly.

To establish an efficient procedure, the ADS with the thermal fluctuation method is developed to calibrate the spring constant of cantilevers. In comparison with the technique of optical beam deflection, the ADS is more sensitive to the vertical and less sensitive to the angular displacement of a cantilever. The acquisition of deflection sensitivity of the optoelectronic sensor can be achieved by simply moving the cantilever vertically with a known distance, and no substrate is involved. Therefore, the whole process can be time saving and also avoid damaging the cantilever tip. Furthermore, this new approach can be extended to obtain the spring constant of a tipless cantilever.

#### 5.4.1 Thermal fluctuation method

Without any external excitation, the cantilever is subject to the thermal stimulation at room temperature. According to the well-known Equipartition theorem Equation (5.6):

$$\frac{1}{2}k \langle x^2 \rangle = \frac{1}{2}k_B T, \quad (5.6)$$

where  $k_B$  is Boltzmann's constant,  $T$  is the cantilever temperature in Kelvin, the spring constant  $k$  of an ideal spring can be calculated through measuring its mean square amplitude  $\langle x^2 \rangle$ . Burnham *et al.* derived the thermal distribution function of a simple harmonic oscillator (SHO) [62], and its raw thermal power spectrum can be fitted by the following equation



$$\langle x^2(f) \rangle = \frac{A}{f} + B + \frac{\langle x^2(f_r) \rangle}{Q^2} \frac{1}{\left\{ \left[ 1 - \left( \frac{f}{f_r} \right)^2 \right]^2 + \left[ \frac{f}{f_r Q} \right]^2 \right\}}, \quad (5.7)$$

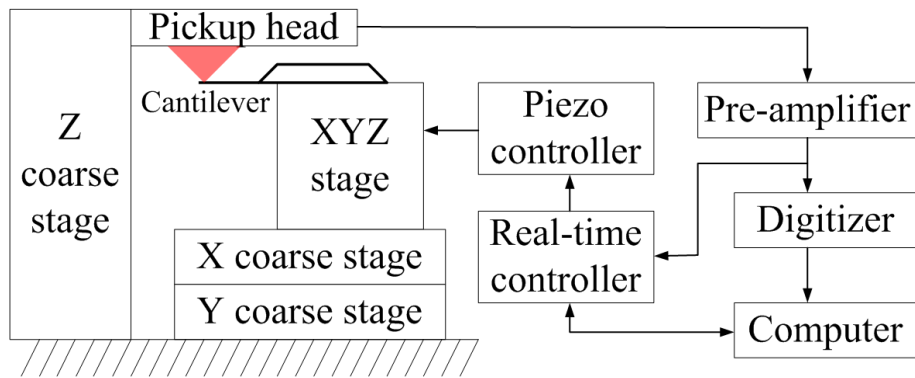
where  $\langle x^2(f) \rangle$  is the mean square amplitude at frequency  $f$ , and the first and second terms represent  $1/f$  noise and white noise, respectively. The parameters  $A$ ,  $B$ , mean square amplitude  $\langle x^2(f_r) \rangle$ , quality factor  $Q$ , and resonant frequency  $f_r$  are obtained from the fitting curve. The spring constant  $k$  can thus be derived by

$$k = \frac{2 k_B T Q \Delta f}{\pi x^2(f_r) f_r}, \quad (5.8)$$

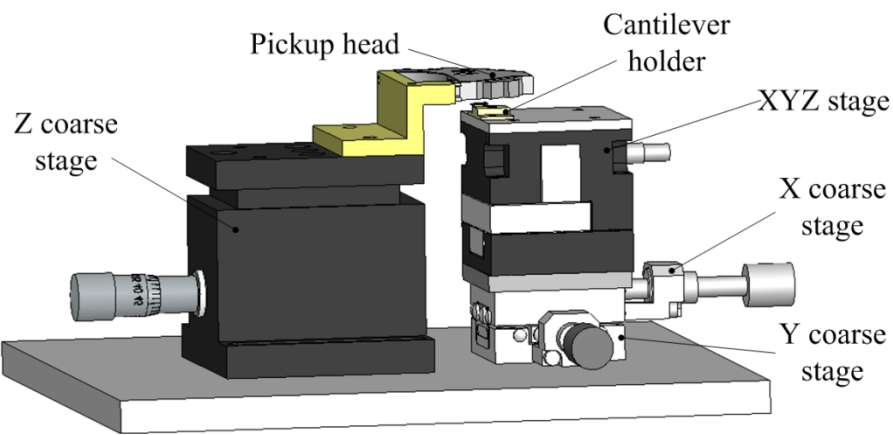
where  $\Delta f$  is the frequency resolution of the thermal power spectrum.

#### 5.4.2 ADS setup for spring constant calibration

Figure 5.9 shows the calibration setup. The astigmatic pickup head (TOP1100Sc, TopRay Technologies) is used to detect the cantilever displacement. The X- and Y-coarse stages are responsible for the alignment of the laser spot on the free end of the cantilever, and the Z-coarse stage for focusing the laser spot on the cantilever. The aligning and focusing processes can be simultaneously monitored by a microscope and a CCD-camera. For deflection sensitivity calibration, a real-time controller (sbRIO-9632, National Instruments) generates the triangular voltage waveform to vertically drive the piezoelectric positioning system, which includes the closed-loop XYZ scanner (P611.3S NanoCube, Physik Instrumente) and the piezo-controller (E644, Physik Instrumente). Its acquired  $U_{FES}$  is processed by the pre-amplifier first and further by the digitizer (PCI-9820, ADLINK) with a sampling rate of 5 MHz. The digitized signal is then delivered to the computer to implement the “Fast Fourier Transform (FFT)” to derive the thermal power spectrum, whose acquired parameters  $x^2(f_r)$ ,  $Q$ , and  $f_r$  are put into the Equation (5.8) to calculate the spring constant  $k$  of the cantilever.



(a)



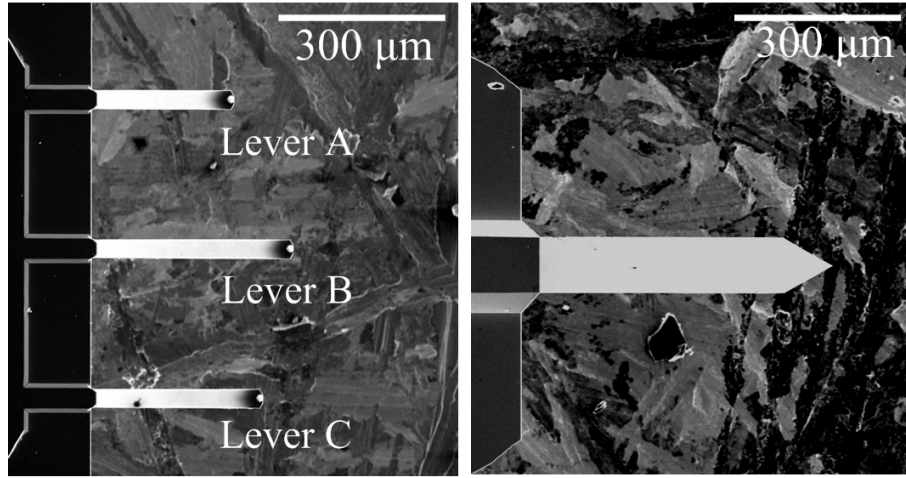
(b)

Figure 5.9 (a) Configuration and (b) construction of calibration setup

### 5.4.3 Calibration on AFM and ADS

For comparison, the spring constants of several cantilevers are separately calibrated by the optical beam deflection technique and our developed ADS. The three-lever chip (CSC38, AIBS, MikroMasch) with three rectangular cantilevers is utilized as the testing sample. The three cantilevers, Lever A, Lever B, and Lever C have same width  $b$  of  $35\ \mu\text{m}$  and thickness  $h$  of  $1\ \mu\text{m}$ , but different lengths  $L$  of  $250\ \mu\text{m}$ ,  $350\ \mu\text{m}$ , and  $300\ \mu\text{m}$ , respectively. In addition, the ADS is also applied to measure the spring constant of a tipless cantilever (Arrow TL1Au, NanoWorld). The scanning

electron microscope (SEM) images of all the cantilevers are displayed in Figure 5.10.

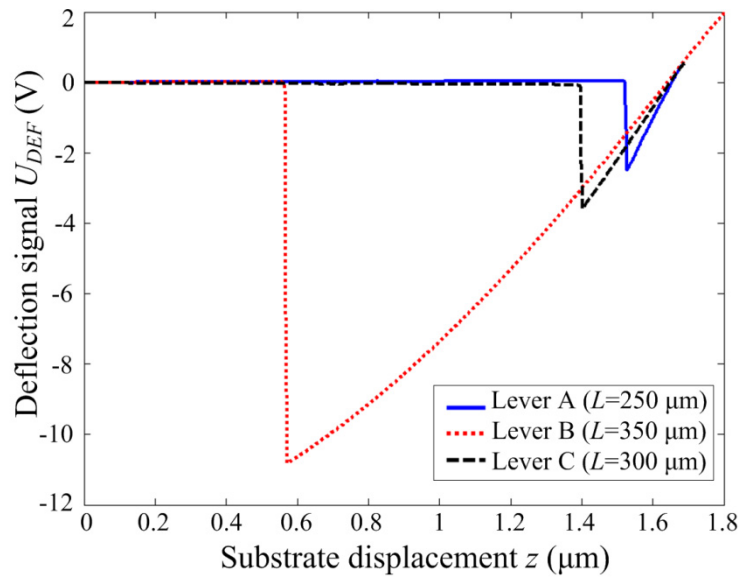


(a) Lever A, B, and C

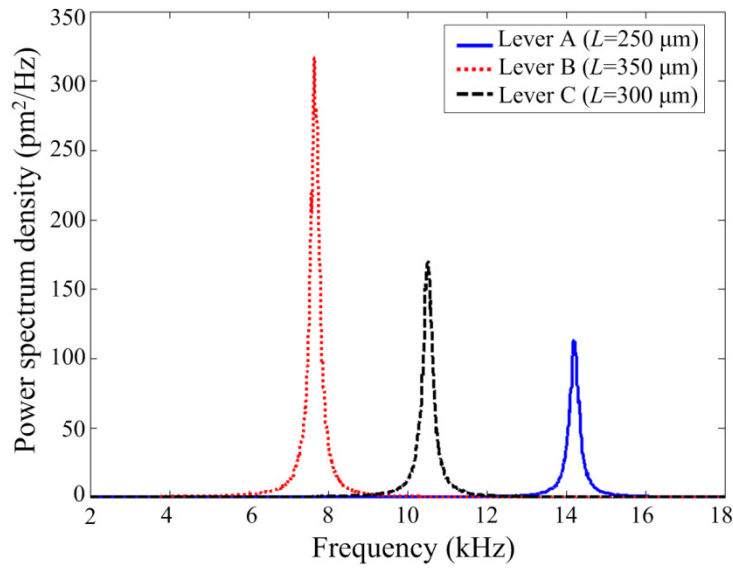
(b) Tipless cantilever

Figure 5.10 SEM images of cantilevers

For demonstrating the optical beam deflection technique, cantilever spring constants are calibrated in a commercial AFM (MultiMode, Bruker). To obtain the flexural deflection sensitivity, the force curves are measured by approaching a sapphire substrate to the cantilevers. The substrate is driven to load and unload the cantilever tip with a defined displacement. Figure 5.11(a) shows the measured cantilever deflection signal  $U_{DEF}$ . From the slopes on the ramp regions, the deflection sensitivities  $S_{OBD}$  on the Levers A, B, and C are 18.6 mV/nm, 12.3 mV/nm, and 14.6 mV/nm, respectively. For the same linear displacement, the shorter cantilever produces a larger angular deflection than the longer ones and, consequently, a larger voltage variation on  $U_{DEF}$ . The longer cantilever also requires a larger movement to detach from the substrate after the contact has been made. Figure 5.11(b) shows the thermal fluctuation spectrums of the three cantilevers. The resonant frequencies  $f_r$  of the Levers A, B, and C are 14.2 kHz, 7.7 kHz, and 10.5 kHz, and their corresponding spring constants  $k_{OBD}$  are 0.073 N/m, 0.030 N/m, and 0.047 N/m, respectively.



(a) Force curves on sapphire substrate

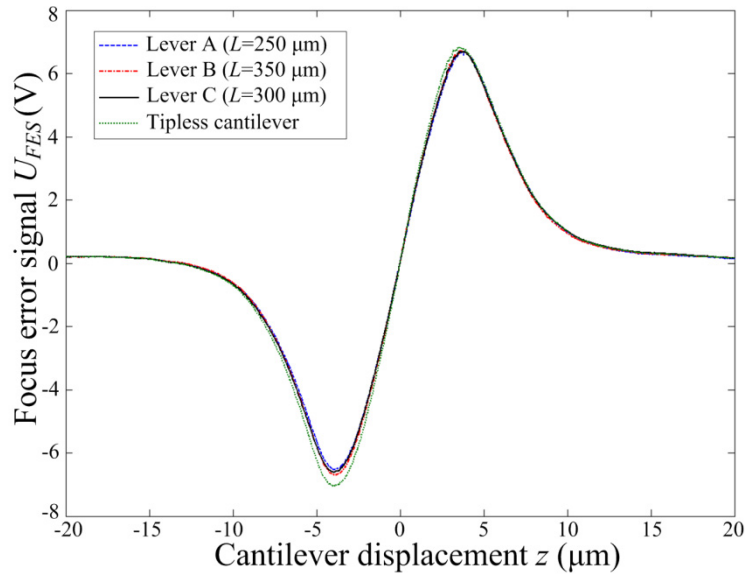


(b) Thermal fluctuation spectrums

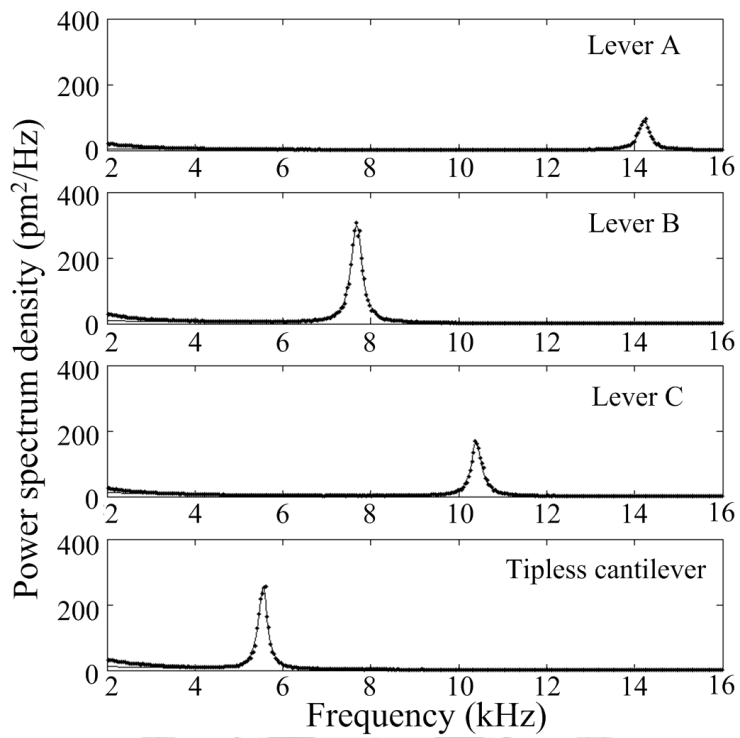
Figure 5.11 Experimental results on AFM

On the ADS, through the linear actuation by using the closed-loop controlled piezo stage, the S-curves of the Levers A, B, C, and the tipless cantilever are acquired and shown in Figure 5.12(a). The slopes in the middle linear regions of the S-curves are

used for calibration of the deflection sensitivities. The deflection sensitivities  $S_{ADS}$  of the Levers A, B, C, and the tipless cantilever are 2.5 mV/nm, 2.6 mV/nm, 2.5 mV/nm, and 2.8 mV/nm, respectively. Their thermal fluctuation spectrums are shown in Figure 5.12(b). The resonant frequencies  $f_r$  of the Levers A, B, and C are 14.2 kHz, 7.7 kHz, and 10.4 kHz, and the corresponding spring constants  $k_{ADS}$  are 0.090 N/m, 0.029 N/m, and 0.056 N/m. The resonant frequency  $f_r$  and spring constant  $k_{ADS}$  of the tipless cantilever are 5.5 kHz and 0.041 N/m. Table 5.3 provides an overview of all experimental results.



(a) S-curves



(b) Thermal fluctuation spectrums

Figure 5.12 Experimental results on ADS

Table 5.3 Experimental results on AFM and ADS

	Nominal spring constant (N/m)	AFM		ADS	
		Measured deflection sensitivity $S_{OBD}$ (mV/nm)	Measured spring constant $k_{OBD}$ (N/m)	Measured deflection sensitivity $S_{ADS}$ (mV/nm)	Measured spring constant $k_{ADS}$ (N/m)
Lever A ( $L=250\mu\text{m}$ )	0.08	18.6	0.073	2.5	0.090
Lever B ( $L=350\mu\text{m}$ )	0.03	12.3	0.030	2.6	0.029
Lever C ( $L=300\mu\text{m}$ )	0.05	14.6	0.047	2.5	0.056
Tipless cantilever ( $L=500\mu\text{m}$ )	0.03	Not available	Not available	2.8	0.041

The deflection sensitivities  $S_{OBD}$  of the Levers A, B, and C derived on the AFM are significantly related to the cantilever length. On the contrary, their measured deflection sensitivities  $S_{ADS}$  on the ADS are very close, but  $S_{ADS}$  of the tipless cantilever is higher than the others slightly. The difference comes from the reflectivity difference between the gold coating on the tipless cantilever and the aluminum coating on the Levers A, B, and C. On the spring constant, a similar result has been obtained with both the AFM and ADS methods for the longest Lever B. Yet, the apparent disagreements were also found for the Levers A and C. As for which method generates more accurate outcome, it remains to be examined. Nevertheless, our current proposed calibration method with the ADS is experimentally verified as an efficient procedure without application of a substrate. It also provides a natural extension to calibrate the tipless cantilever, which acts as a key component in cantilever-based mass sensors.

## 5.5 Conclusion

For applying the ADS to water environment, its measurement sensitivity is investigated. Through calculating the equivalent water thickness to the polycarbonates layer in DVD optical disc, the optimal water thickness  $h_{water}$  of 0.36 mm is derived. In the experiments, the highest sensitivity  $S_{ADS}$  of 4.040 mV/nm is obtained at  $h_{water} = 0.48$  mm, which approximates to the sensitivity through a polycarbonates layer in air. Besides, the water thickness  $h_{water}$  also affects the spatial resolution on the optical scanning mode. A sample of the breast cancer cell MCF-7 is scanned, and the unwanted diffraction patterns can be eliminated by applying an appropriate  $h_{water}$ .

By using this ADS, a novel calibration method for the spring-constants of micro cantilevers is developed. In comparison with the calibration technique of optical beam

deflection used in the AFM, no substrate is needed in the ADS-calibration. Therefore, it avoids all effects induced by the substrate such as the laser interference, capillary force, cantilever tilt, and tip blunting. Besides, this method can be applied to tipless cantilevers, which are widely applied in many cantilever-based mass sensors. Furthermore, this developed ADS-calibration is also time efficient by omitting tip-substrate approaching procedure.





## Chapter 6

### Liquid Environment AFM

Based on the experiences of cantilever design, excitation method, and detection method, a liquid-AFM system is designed and developed for adapting to the detection in liquid environment. In order to widen its application field, torsional cantilever excitation is also integrated into the system. For realizing sample scanning, resonant cantilever tapping and precision signal processing, an embedded controller configuration is developed and built up with a real time processor and a field-programmable gate array (FPGA). And for fulfilling AFM-process, the LabVIEW System Design Software is applied for programming whole system functions and the user interface. The performance of the liquid-AFM system is experimentally verified by detecting different samples in both air and liquid environments.

#### 6.1 System Configuration

Figure 6.1 shows the configuration of the liquid environment AFM system. The AFM system can be distinguished into the mechanical system, the electronic control system, and the user interface. In the mechanical system, the cantilever holder is designed for reducing spurious peaks in liquid, and provides both flexural and torsional excitation by dual piezoelectric actuators. The astigmatic pickup head (TOP1100Sc, TopRay Technologies) is adopted to detect the cantilever deflection, and the water thickness is optimized for improving the sensitivity in water. The cantilever holder and the pickup head are installed on two XYZ stages individually (B70-60RK and B70-60RK, SURUGA SEIKI) to adjust their positions arbitrarily. The closed-loop XYZ

Scanner (P-363.3CD PicoCube, Physik Instrumente) and the scanner controller (E-536 PicoCube Controller, Physik Instrumente) are used for precise sample scanning with the closed-loop resolution of 0.1 nm. The sample is brought into the scan range by a motorized Z stage. In the electronic control system, a programmable embedded controller (sbRIO-9632, National Instrument) is utilized to realize the AFM functions and integrate the sub-systems. A real time processor and a field-programmable gate array (FPGA) are built-in inside the embedded controller. The 16 bits analog outputs (voltage range: -10 ~ 10 V) with 100 kHz sampling rate provide the XYZ-axes control signals, which are amplified to a suitable voltage range (XY-axes: 0 ~ 10 V, Z-axis: 0 ~ 2 V) for the scanner controller. The Z stepper motor is driven by a motor driver, which is commanded through the digital outputs. For exciting the piezoelectric actuators (PZT), the driving signal is also generated from the digital output, and converted to the analog signal through a digital-to-analog converter (DAC) (DC245A-A, Linear Technology) with the sampling rate of 5 MHz. The focus error signal  $U_{FES}$  is generated by a PDIC amplifier [63]. In the tapping mode, an amplifier (SR560, Stanford Research) with an adjustable band-pass filter is equipped for increasing the signal to noise ratio. Then, the focus error signal  $U_{FES}$  is captured through an analog-to-digital converter (ADC) (DC919A-A, Linear Technology). The user interface in the personal computer (PC) and the functions in the embedded controller are programmed by the LabVIEW software. Furthermore, for avoiding the vibration from the ground, the mechanical system is placed on an active vibration isolation system (MOD-1M Plus, Halcyonics). An acrylic glass cover is used to isolate the airflow disturbance.

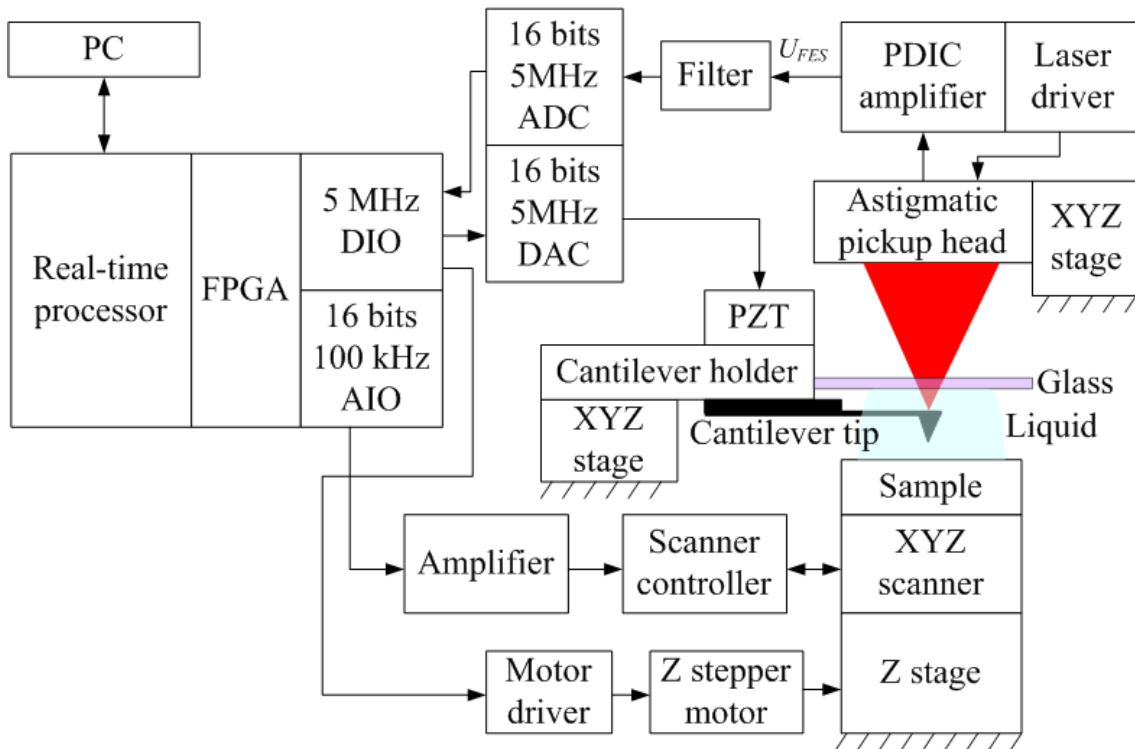


Figure 6.1 Configuration of liquid-AFM

### 6.1.1 Equipment construction

The equipment construction is illustrated in Figures 6.2. For avoiding the vibration on the pickup head and the cantilever due to the scanning motion, the scanning sample type is adopted. Besides, the Z Stage is placed under the XYZ scanner for reducing the vibration on the pickup head during the tip-sample approaching, and avoiding any signal variations due to the cable stretch. Besides, only one stepper motor is necessary, and the vertical sample movement can be achieved by the linear guides simply. The Z stage is composed of two trapezoid parts mainly, and the vertical and horizontal preloads are provided by two springs inside, respectively. The stepper motor pushes the lower trapezoid horizontally with a average displacement of 17 nm/step. Through the 30° trapezoid design, the vertical average displacement is further reduced to 9 nm/step. The smaller step displacement can reduce the risk of tip damage during the tip-sample

approaching, and the 30° trapezoid design also increase the vertical mechanical stiffness. However, this design causes a longer mechanical loop between the tip and the sample, and could be more sensitive to the temperature variation. Therefore, the Z stage is made by steel to decrease the material thermal expansion.

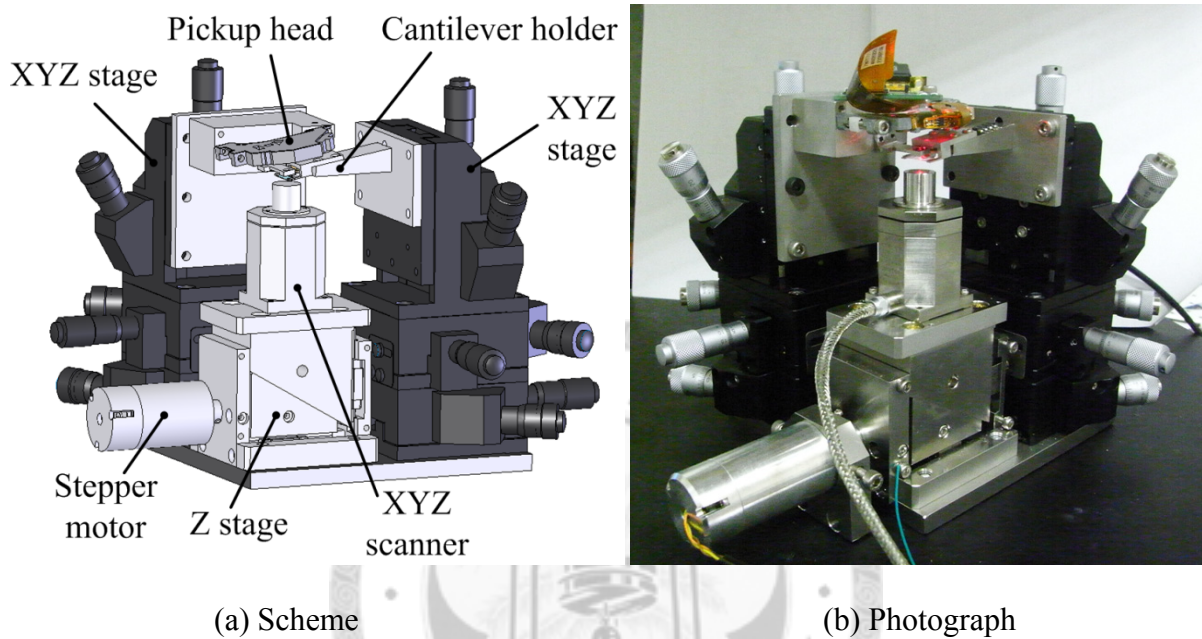


Figure 6.2 Equipment construction

The cantilever holder design is shown in Figure 6.3. The dual piezoelectric actuators are utilized to generate either the flexural or the torsional excitation. The piezoelectric actuators and the steel chip support are isolated by a PEEK isolator for reducing the acoustic wave propagation. The cantilever chip is clamped by a steel spring clip, which is screwed on the chip support directly. This design avoids the acoustic wave propagation from the spring clip, and no preload variation occurs on the piezoelectric actuators. For operation in liquid environment, a cover glass is placed between the cantilever tip and the objective lens. The distance between the cantilever and the cover glass is about 0.5 mm to obtain the optimal detection sensitivity in water. For air environment, the cover glass is replaced by a polycarbonates chip. To avoid the

mechanical interference between the pickup head and the cantilever holder, the objective lens is moved to a lens holder from the pickup head. The tilt angle of the cantilever is  $9^\circ$  to ensure that the tip is the closest part to the sample.

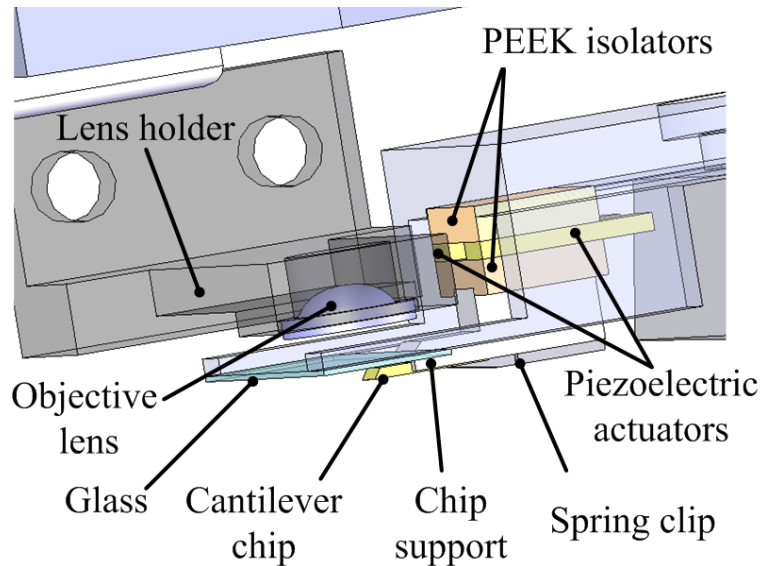
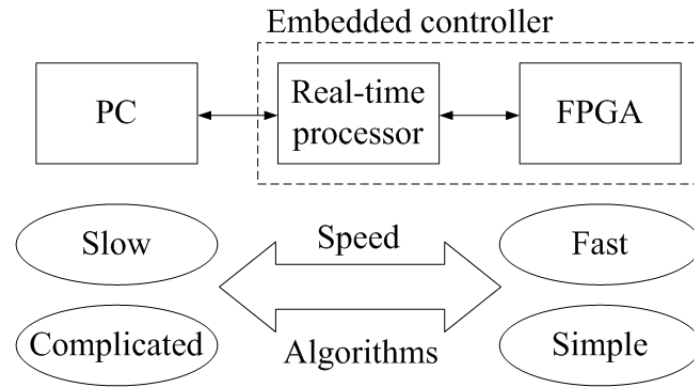


Figure 6.3 Cantilever holder

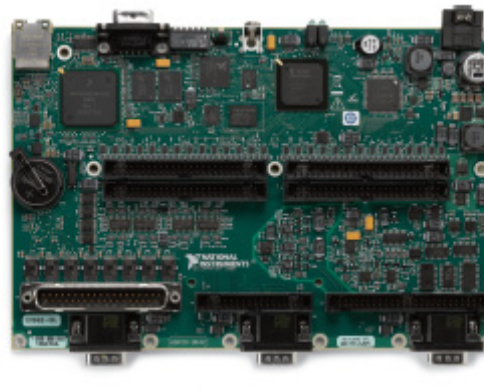
### 6.1.2 Electronic control system

As shown in Figure 6.4, the control system is built on the programmable embedded controller (sbRIO-9632, National Instrument), which includes a 400 MHz real-time processor (MPC5200), and a 2M gates FPGA (Xilinx Spartan-3). The FPGA with a 40 MHz internal clock provides high speed operations. However, the limited algorithmic functions and the number of gates restrict the achievable functions in FPGA. Therefore, the functions such as the lock-in amplifier algorithm and the Z-axis feedback control are implemented by the FPGA, because the operational speed is required. On the other hand, large and complicated functions such as data access, image processes, and the user interface are accomplished in the PC. The real-time processor provides a stable speed and bridges the PC and the FPGA. It is also responsible for the XY-axes scanning

control, force curve measurement, and automatic tip-sample approaching.



(a) Design concept of functional assignment

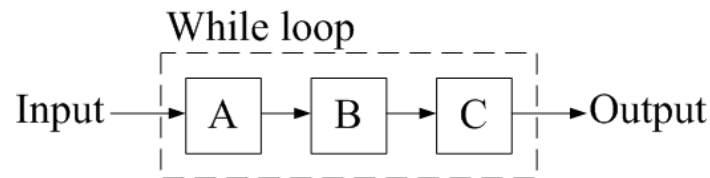


(b) Photograph

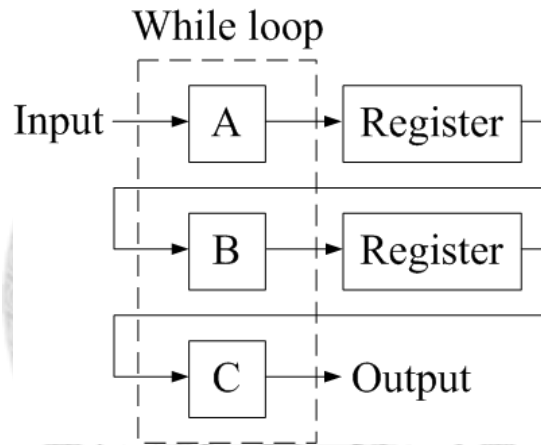
Figure 6.4 Programmable embedded controller

For realizing the lock-in amplifier, the bandwidth is first considered. A typical resonant frequency for the tapping mode AFM is about 300 kHz. However, the sampling frequency of the built-in analog input/output (AIO) in the embedded controller is only around 100 kHz. Therefore, the additional high speed ADC and DAC are connected with the digital input/output (DIO) to achieve 5 MHz sampling rate. Except the sampling rate, the loop rate of the algorithm should be also considered. Although the internal clock in the FPGA is 40 MHz, executing a sequential operation requires a lot of clock periods as illustrated in Figure 6.5(a). To obtain a loop rate of 5 MHz, the pipeline

processing is adopted as shown in Figure 6.5(b). Operations are parallel executed. Each output of an operation is stored in a register, and transferred to the next operation in the next loop. The pipeline method can increase the loop rate significantly. However, the operations should be assigned properly to avoid latency increasing.



(a) Sequential processing



(b) Pipeline processing

Figure 6.5 Processing strategies of lock-in amplifier

Figure 6.6 shows the configuration of the lock-in amplifier. The whole algorithm is divided into two loops. In the main loop, the process includes three stages. The sine and cosine signals are generated in the first stage, and recorded in the register 1. At the second stage, the sine signal is multiplied by an amplitude gain to adjust its amplitude. Next, the sine signal is transmitted to the DAC through the digital outputs, and the analog output from the DAC connects with the piezoelectric actuators to excite the cantilever. On the other hand, the  $U_{FES}$  from the ADC is captured by the digital inputs.

Then, the  $U_{FES}$  is multiplied by the sine and cosine signals individually, and the results are recorded in the register 2. At the third stage, the rectangular coordinates  $X$  and  $Y$  are generated through two low pass filters (LPF). The infinite impulse response (IIR) filter is adopted, and its transfer function  $H(z)$  in z-domain is described by

$$H(z) = \frac{1}{N \left( 1 - \frac{N-1}{N} z^{-1} \right)}, \quad (6.1)$$

where  $N$  is an integer that is adjustable for changing the bandwidth. In the secondary loop, the rectangular coordinates  $X$  and  $Y$  are transformed into the polar coordinates amplitude  $R$  and phase  $\theta$  through a built-in function in LabVIEW with a throughput of 18 cycles/sample. The secondary loop also provides the 5 MHz clock signal to both the ADC and DAC.

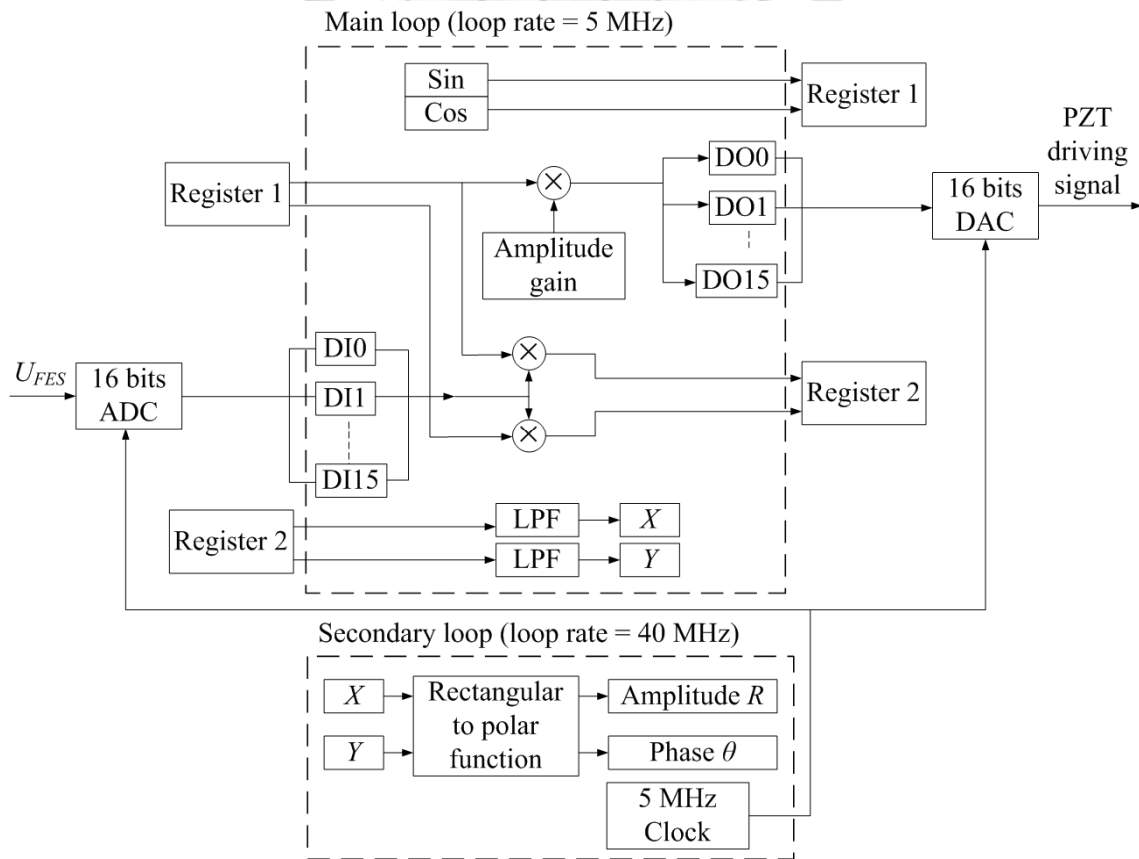


Figure 6.6 Configuration of lock-in amplifier



The Z-axis feedback control loop is illustrated in Figure 6.7. In the tapping mode, the amplitude  $R$  is chosen as the reference signal for the feedback control. For other modes, the external reference signal can be acquired through the analog input (AI). The error signal is calculated by the reference minus the setpoint, which is the tracking target set by user. The proportional-integral (PI) controller is utilized to compensate the Z-axis output signal  $Z_{out}$ . In the proportional controller, the error is multiplied by the P-gain simply. In the integral controller, the error is multiplied by the P-gain, and is accumulated for eliminating the steady state error. The error accumulation will be paused for avoiding overflow if the  $Z_{out}$  reaches the maximum/minimum value. The  $Z_{out}$  is the summation of the outputs from the proportional and integral controllers. When the feedback control is switched off, the  $Z_{out}$  is set to a constant defined by user.

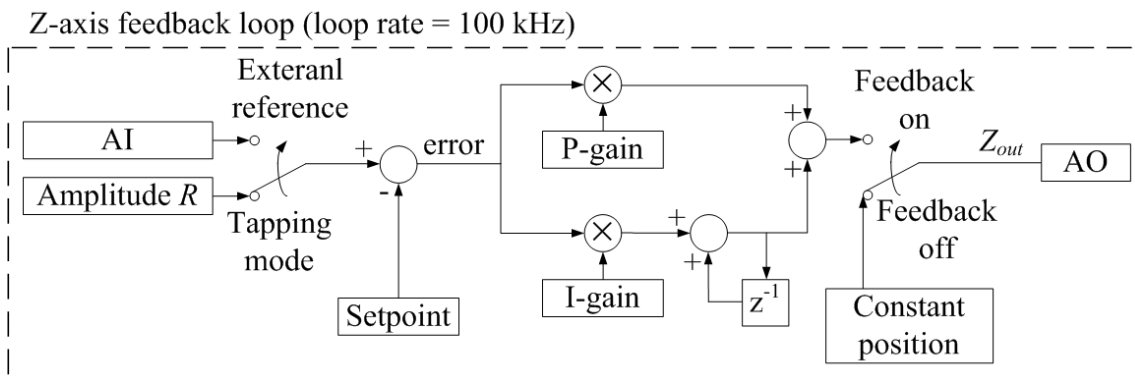


Figure 6.7 Z-axis feedback control configuration

Figure 6.8 shows the scanning control procedure. The scanner is set to the initial position in the beginning. After the Z-axis feedback is switched on, and the line scan is executed. The data such as the height, the amplitude, and the phase are transmitted to the PC after finishing one line scan. Then, the scanner moves to the initial position of the next line, and repeats the line scan until completing the final line.

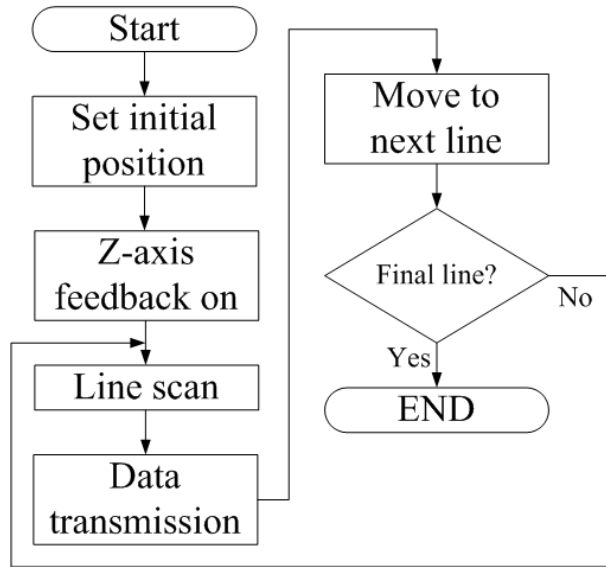


Figure 6.8 Scanning control flowchart

The raster scan method is utilized for scanning, and the scan area can be rotated arbitrarily. To set the scanner initial position with a rotational angle  $\theta_r$ , the calculation is illustrated in Figure 6.9. The largest black square represents the full scan range of the scanner. The blue square with dashed line is the scan range without the rotation, and its initial coordinates are denoted by  $(x, y)$ . First, the offset of  $(x, y)$  is subtracted, and the shifted coordinates  $(x_o, y_o)$  become

$$(x_o, y_o) = (x - x_{offset}, y - y_{offset}). \quad (6.2)$$

The rotated coordinates  $(x_o', y_o')$  can be obtained by

$$[x_o', y_o'] = [x_o, y_o] \begin{bmatrix} \cos \theta & \sin \theta \\ -\sin \theta & \cos \theta \end{bmatrix}, \quad (6.3)$$

and then  $(x_o', y_o')$  are shifted back to get the final initial coordinates  $(x', y')$  as

$$(x', y') = (x_o' + x_{offset}, y_o' + y_{offset}) \quad (6.4)$$

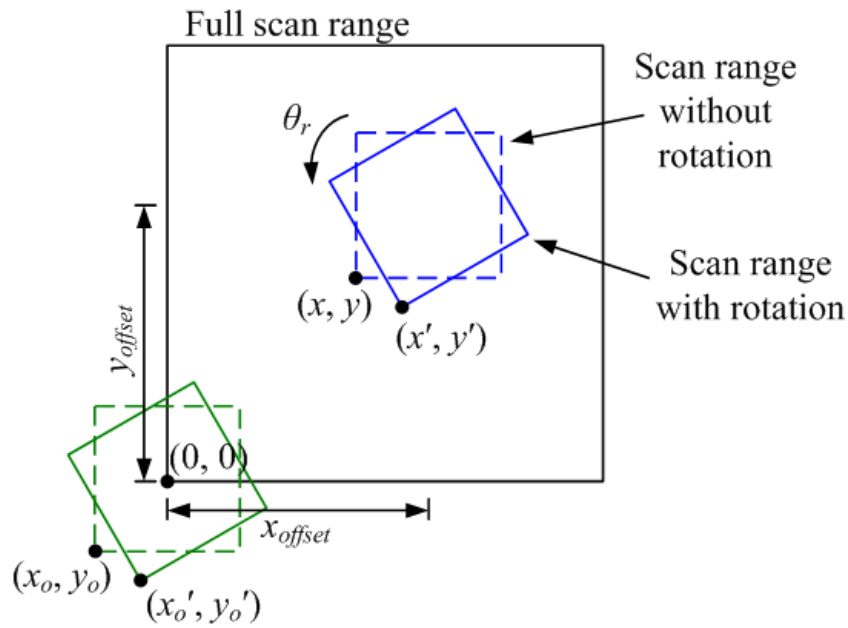
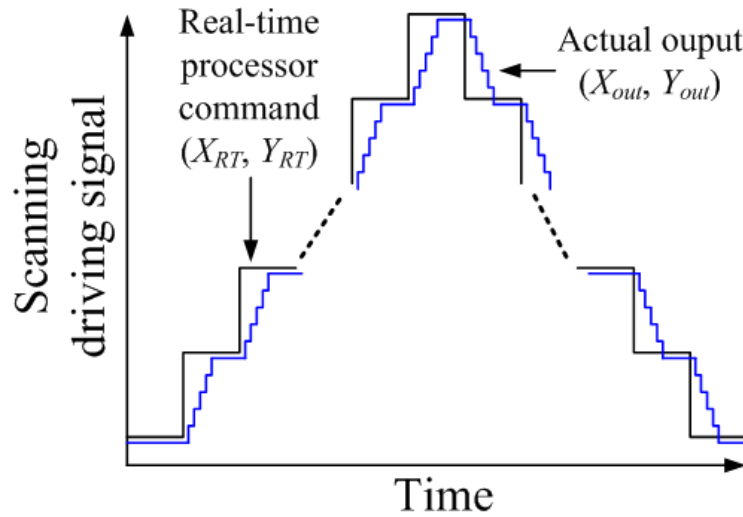


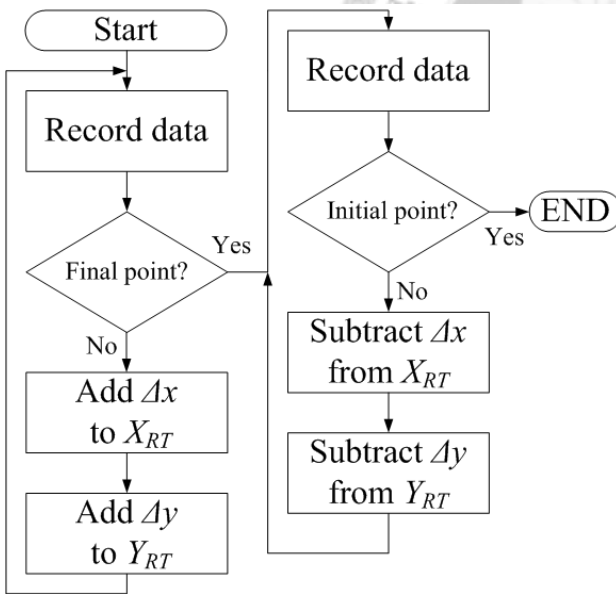
Figure 6.9 Scheme of coordinate rotational of scan range

During the line scan, triangular waveforms are used to control the X-axis and Y-axis displacement, and their amplitudes depend on the scan range and the rotational angle  $\theta_r$ . However, as the black line in Figure 6.10(a), the driving signal  $(X_{RT}, Y_{RT})$  in the digital real-time processor is not perfect triangular. If the displacement on each step is too large, this driving signal could cause an oscillatory step response of the scanner. For avoiding this problem, a slew rate limitation is accomplished by the FPGA, and the blue line represents the final driving signal  $(X_{out}, Y_{out})$ . Figure 6.10(b) and 6.10(c) show the flowcharts in the real-time processor and the FPGA, respectively. Each line scan can be divided into the forward and backward trajectories. In the forward trajectory, the displacement  $(\Delta x, \Delta y)$  of one step is added to  $(X_{RT}, Y_{RT})$  step by step until the end of the trajectory. In the backward trajectory, the same displacement  $(\Delta x, \Delta y)$  is subtracted from  $(X_{RT}, Y_{RT})$  until the initial position. During the scanning, the slew rate limiter in Figure 6.10(c) is always working with a faster loop rate. If the command position  $X_{RT}$  ( $Y_{RT}$ ) is larger than the current output  $X_{out}$  ( $Y_{out}$ ),  $X_{out}$  ( $Y_{out}$ ) is slightly increased to approach  $X_{RT}$

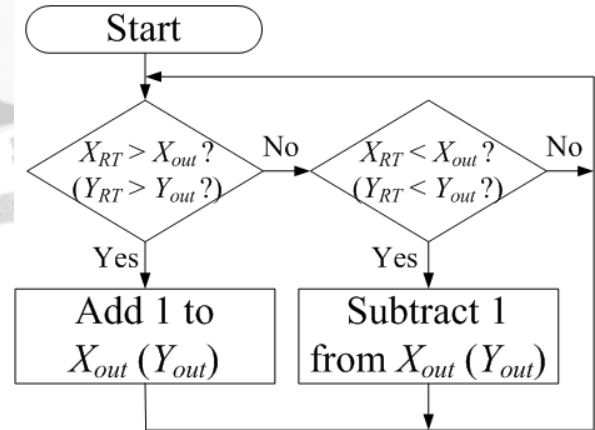
( $Y_{RT}$ ). Reversely,  $X_{out}$  ( $Y_{out}$ ) is decreased when  $X_{RT}$  ( $Y_{RT}$ ) is smaller than  $X_{out}$  ( $Y_{out}$ ). The slew rate is adjustable through changing the loop rate.



(a) Driving signal for scanning



(b) Line scan flowchart in real-time processor



(c) Slew rate limiter in FPGA

Figure 6.10 XY-axes scanning control process

The tip-sample approaching process is illustrated in Figure 6.11, and the continuous approaching method is adopted. At first, the Z-axis feedback control is switched on, and the setpoint must be set properly. After the  $Z_{out}$  reaches the maximum

value, the motor starts to move the sample toward the tip. The  $Z_{out}$  is monitored continuously, and it will decrease when the tip contacts with the sample surface. When the  $Z_{out}$  is less than the half of the full range, the motor is stopped to finish the approaching. At first, the motor speed is tuned for avoiding tip damage. The approaching speed of about 450 nm/sec (50 steps/sec) is chosen, and no overshooting on the  $U_{FES}$  can be observed in this case. For decreasing time consumption, the motor can be controlled manually to bring the sample closer to the tip.

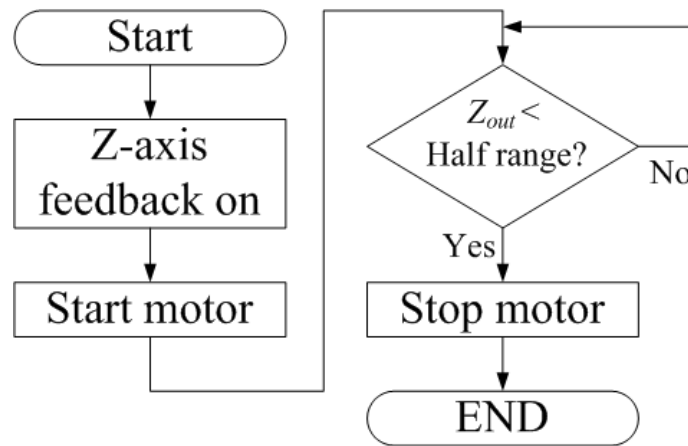


Figure 6.11 Tip-sample approaching process

## 6.2 Experimental Verification

### 6.2.1 Scanning in air

For examining the system performance, different samples are scanned in air first. The polycarbonates chip is installed between the objective lens and the cantilever for achieving optimal sensitivity in air. The tapping mode cantilever PPP-NCHAuD (NANOSENSORS) is adopted, and has a length of 125  $\mu\text{m}$ , a width of 30  $\mu\text{m}$ , and a thickness of 4  $\mu\text{m}$ . Its typical resonant frequency is 330 kHz with the spring constant of 42 N/m. Figure 6.12 shows the excitation spectrum of the cantilever in air, and its resonant frequency and Q-factor are 316.58 kHz and 536, respectively. The slope in

the phase plot represents the time delay in the system.

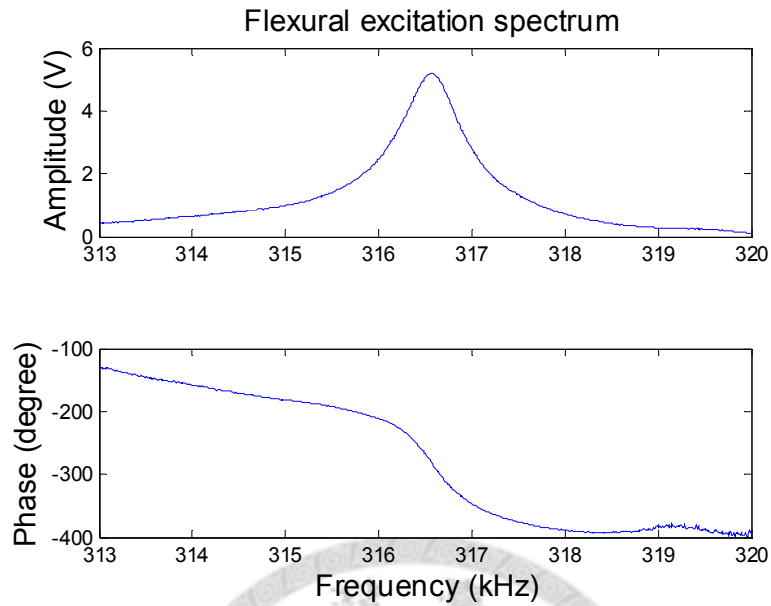
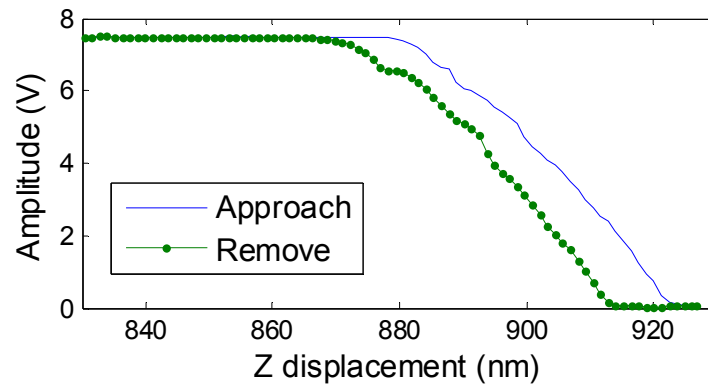


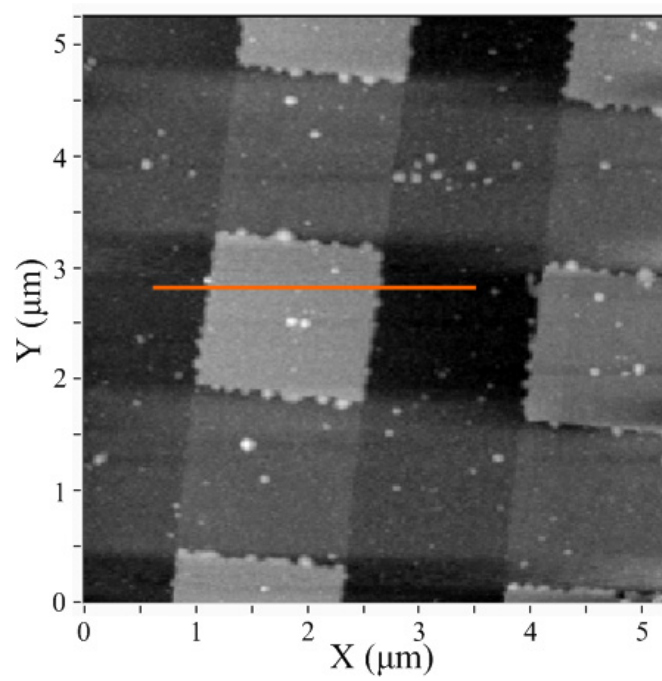
Figure 6.12 Flexural bode plot of cantilever PPP-NCHAuD in air

For calibrating the scanner displacement, a square test grating (TGQ1, NT-MDT) is scanned. The voltage amplitude of the driving signal for the piezoelectric actuators is 15 mV. From the force-displacement curve shown in Figure 6.13(a), the free amplitude of the cantilever is about 40 nm. The blue line and the green dotted line represent the approaching curve and the removing curve, respectively. Figure 6.13(b) shows the scanning topographic image, and the structure period of 3  $\mu\text{m}$  shows the accurate calibration in the XY-axes. The feedback setpoint is 88% of the free amplitude, and the P-gain and I-gain are 50 and 1000, respectively. The scan rate is 0.3 lines/sec, and the image pixels are 256 $\times$ 256 points. The polynomial fitting line is subtracted from each scan line for eliminating the surface slope and the low frequency drift between each line. However, the dark artificial regions beside the squares are also caused by this image process. Figure 6.13(c) shows the cross-sectional profile of the orange line in Figure 6.13(b). The height of the square structure is accurate 20 nm after the calibration of the

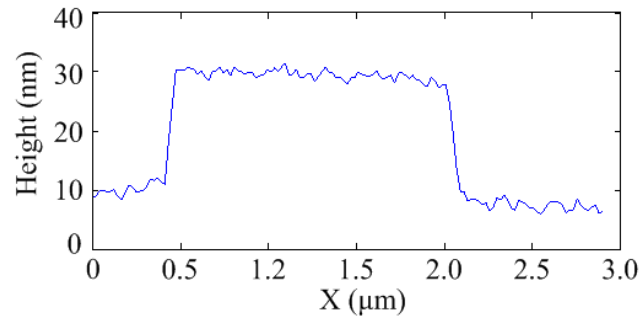
Z-axis.



(a) Force-displacement curve



(b) Topography

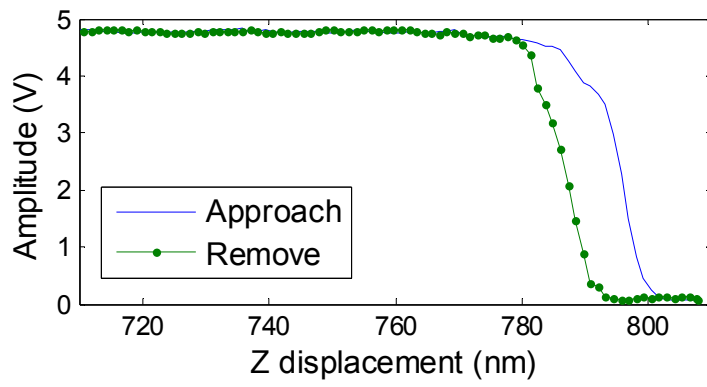


(c) Cross-sectional profile

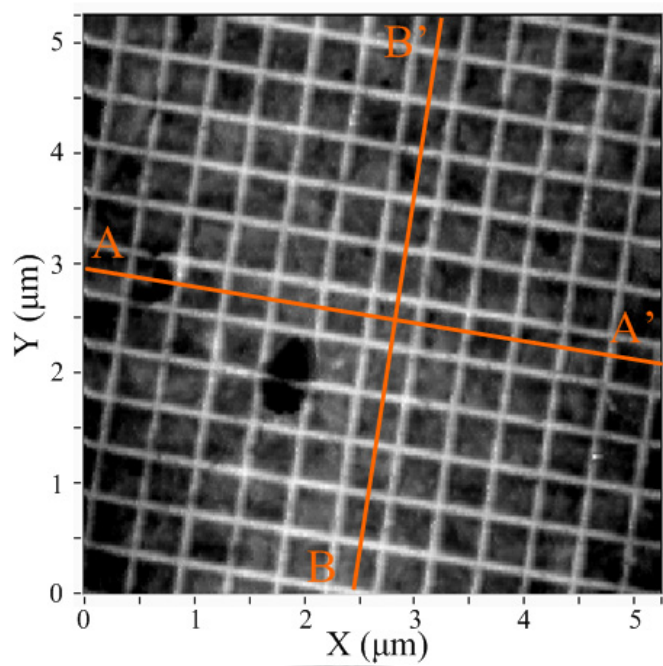
Figure 6.13 Scanning results on test grating TGQ1 in air

For further examining the linearity of the scanner, a meshed test grating (607-AFM, TED PELLA, INC.) is scanned. The force-displacement curve is shown in Figure 6.14(a), and the free amplitude of the cantilever is about 10 nm. Figure 6.14(b) presents the topographic image. The height of the meshed structure is 30 nm, and its period in XY-axes is 0.463  $\mu\text{m}$ . (The feedback setpoint is 89% of the free amplitude, and the P-gain and I-gain are 10 and 1500, respectively. The scan rate is 0.2 lines/sec, and the image pixels are 256 $\times$ 256 points.) The cross-sectional profiles A-A' and B-B' are shown in Figure 6.14(c) and 6.14(e). The peaks are used for the reference points, which are denoted by P1~P11. Figure 6.14(d) and 6.14(e) show the measured displacement at the reference points on the cross-sectional profiles A-A' and B-B', respectively, and their coefficients of determination  $R^2$  are 0.99998 on both cross-sections.

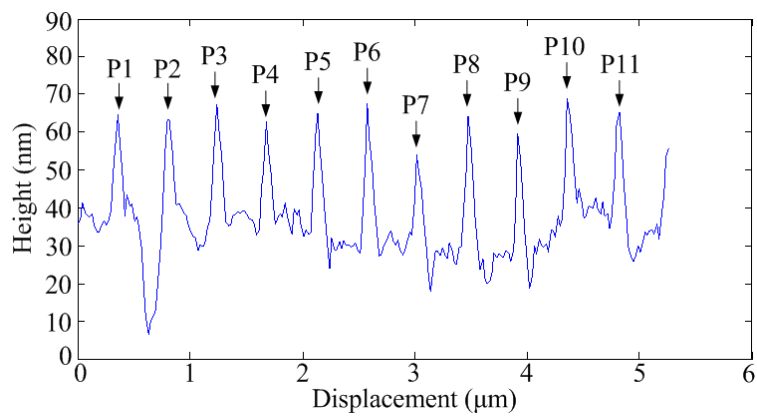




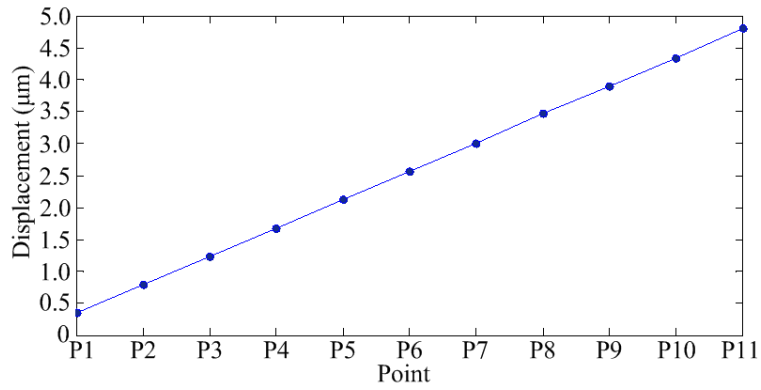
(a) Force-displacement curve



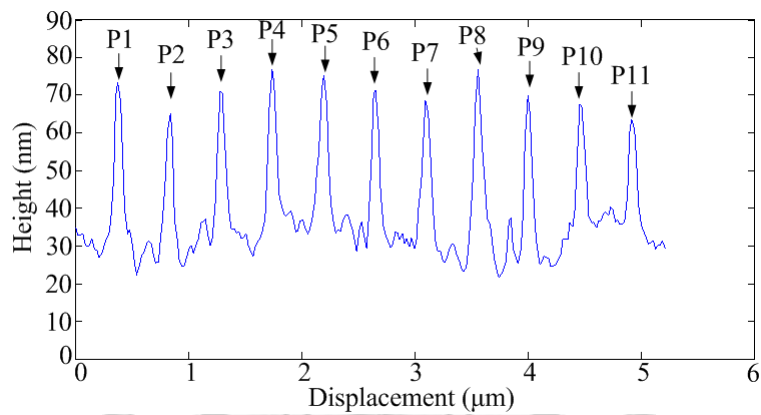
(b) Topography



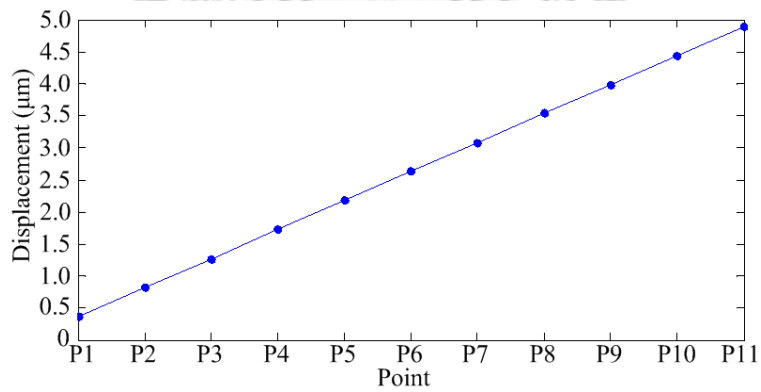
(c) Cross-sectional profile A-A'



(d) Linearity along profile A-A'



(e) Cross-sectional profile B-B'

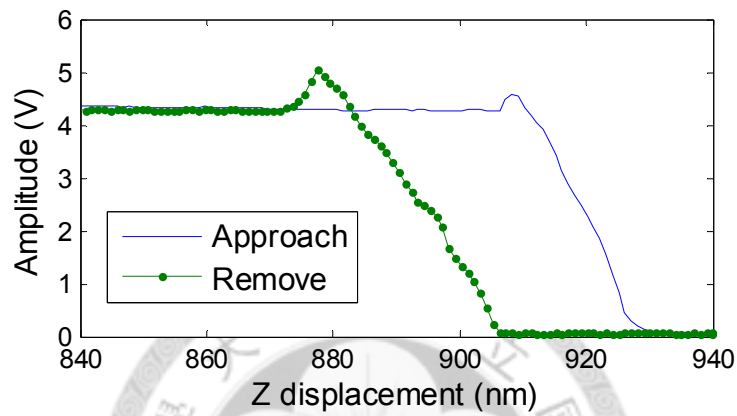


(f) Linearity along profile B-B'

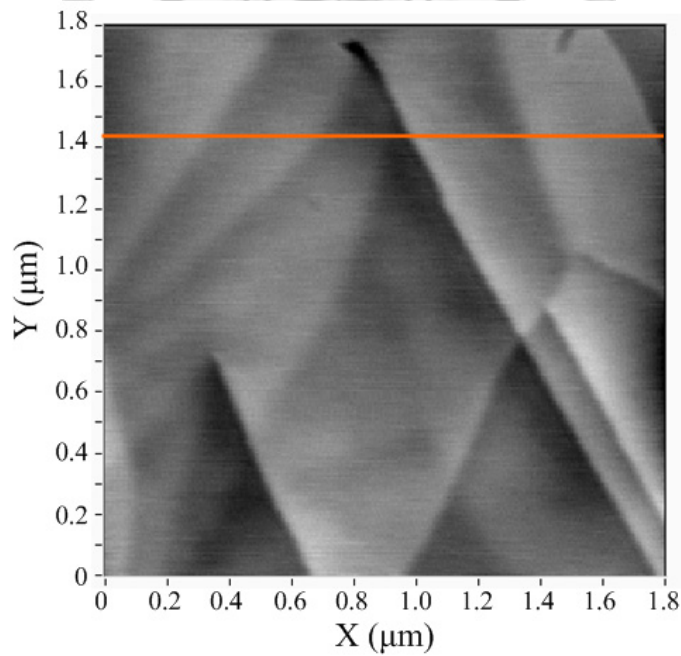
Figure 6.14 Scanning results on test grating 607-AFM in air

A highly oriented pyrolytic graphite (HOPG) is measured for examining the resolution in Z-axis. The force-displacement curve is shown in Figure 6.15(a). Figure

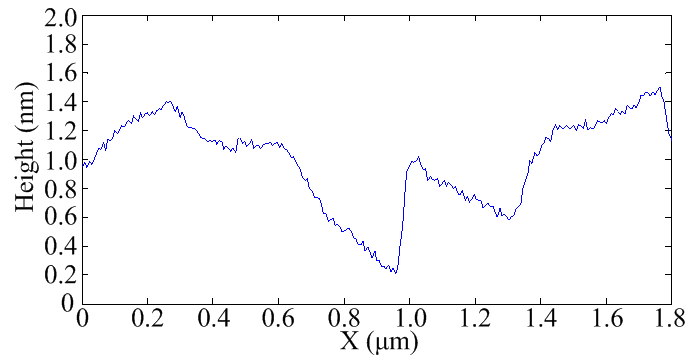
6.15(b) presents the topographic image, and the layer structures of the graphite sample are observed. Figure 6.15(c) shows the cross-sectional profile of the orange line, and the single atomic layer of the graphite can be resolved obviously. (The feedback setpoint is 83% of the free amplitude, and the P-gain and I-gain are 1 and 150, respectively. The scan rate is 0.2 lines/sec, and the image pixels are 256×256 points.)



(a) Force-displacement curve



(b) Topography

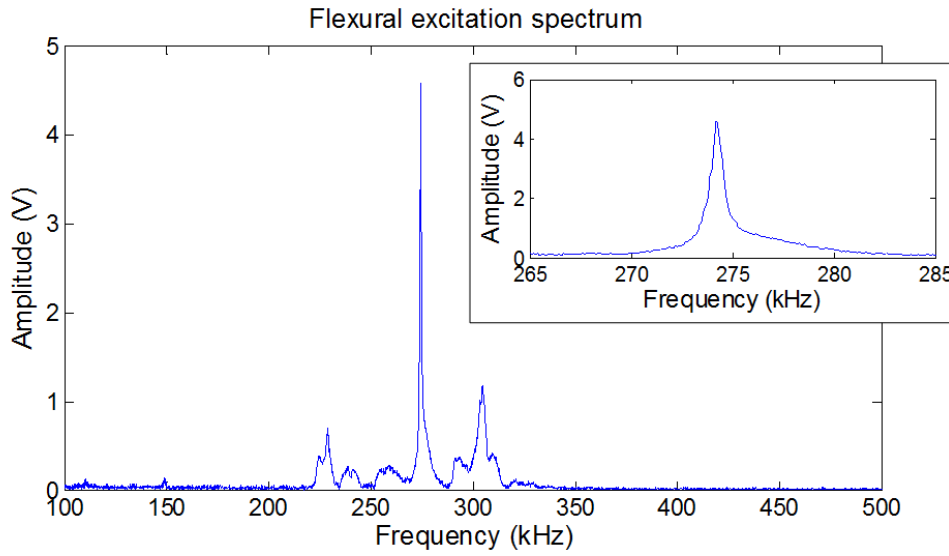


(c) Cross-sectional profile

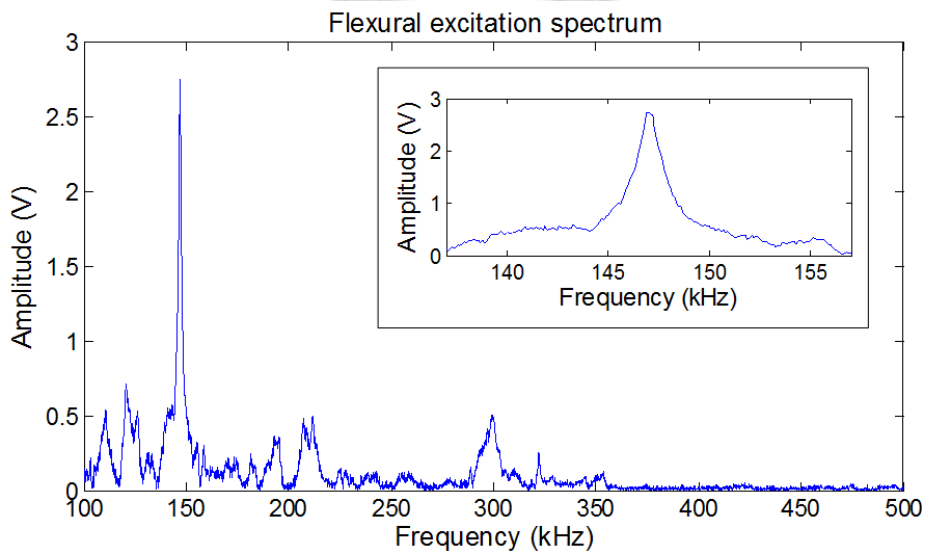
Figure 6.15 Scanning results on graphite (HOPG) in air

### 6.2.2 Scanning in liquid

For the liquid environment operation, the cover glass is installed between the cantilever tip and the objective lens. Comparing the cantilever dynamic properties in air and water, the excitation spectrums of a cantilever PPP-NCHAuD in air and water are shown in the Figure 6.16(a) and 6.16(b), respectively. From the excitation spectrums, the resonant frequencies in air and water are 274.2 kHz and 147.0 kHz, and the Q-factors are 588 and 154, respectively. The spurious peaks are less than 25.9 % and 26.0 % of the resonant peaks in air and water. To obtain similar amplitude, the driving voltage for the piezoelectric actuators in water is usually over ten times than that in air.



(a) In air

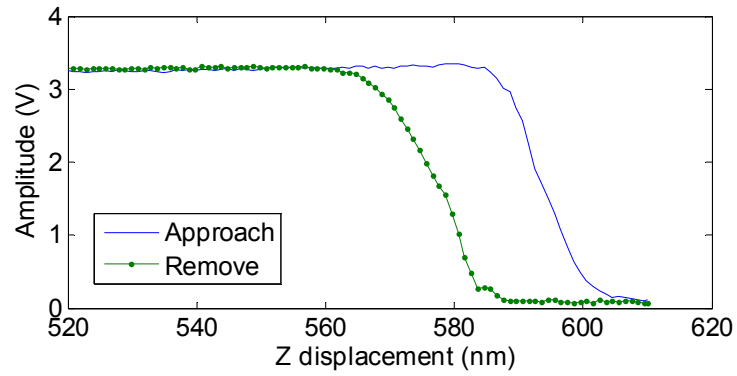


(b) In water

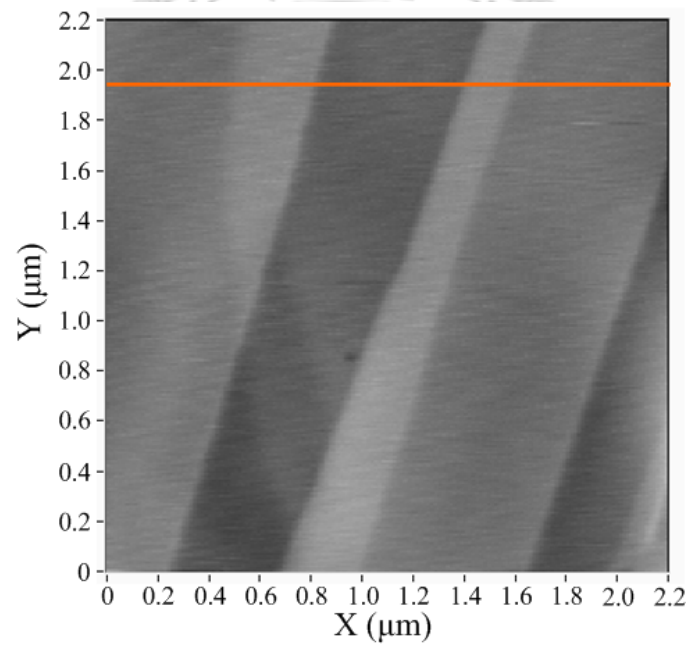
Figure 6.16 Flexural spectrums of cantilever PPP-NCHAuD in air and water

For testing the resolution in water, the graphite (HOPG) sample is measured. Water is dropped on the holder to surround the cantilever and the graphite surface individually, and the two drops bind together during tip-sample approaching. Figure 6.17(a) shows the force-displacement curve, and the topographic image and the cross-sectional profile are shown in Figure 6.17(b) and 6.17(c), respectively. Single and double atomic layers

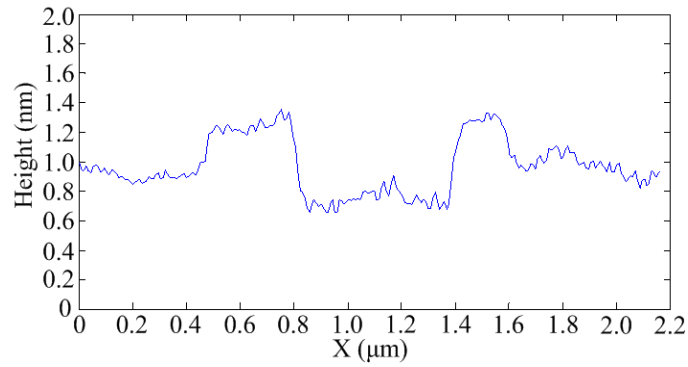
of the graphite can be observed distinctly. (The feedback setpoint is 60% of the free amplitude, and the P-gain and I-gain are 1 and 60, respectively. The scan rate is 0.3 lines/sec, and the image pixels are 256×256 points.)



(a) Force-displacement curve



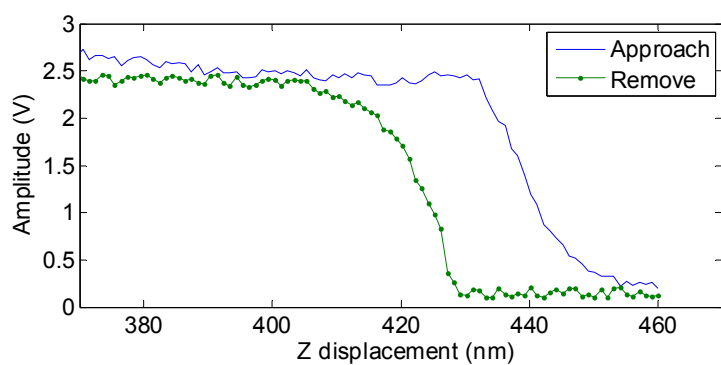
(b) Topography



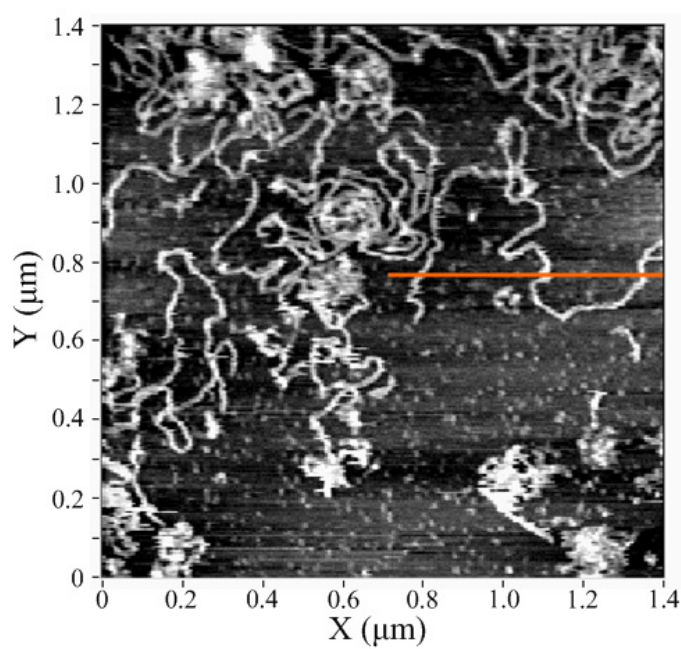
(c) Cross-sectional profile

Figure 6.17 Scanning results on graphite (HOPG) in water

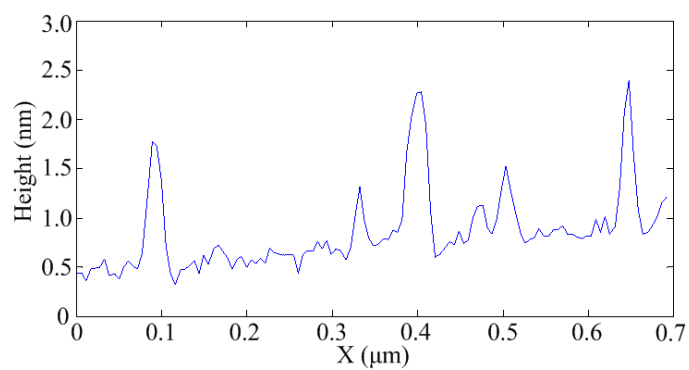
For demonstrating the soft bio-sample, a Lambda DNA sample (N3011S, BioLabs) is prepared on a mica substrate. For stabilizing the DNA on the mica surface through static electrostatic force, the DNA of  $10 \text{ ng}/\mu\text{l}$  is mixed with the  $\text{NiCl}_2$  of  $4 \text{ mM}$  by 1:1 volume ratio. Then the  $5 \mu\text{l}$  DNA is dropped on the mica surface, and incubated about 5 mins. For reducing the interactive force on the DNA, a soft cantilever (SCANASYST-FLUID+, Veeco) with a spring constant of  $0.7 \text{ N/m}$  is used. Its typical resonant frequency is around  $150 \text{ kHz}$  in air. In the liquid experiment, the driving frequency is operated at  $34.3 \text{ kHz}$ . Figure 6.18(a) represents the force-displacement curve on the mica substrate, and the DNA image is displayed in Figure 6.18(b). From the cross-sectional profile in Figure 6.18(c), the height of the DNA is about  $1.5 \text{ nm}$ . (The feedback setpoint is 74% of the free amplitude, and the P-gain and I-gain are 2 and 150, respectively. The scan rate is  $0.2 \text{ lines/sec}$ , and the image pixels are  $256 \times 256$  points.)



(a) Force-displacement curve on mica



(b) Topography



(c) Cross-sectional profile

Figure 6.18 Scanning results of DNA on mica in liquid



## 6.3 Conclusion

A liquid-AFM system is developed based on the astigmatic detection method, which can detect not only the linear but also angular displacement of the cantilever. The beam path of the astigmatic pickup head is perpendicular to the cantilever and can be easily focused on the cantilever. Besides, its beam path is shorter than that of the optical beam deflection system. The programmable embedded controller, the PC and LabVIEW software effectively realize all AFM functions that include the scanning, the tapping, the approaching, the signal processing, the data representation, and the user interface. Through applying the high-speed ADC, DAC, and the digital lock-in amplifier, the sampling rate is increased to 5 MHz. Furthermore by optimizing the water thickness and the optical configuration, the astigmatic detection system (ADS) also achieves sufficient detection sensitivity for the water environment. For reducing the spurious vibration induced through the liquid environment, the cantilever holder is integrated with the damping PEEK layer between the steel structures. And for avoiding vibration transmission and enhancing the resonant peak, the spring chip for the cantilever is also isolated from the holder base.

For the experimental verification, the scanner displacement is calibrated in air by using square test gratings, and shows a high linearity with the coefficient of determination  $R^2$  of 0.99998. The scanning graphite (HOPG) image verifies that the Z-axis resolution reaches the sub-nanometer scale. Through optimizing the water thickness and the optical configuration, the spurious peaks are suppressed down to 26.0 % of the resonant peaks in the liquid environment. Furthermore, it is verified that the liquid-AFM can realize high-resolution scanning images of the sub-nano scale graphite layer and the soft DNA sample in water.

## Chapter 7

### Summary

For improving the dynamic properties of the cantilever in liquid, the cantilever dimensions and geometry are studied. Through decreasing the cantilever thickness and length proportionally, the resonant frequency and the Q-factor can be raised, and the spring constant can be maintained by a constant width. However, the cantilever dimensions are restricted by the laser spot size of the cantilever detection system. For overcoming this limitation, an approach of making holes on the cantilever is experimented, but the results show insignificant effects on both the Q-factor and the resonant frequency. Besides, the high-order resonances can provide higher mass sensitivity than the fundamental one. For applying to AFM scanning, their resolution and stability need for further examinations.

For suppressing spurious peaks in liquid, the integration of the damping PEEK layer and the steel structures is adopted in the cantilever holder. Besides, the preload adjustment can improve the excitation spectrum. However, its influences on the piezoelectric actuators and the cantilever chip need to be further identified. The clamp-modification holder isolates the spring clip and the holder base, and avoids constriction on the piezoelectric actuators. This developed design is verified that it can enhance both flexural and torsional peaks on two different types of the cantilevers.

An astigmatic pickup head is utilized for detecting the cantilever deflection. For increasing its sensitivity in liquid, the optimal water thickness of 0.48 mm is proposed with a cover glass. The highest sensitivity  $S_{ADS}$  of 4.040 mV/nm is obtained in water, which approximates to the sensitivity through a polycarbonates layer in air. After this modification, the breast cancer cell MCF-7 can be imaged clearly through the optical

scanning mode in liquid. Besides, the astigmatic pickup head can detect both the linear and angular displacement of the cantilever. Utilizing this property, an efficient method of cantilever spring constant calibration is proposed. This method can be also applied to tipless cantilevers, which are widely applied in many cantilever-based mass sensors.

A liquid-AFM system is developed based on the astigmatic detection method. For fulfilling AFM-process, the LabVIEW System Design Software is applied for programming whole system functions on the embedded controller configuration. The performance of the liquid-AFM system is experimentally verified by detecting different samples in both air and liquid environments. Through optimizing the water thickness and the holder configuration, the spurious peaks are suppressed down to 26.0 % of the resonant peaks in the liquid environment. Furthermore, it is verified that the liquid-AFM can realize high-resolution scanning images of the sub-nano scale graphite layer and the soft DNA sample in water.

In the future, high speed, high resolution, and large scan range are the long-term targets. Therefore, the shorter and thinner cantilever should be utilized. For the short cantilever, the angular signal of the astigmatic pickup head is proposed for improving the sensitivity. Besides, the angular signal is also necessary for the torsion mode, which can provide higher Q-factor and resonant frequency. In addition, the optical interference problem could increase if the laser penetrates the thinner cantilever. For widening applications, the environmental control such as buffer exchange, temperature, and pressure are necessary.

## References

- [1] Binnig, G., Rohrer, H., Gerber, Ch., and Weibel, E., "Surface studies by scanning tunneling microscopy," *Physical Review Letters*, vol. 49, no.1, pp. 57-61, 1982
- [2] Binnig, G., Rohrer, H., Gerber, Ch., and Weibel, E., " $7 \times 7$  Reconstruction on Si(111) resolved in real space," *Physical Review Letters*, vol. 50, no. 2, pp. 120-123, 1983
- [3] Eigler, D. M. and Schweizer, E. K., "Positioning single atoms with a scanning tunnelling microscope," *Nature*, vol. 344, no. 5, pp. 524-526, 1990
- [4] Binnig, G. C., Quate, F., and Gerber, Ch., "Atomic force microscope," *Physical Review Letters*, vol. 56, no. 9, pp. 930-933, 1986
- [5] Mate, C. M., McClelland, G. M., Erlandsson, R., and Chiang, S. "Atomic-scale friction of a tungsten tip on graphite surface," *Physical Review Letters*, vol. 59, no. 17, pp. 1942-1945, 1987
- [6] Martin Y. and Wickramasinghe, H. K., "Magnetic imaging by force microscopy with 1000 Å resolution," *Applied Physics Letters*, vol. 50, no. 20, pp. 1455-1457, 1987
- [7] Martin, Y., Abraham, D. W., and Wickramasinghe, H. K., "High-resolution capacitance measurement and potentiometry by force microscopy," *Applied Physics Letters*, vol. 52, no. 13, pp. 1103-1105, 1988
- [8] Terris, B. D., Stern, J. E., Ruger, D., and Mamin, H. J., "Contact electrification using force microscopy," *Physical Review Letters*, vol. 63, no. 24, pp. 2669-2672, 1989
- [9] Heinzelmann, H. and Pohl, D. W., "Scanning near-field optical microscopy," *Applied Physics A*, vol. 59, pp. 89-101, 1994

- [10] Williams, C. C. and Wickramasinghe, H. K., "Scanning thermal microscopy," *Applied Physics Letters*, vol. 49, no. 23, pp. 1587-1589, 1986
- [11] Hansma, H. G., Vesenka, J., Siegerist, C., Kelderman, G., Morrett, H., Sinsheimer, R. L., Elings, V., Bustamante, C., and Hansma, P. K., "Reproducible imaging and dissection of plasmid DNA under liquid with the atomic force microscope," *Science*, vol. 256, no. 22, pp. 1180-1184, 1992
- [12] Lee, G., Abdi, K., Jiang, Y., Michaely, P., Bennett, V., and Marszalek, P. E., "Nanospring behaviour of ankyrin repeats," *Nature*, vol. 440, no. 9, pp. 246-249, 2006
- [13] Ke, C., Humeniuk, M., S-Gracz, H., and Marszalek, P. E., "Direct measurements of base stacking interactions in DNA by single-molecule atomic force spectroscopy," *Physical Review Letters*, vol. 99, p. 018302, 2007
- [14] Drake, B., Prater, C. B., Weisenhorn, A. L., Gould, S. A. C., Albrecht, T. R., Quate, C. F., Cannell, D. S., Hansma, H. G., and Hansma, P. K., "Imaging crystals, polymers, and processes in water with the atomic force microscope," *Science*, vol. 243, pp. 1586-1589, 1989
- [15] Fotiadis, D., "Atomic force microscopy for the study of membrane proteins," *Current Opinion in Biotechnology*, vol. 23, pp. 1-6, 2011
- [16] Müller, D. J. and Engel, A., "Voltage and pH-induced channel closure of porin OmpF visualized by atomic force microscopy," *Journal of Molecular Biology*, vol. 285, pp. 1347-1351, 1999
- [17] Butt, H.-J., Wolff, E. K., Gould, S. A. C., Northern, B. D., Peterson, C. M., and Hansma, P. K., "Imaging cells with the atomic force microscope," *Journal of Structural Biology*, vol. 105, pp. 54-61, 1990
- [18] Müller, D. J. and Dufrêne, Y. F., "Atomic force microscopy: a nanoscopic window

- on the cell surface,” *Trends in Cell Biology*, vol. 21, no. 8, pp. 461-469, 2011
- [19] Stark, R. W., Thalhammer, S., Wienberg, J., and Heckl, W. M., “The AFM as a tool for chromosomal dissection – the influence of physical parameters,” *Applied Physics A*, vol. 66, pp. S579-S584, 1998
- [20] Goncalves, R. P. and Scheuring, S., “Manipulating and imaging individual membrane proteins by AFM,” *Surface and Interface Analysis*, vol. 38, pp. 1413-1418, 2006
- [21] Zong, Q., Innis, D., Kjoller, K., and Elings, V. B., “Fractured polymer/silica fiber surface studied by tapping mode atomic force microscopy,” *Surface Science Letters*, vol. 290, pp. L688-L692, 1993
- [22] Hansma, P. K., Cleveland, J. P., Radmacher, M., Walters, D. A., Hillner, P. E., Bezanilla, M., Fritz, M., Vie, D., Hansma, H. G., Prater, C. B., Massie, J., Fukunage, L., Gurley, J., and Elings, V., “Tapping mode atomic force microscopy in liquid,” *Applied Physics Letters*, vol. 64, no. 13, pp. 1738-1740, 1994
- [23] Cleveland, J. P., Anczykowski, B., Schmid, A. E., and Elings, V. B., “Energy dissipation in tapping-mode atomic force microscopy,” *Applied Physics Letters*, vol. 72, no. 20, pp. 2613-2615, 1998
- [24] Stark, M., Möller, C., Müller, D. J., and Guckenberger, R., “From images to interactions: high-resolution phase imaging in tapping-mode atomic force microscopy,” *Biophysical Journal*, vol. 80, pp. 3009-3018, 2001
- [25] Fukuma, T., Kilpatrick, J. I., and Jarvis, S. P., “Phase modulation atomic force microscope with true atomic resolution,” *Review of Scientific Instruments*, vol. 77, p 123703, 2006
- [26] Albrecht, T. R., Grütter, P., Horne, D., and Rugar, D., “Frequency modulation detection using high-Q cantilevers for enhanced force microscope sensitivity,”

*Journal of Applied Physics*, vol. 69, no. 2, pp. 668-673, 1991

- [27] Fukuma, T., Kobayashi, K., Matsushige, K., and Yamada, H., “True atomic resolution in liquid by frequency-modulation atomic force microscopy,” *Applied Physics Letters*, vol. 87, p. 034101, 2005
- [28] Hölscher, H., Gotsmann, B., Allers, W., Schwarz, U. D., Fuchs, H., and Wiesendanger, R., “Measurement of conservative and dissipative tip-sample interaction forces with a dynamic force microscope using the frequency modulation technique,” *Physical Review B*, vol. 64, p. 075402, 2001
- [29] Stark, R. W., Drobek, T., and Heckl, W. M., “Tapping-mode atomic force microscopy and phase-imaging in higher eigenmodes,” *Applied Physics Letters*, vol. 74, no. 22, pp. 3296-3298, 1999
- [30] Sahin, O., Yaralioglu, G., Grow, R., Zappe, S. F., Atalar, A., Quate, C., and Solgaard, O., “High-resolution imaging of elastic properties using harmonic cantilevers,” *Sensors and Actuators A*, vol. 114, pp. 183-190, 2004
- [31] Sahin, O., Magonov, S., Su, C., Quate, C. F., and Solgaard, O., “An atomic force microscope tip designed to measure time-varying nanomechanical forces,” *Nature Nanotechnology*, vol. 2, pp. 507- 514, 2007
- [32] Reinstädler, M., Kasai, T., Rabe, U., Bhushan, B., and Arnold, W., “Imaging and measurement of elasticity and friction using the Trmode,” *Journal of Physics D: Applied Physics*, vol. 38, pp. R269-R282, 2005
- [33] Yurtserver, A., Gigler, A. M., and Stark, R. W., “Amplitude and frequency modulation torsional resonance mode atomic force microscopy of a mineral surface,” *Ultramicroscopy*, vol. 109, pp. 275-279, 2009
- [34] Yang, C.-W. and Hwang, I.-S., “Soft-contact imaging in liquid with frequency-modulation torsion resonance mode atomic force microscopy,”

*Nanotechnology*, vol. 21, p. 065710, 2010

- [35] Schäffer, T. E., Cleveland, J. P., Ohnesorge, F., Walters, D. A., and Hansma, P. K., “Studies of vibrating atomic force microscope cantilevers in liquid,” *Journal of Applied Physics*, vol. 80, no. 7, pp. 3622-3627, 1996
- [36] Kiracofe, D. and Raman, A., “Quantitative force and dissipation measurements in liquids using piezo-excited atomic force microscopy: a unifying theory,” *Nanotechnology*, vol. 22, p. 485502, 2011
- [37] Chen, Y., Cai, J., Liu, M., Zeng, G., Feng, Q., and Chen, Z., “Research on double-probe, double- and triple-tip effects during atomic force microscopy scanning,” *Scanning*, vol. 26, pp. 155-161, 2004
- [38] Matei, G. A., Thoreson, E. J., Pratt, J. R., Newell, D. B., and Burnham, N. A., “Precision and accuracy of thermal calibration of atomic force microscopy cantilevers,” *Review of Scientific Instruments*,” vol. 77, p. 083703, 2006
- [39] Jarvis, S. P., Oral, A., Weihs, T. P., and Pethica, J. B., “A novel force microscope and point contact probe,” *Review of Scientific Instruments*,” vol. 64, no. 12, pp. 3515-3520, 1993
- [40] Xu, X. and Raman, A., “Comparative dynamics of magnetically, acoustically, and Brownian motion driven microcantilevers in liquids,” *Journal of Applied Physics*, vol. 102, p. 034303, 2007
- [41] Buguin, A., Roure, O. D., and Silberzan, P., “Active atomic force microscopy cantilevers for imaging in liquids,” *Applied Physics Letters*, vol. 78, no. 19, pp. 2982-2984, 2001
- [42] Enders, O., Korte, F., and Kolb, H.-A., “Lorentz-force-induced excitation of cantilevers for oscillation-mode scanning probe microscopy,” *Surface and Interface Analysis*, vol. 36, pp. 119-123, 2004



- [43] Jeon, S., Braiman, Y., and Thundat, T., "Cross talk between bending, twisting, and buckling modes of three types of microcantilever sensors," *Review of Scientific Instruments*," vol. 75, no. 11, pp. 4841-4844, 2004
- [44] Umeda, N., Ishizaki, S., and Uwai, H., "Scanning attractive force microscope using photothermal vibration," *Journal of Vacuum Science and Technology B*, vol. 9, no. 2, pp. 1318-1322, 1991
- [45] Nishida, S., Kobayashi, D., Sakurada, T., Nakazawa, T., Hoshi, Y., and Kawakatsu, H., "Photothermal excitation and laser Doppler velocimetry of higher cantilever vibration modes for dynamic atomic force microscopy in liquid," *Review of Scientific Instruments*," vol. 79, p. 123703, 2008
- [46] Adams, J. D., York, D., and Whisman, N., "Reduction of spurious resonance peaks in microcantilever tuning through substrate contact surface reduction," *Review of Scientific Instruments*," vol. 75, no. 9, pp. 2903-2905, 2004
- [47] Asakawa, H. and Fukuma, T., "Spurious-free cantilever excitation in liquid by piezoactuator with flexure drive mechanism," *Review of Scientific Instruments*," vol. 80, p. 103703, 2009
- [48] Tortonese, M., Barrett, R. C., and Quate, C. F., "Atomic resolution with an atomic force microscope using piezoresistive detection," *Applied Physics Letters*, vol. 62, no. 8, pp. 834-836, 1993
- [49] Blanc, N., Brugger, J., Rooij, N. F. De, and Dürig, U., "Scanning force microscopy in the dynamic mode using microfabricated capacitive sensors," *Journal of Vacuum Science and Technology B*, vol. 14, pp. 901-905, 1996
- [50] Ruger, D., Mamin, H. J., and Guethner, P., "Improved fiber-optic interferometer for atomic force microscopy," *Applied Physics Letters*, vol. 55, no. 25, pp. 2588-2590, 1989

- [51] Meyer, G. and Amer, N. M., "Novel optical approach to atomic force microscopy," *Applied Physics Letters*, vol. 53, no. 12, pp. 1045-1047, 1988
- [52] Meyer, G. and Amer, N. M., "Optical-beam-deflection atomic force microscopy: The NaCl (001) surface," *Applied Physics Letters*, vol. 56, no. 21, pp. 2100-2101, 1990
- [53] Hwu, E.-T., Huang, K.-Y., Hung, S.-K., and Hwang, I.-S., "Measurement of cantilever displacement using a compact disk/digital versatile disk pick head," *Japanese Journal of Applied Physics*, vol. 45, no. 3B, pp. 2368-2371, 2006
- [54] Hwu, E.-T., Hung, S.-K., Yang, C.-W., Hwang, I.-S., and Huang, K.-Y., "Simultaneous detection of translational and angular displacements of micromachined elements," *Applied Physics Letters*, vol. 91, p. 221908, 2007
- [55] Mahmood, I. A. and Moheimani, S. O. R., "Fast spiral-scan atomic force microscopy," *Nanotechnology*, vol. 20, p. 365503, 2009
- [56] Clough, R. W. and Penzien, J., "Dynamics of structures," *Computer & Structure, Inc.*, 3<sup>rd</sup> ed., pp. 377-385, 2003
- [57] Sader, J. E., "Frequency response of cantilever beams immersed in viscous fluids with applications to the atomic force microscope," *Journal of Applied Physics*, vol. 84, no. 1, pp. 64-76, 1998
- [58] Eysden, C. A. V. and Sader, J. E., "Small amplitude oscillations of a flexible thin blade in a viscous fluid: Exact analytical solution," *Physics of Fluids*, vol. 18, p. 123102, 2006
- [59] Eysden, C. A. V. and Sader, J. E., "Frequency response of cantilever beams immersed in viscous fluids with applications to the atomic force microscope: Arbitrary mode order," *Journal of Applied Physics*, vol. 101, p. 044908, 2007
- [60] Veeco Instruments Inc., "Support note 402, revision E," 2004

- [61] Hwu, E.-T., Illers, H., Jusko, L., and Danzebrink, H.-U., “A hybrid scanning probe microscope (SPM) module based on a DVD optical head,” *Measurement Science and Technology*, vol. 20, p. 084005, 2009
- [62] Burnham, N. A., Chen, X., Hodges, C. S., Matei, G. A., Thoreson, E. J., Roberts, C. J., Davies, M. C., and Tendler, S. J. B., “Comparison of calibration methods for atomic-force microscopy cantilevers,” *Nanotechnology*, vol. 14, pp. 1-6, 2003
- [63] Hung, S.-K., “Design and control of novel atomic force microscope systems,” Ph.D. Dissertation, Department of Electrical Engineering College of Electrical Engineering and Computer Science, National Taiwan University, Taiwan, pp. 23-24, 2007



# Appendix A

## Cantilever tip PPP-NCHAuD



### PPP-NCHAuD

*PointProbe® Plus Non-Contact / Tapping Mode - High Resonance Frequency - Au coating (Detector Side)*

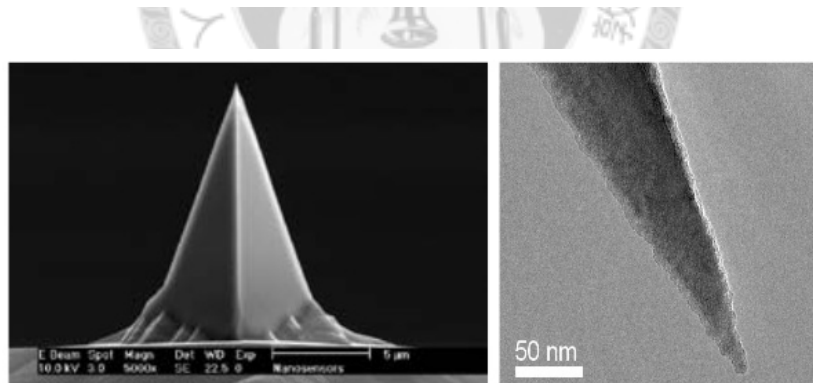
The **Point Probe® Plus (PPP)** combines the well-known features of the proven PointProbe® series such as high application versatility and compatibility with most commercial SPMs with a further reduced and more reproducible tip radius as well as a more defined tip shape. The typical tip radius of less than 7 nm and the minimized variation in tip shape provide more reproducible images and enhanced resolution.

NANOSENSORS™ PPP-NCHAuD probes are designed for non-contact mode or tapping mode AFM (also known as: attractive or dynamic mode). This AFM probe combines high operation stability with outstanding sensitivity and fast scanning ability.

#### The probe offers unique features:

- guaranteed tip radius of curvature < 10 nm
- highly doped to dissipate static charge
- Au coating on detector side of cantilever
- chemically inert

A metallic layer (Au) is coated on the detector side of the cantilever which enhances the reflectivity of the laser beam by a factor of about 2.5. Furthermore it prevents light from interfering within the cantilever. The virtually stress-free coating is bending the cantilever less than 2 % of the cantilever length.



#### Cantilever data:

Technical Data	Nominal Value	Specified Range
Thickness /µm	4.0	3.0-5.0
Mean Width /µm	30	22.5-37.5
Length /µm	125	115-135
Force Constant /(N/m)	42	10-130
Resonance Frequency /kHz	330	204-497

#### Order codes and shipping units:

Order Code	Quantity	Data Sheet	Coating
PPP-NCHAuD-10	10	of all probes	Au (detector side)

For further information please contact your local distributor or **NANOSENSORS™** directly.

**NANOSENSORS™** is a trademark of NanoWorld AG / info@nanosensors.com / www.nanosensors.com

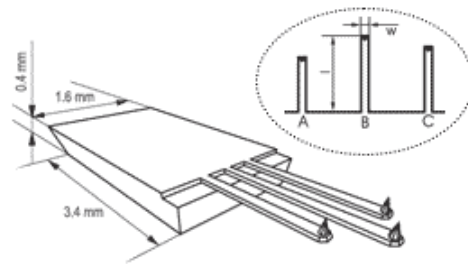
# Appendix B

## Cantilever tip CSC38/Cr-Au

### CSC38, CANTILEVERS



SEM image of 3 cantilevers (A, B, C) on chip of the CSC38 series.



Schematic drawing of the probe chip.

CSC38, Cantilevers	Resonant Frequency, kHz			Spring Constant, N/m			Length $l \pm 5$ , $\mu\text{m}$	Width $w \pm 3$ , $\mu\text{m}$	Thickness $t \pm 0.3$ , $\mu\text{m}$
	min	typ	max	min	typ	max			
A	14	<b>20</b>	28	0.02	<b>0.08</b>	0.2	250	35	1.0
B	7	<b>10</b>	14	0.01	<b>0.03</b>	0.08	350		
C	9.5	<b>14</b>	19	0.01	<b>0.05</b>	0.1	300		



### CSC38/Cr-Au

Conducting SPM Probe with tip height 20-25  $\mu\text{m}$ , cone angle  $<40^\circ$  mounted on a rectangular 3.4x1.6x0.4 mm silicon chip.

Tip radius, nm ▶	<b>&lt; 50</b>		
Chip lever configuration ▶			
Cantilever length, $\pm 5 \mu\text{m}$ ▶	<b>250</b>	<b>350</b>	<b>300</b>
Cantilever width, $\pm 3 \mu\text{m}$ ▶	<b>35</b>		
Cantilever thickness, $\pm 0.5 \mu\text{m}$ ▶	<b>1.0</b>		
Resonant frequency, kHz ▶	<b>20</b> <small>(14-28)</small>	<b>10</b> <small>(7.0-14)</small>	<b>14</b> <small>(9.5-19)</small>
Force constant, N/m ▶	<b>0.08</b> <small>(0.02-0.2)</small>	<b>0.03</b> <small>(0.03-0.08)</small>	<b>0.05</b> <small>(0.01-0.1)</small>
Tipside coating, nm ▶	<b>Cr 20; Au 20</b>		
Backside coating, nm ▶	<b>Cr 20; Au 20</b>		

# Appendix C

## Tipless cantilever Arrow TL1Au



**Type: Arrow™ TL1Au**

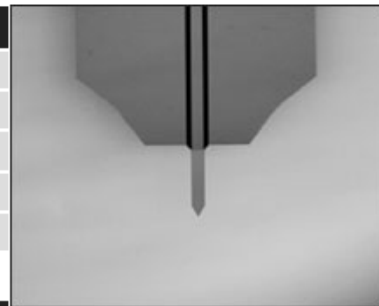
### Special Application Cantilevers

NanoWorld Arrow™ TL1Au probes are tipless cantilevers for special applications. They can for example be used for attaching spheres and other objects to the free end of the cantilever, or for functionalizing and sensing applications.

All SPM and AFM probes of the Arrow™ series are made from monolithic silicon which is highly doped to dissipate static charge and are chemically inert. The TL1Au probes feature one rectangular cantilever with a triangular free end.

The Arrow™ TL1Au probes feature a sample facing side coating of 5 nm titanium / 30 nm gold. They are optionally available without a coating ([Arrow™ TL1](#)).

Cantilever Data	Value	Range*
Thickness	1.0 µm	0.5 - 2.5
Width (rectangular part)	100 µm	95 - 105
Length	500 µm	495 - 505
Force Constant	0.03 N/m	0.004 - 0.54
Resonance Frequency	6 kHz	3 - 14



Order Code	Quantity	Data Sheet
ARROW-TL1Au-50	50	Nominal values

\*Typical values

For more information contact: [info@nanoworld.com](mailto:info@nanoworld.com)

Arrow™ is a trademark of NanoWorld AG.  
All data are subject to change without notice.

NanoWorld AG  
Rue Jaquet-Droz 1  
Case Postale 216  
CH-2002 Neuchâtel  
Switzerland  
[www.nanoworld.com](http://www.nanoworld.com)

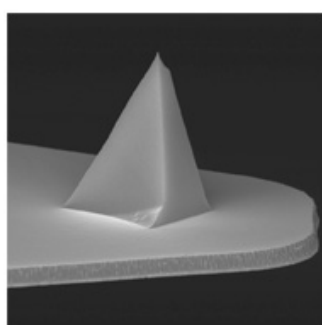
# Appendix D

## Cantilever tip SCANASYST-FLUID+

Shape	Resonant Freq. kHz			Spring Const. N/m			Length $\mu\text{m}$			Width $\mu\text{m}$		
	Nom.	Min.	Max.	Nom.	Min.	Max.	Nom.	Min.	Max.	Nom.	Min.	Max.
Triangular	150	100	200	0.7	0.35	1.4	70	65	75	10	5	15

### Tip Specification

ScanAsyst Fluid+ probes marry the sharpness of a Silicon tip with the low spring constant and high sensitivity of a Silicon Nitride cantilever, for an unprecedented level of high resolution and force control on samples in fluid.

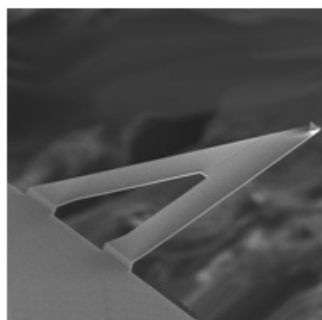


<b>Geometry:</b>	Rotated (Symmetric)
<b>Tip Height (h):</b>	2.5 - 8.0 $\mu\text{m}$
<b>Front Angle (FA):</b>	15 $\pm$ 2.5 $^\circ$
<b>Back Angle (BA):</b>	25 $\pm$ 2.5 $^\circ$
<b>Side Angle (SA):</b>	17.5 $\pm$ 2.5 $^\circ$
<b>Tip Radius (Nom):</b>	2nm
<b>Tip Radius (Max):</b>	12nm
<b>Tip SetBack (TSB)(Nom):</b>	5 $\mu\text{m}$
<b>Tip Set Back (TSB)(RNG):</b>	3 - 7 $\mu\text{m}$

### Cantilever Specification

[Cantilever Orientation diagram](#) can be found here.

ScanAsyst probes have less than 2deg of cantilever bend.



<b>Material:</b>	Silicon Nitride
<b>Geometry:</b>	Triangular
<b>Cantilevers Number:</b>	1
<b>Cantilever Thickness (Nom):</b>	0.6 $\mu\text{m}$
<b>Cantilever Thickness (RNG):</b>	0.55 - 0.65 $\mu\text{m}$
<b>Back Side Coating:</b>	Reflective Gold
<b>Top Layer Back:</b>	45 $\pm$ 5 nm of Ti/Au

# Appendix E

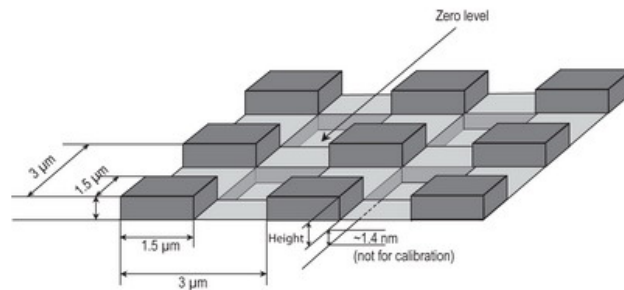
## Test grating TGQ1



### Test Grating TGQ1

Test grating TGQ1 is intended for:

- simultaneous calibration in X, Y and Z directions;
- lateral calibration of SPM scanners;
- detection of lateral non-linearity, hysteresis, creep and cross-coupling effects.



### Grating description

Structure	- Si wafer - the grating is formed on the layer of SiO <sub>2</sub>
Pattern types	3-Dimensional array of small rectangles
Period	3.0±0,05 μm
Height	20nm ±1,5 nm*
Rectangles side size:	1,5±0,35 μm
Chip size	5x5x0,5 mm
Effective area	central square 3x3 mm

\* the average meaning based on the measurements of 5 gratings (from the batch of 300 gratings) by SPM calibrated by PTB certified grating TGZ1. Basic step height can vary from the specified one within ±10% (for example step height can be 22±1.5nm)

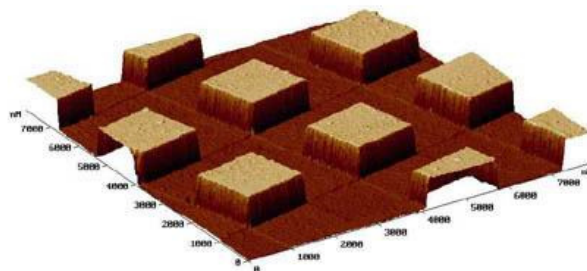


Fig.1 SPM image of TGQ1 grating



# Appendix F

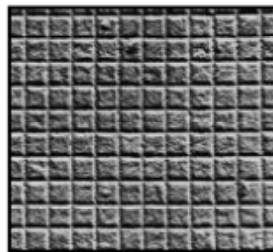
## Test grating 607-AFM



## TECHNICAL NOTES

### CALIBRATION SPECIMEN for ATOMIC FORCE MICROSCOPE PRODUCT NO. 607-AFM

This specimen is a cellulose acetate replica of a 2,160 lines/mm waffle pattern diffraction grating. When imaging the specimen, it should be kept in mind that the line spacing is 0.463 $\mu$ m and the pattern will not be visible until the imaging system is set to resolve that level of detail.



The height of the bars of the grid pattern is approximately 31nm. To calibrate instrument magnification, use the following calculation where **A** represents the distance in mm between limiting lines of the spaces measured and **B** represents the number of spaces measured:

$$\text{Magnification} = A \times 2,160 / B$$

(Use a scan size of under 10 $\mu$ m for best results.)

#### CARE OF THE SPECIMEN

Open the storage box by cutting the white label where the lid and base meet.

At all times, the surface of the replica must be protected from damage. The replica is mounted on a metal disk, which is laying facedown in the storage box. The disk can be removed by carefully inserting forceps under the rim, using the groove provided in the box base. Do not grip more than 1mm into the center of the disk. Once the disk is removed from the storage box, always lay it down with the specimen side facing up. Store the specimen in the original box or a similar container, which will protect the surface.

Do not attempt to clean the specimen or remove it from the metal disk.

Never allow the specimen to be exposed to water or solvents.

**Note:** During the mounting process, an area around the extreme outer edges of the specimen may have been damaged. Avoid these areas when using the specimen for calibration purposes.

607-AFM TN 3/02

#### **TED PELLA, INC.**

*Tools for Science and Industry*

P.O. Box 492477, Redding, CA 96049-2477, U.S.A.

Telephone: 530-243-2200; 800-237-3526 (U.S.A. or Canada) • FAX: 530-243-3761

Email: sales@tedpella.com • Web Site: <http://www.tedpella.com>



## Publication List

### International Journal:

1. Wesley W. Hsiao, Hsien-Shun Liao, Hsing-Hung Lin, Ren-Feng Ding, Kuang-Yuh Huang, and Chia-Seng Chang, “Motility Measurement of a Mouse Sperm by Atomic Force Microscopy”, *Analytical Sciences* (SCI), Accepted, 2012
2. Ing-Shouh Hwang, Chih-Wen Yang, Ping-Hsiang Su, En-Te Hwu, and Hsien-Shun Liao, “Imaging Soft Matters in Water with Torsional Mode Atomic Force”, *Ultramicroscopy* (SCI), Accepted, 2012
3. Hsien-Shun Liao, Bo-Jing Juang, Kuang-Yuh Huang, En-Te Hwu, and Chia-Seng Chang, “Spring Constant Calibration of Microcantilever by Astigmatic Detection System”, *Japanese Journal Applied Physics* (SCI), **51**, 08KB13, 2012
4. W.-C. Chang, W.-C. Lai, H.-S. Liao, S. C. Wang, M. S. Ho, K.-Y. Huang, L. J. Chen, and C. S. Chang, “Orientation-dependent friction between a carbon nanotube and graphite”, *Applied Physics Letters* (SCI), **101**, 063109, 2012
5. En-Te Hwu, Hsien-Shun Liao, Filippo G. Bosco, Ching-Hsiu Chen, Stephan Sylvest Keller, Anja Boisen, and Kuang-Yuh Huang, “An Astigmatic Detection System for Polymeric Cantilever-Based Sensors”, *Journal of Sensors*, **2012**, 580939, 2012
6. H.-S. Liao, B.-J. Juang, W.-C. Chang, W.-C. Lai, K.-Y. Huang, and C.-S. Chang, “Rotational Positioning System Adapted to Atomic Force Microscope for Measuring Anisotropic Surface Properties”, *Review of Scientific Instruments* (SCI), **82**, 113710, 2011 (selected for the December 12, 2011 issue of *Virtual Journal of Nanoscale Science & Technology*)

### International Conference:

1. R.-F. Ding, H.-S. Liao, C.-W. Yang, K.-Y. Huang, I.-S. Hwang, and C.-S. Chang, “Development of Adaptable Cantilever Holder for Atomic Force Microscopy in

- Liquid”, *20th International Colloquium on Scanning Probe Microscopy*, 2012
2. B.-J. Juang, T.-J. Chang, H.-S. Liao, K.-Y. Huang, E.-T. Hwu, and I.-S. Hwang, “Linear and Angular Detection Functions of Holographic Optical Element (HOE)-AFM”, *20th International Colloquium on Scanning Probe Microscopy*, 2012
  3. H.-S. Liao, B.-J. Juang, K.-Y. Huang, E.-T. Hwu, and C.-S. Chang, “Fast Spring Constant Calibration of Micro-cantilever using Astigmatic Detection System”, *19th International Colloquium on Scanning Probe Microscopy*, 2011
  4. H.-S. Liao, K.-Y. Huang, C.-S. Chang, “Cantilever-based Mass Sensor using High Order Resonances for Liquid Environment”, *IEEE/ASME International Conference on Advanced Intelligent Mechatronics*, 2011
  5. H.-S. Liao, K.-Y. Huang, E.-T. Hwu, C.-S. Chang, “Resonance-Enhanced Micromechanical Cantilever for Mass Sensing”, *IEEE/ASME International Conference on Advanced Intelligent Mechatronics*, 2010
  6. Bo-Jing Juang, Kuang-Yuh Huang, Hsien-Shun Liao, Kuok-Chan Leong, Ing-Shouh Hwang, “AFM Pickup Head with Holographic Optical Element (HOE)”, *IEEE/ASME International Conference on Advanced Intelligent Mechatronics*, 2010
  7. H.-S.,Liao, K.-Y.,Huang, C.-S.,Chang, C.-K.,Lin, S.-K.,Hung, ”Magnifying the Nanoworld: an Educational AFM”, *The ASME Asia-Pacific Engineering Education Congress*, 2009